MEASUREMENT OF THE CHARGE ASYMMETRY OF MUONS FROM W BOSON DECAY AT THE DØ DETECTOR

by

Ajay M. Narayanan

A Dissertation Submitted to the Faculty of the
DEPARTMENT OF PHYSICS
In Partial Fulfillment of the Requirements
For the Degree of
DOCTOR OF PHILOSOPHY
In the Graduate College
THE UNIVERSITY OF ARIZONA

1997

THE UNIVERSITY OF ARIZONA ®
GRADUATE COLLEGE

As members of the Final Examination Committee, we certify that we have read the dissertation prepared by AJAY M. NARAYANAN

entitled MEASUREMENT OF THE CHARGE ASYMMETRY OF MUONS FROM THE DECAY OF W BOSONS AT THE DØ DETECTOR.

and recommend that it be accepted as fulfilling the dissertation requirement for the Degree of Doctor of Philosophy

Dr. Kenneth E. Johns	Date 7/15/97
Dr. John P. Rutherfoord	Date 7/15/97
Dr. Robert L. Thews	Date 7/15/97
Dr. Douglas J. Donahue	Date 15 July 97
Dr. Fang Li-Zhi	Date 07/15/97

Final approval and acceptance of this dissertation is contingent upon the candidate's submission of the final copy of the dissertation to the Graduate College.

I hereby certify that I have read this dissertation prepared under my direction and recommend that it be accepted as fulfilling the dissertation requirement.

Dissertation Director	Date 7/15/97

STATEMENT BY AUTHOR

This dissertation has been submitted in partial fulfillment of requirements for an advanced degree at The University of Arizona and is deposited in the University Library to be made available to borrowers under the rules of the Library.

Brief quotations from this dissertation are allowable without special permission, provided that accurate acknowledgment of source is made. Requests for permission for extended quotation from or reproduction of this manuscript in whole or in part may be granted by the head of the major department or the dean of the Graduate College when in his or her judgement the proposed use of the material is in the interests of scholarship. In all other instances, however, permission must be obtained by the author

SIGNED: 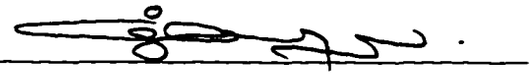

ACKNOWLEDGEMENTS

It is not possible to thank each of those who have, in some fashion or the other, helped, influenced or inspired me in this endeavour. So I express my heartfelt thanks to all you friends and teachers.

There were, however, some individuals whose help and guidance were invaluable in bringing this work to completion.

Foremost among them is my advisor Kenneth Johns. I owe a great deal to Ken's unstinting efforts as thesis advisor, general counselor and friend.

At the University of Arizona Physics Department, I would like to thank all my colleagues in the high energy physics group. In particular Dave Fein, Alex Smith and Eric James taught me the ropes when I started out in high energy physics. Dave Vititoe and I embarked on our projects at DØ at the same time and I thank him for his help in trying to understand the beast called the muon, in unraveling the black magic of the OTC card and in setting up OTC monitoring software. I also wish to thank members of the office staff, especially Iris Wright, without whose help I would have long perished under a mound of forms and deadlines.

I would like to thank all members of the DØ collaboration, the administrative staff at Fermilab and members of the accelerator division. I would like to thank Cecilia Gerber, Ting Hu, Paul Quintas, Atsushi Taketani and Darien Wood for following this work closely and contributing to it. Their comments, questions and insights helped define the path this work was to take. I would also like to thank members of the muon-ID and hardware maintenance groups who offered much help and advice.

To my parents.

TABLE OF CONTENTS

LIST OF FIGURES

LIST OF TABLES

ABSTRACT

We have measured the charge asymmetry of muons produced in W boson decay as a function of muon pseudorapidity. The W bosons were produced in $p\bar{p}$ collisions at $\sqrt{s} = 1.8$ TeV at the Fermilab Tevatron and recorded by the DØ detector during the run period 1992-1993 (run 1A) and 1994-1995 (run 1B). The combined data for both periods consists of 8831 $W \rightarrow \mu\nu$ decays with $|\eta_\mu| < 1.0$ selected from events corresponding to an integrated luminosity of 61.9 pb^{-1} and 664 decays with $1.0 \leq |\eta_\mu| < 1.6$ corresponding to an integrated luminosity of 44.5 pb^{-1} .

CHAPTER 1

THE STANDARD MODEL

1.1 Introduction

The Standard Model summarizes our knowledge of modern particle physics spanning, roughly, the hundred years between the discovery of the electron and that of the top quark. It describes, what are thought to be, the fundamental particles, or building blocks, of all matter and the interactions between them. A brief account of the Standard Model is presented below with an indication of where the present work, which is concerned with electroweak interactions, fits into the broader picture. A more detailed account of the electroweak theory and the physics relevant to the present analysis is presented in the next chapter.

1.2 Quarks and Leptons

The fundamental particles have been divided into two families: leptons and quarks. The known leptons consisting of electron, e, the muon μ and the tau, τ with corresponding neutrinos, ν_e, ν_μ and ν_τ, are arranged in three generations, as shown in Table 1.1. In this arrangement, each generation consists of a charged and a neutral lepton. Attached to each particle is a lepton number specific to its generation. The lepton number of each generation is conserved separately in any interaction.

$$\left\{ \begin{array}{c} e\,(\,0.00051,+1) \\ \nu_e(15\times10^{-6},0) \end{array} \right\}, \left\{ \begin{array}{c} \mu(\,0.1056,+1) \\ \nu_\mu(<0.017,0) \end{array} \right\} \text{and} \left\{ \begin{array}{c} \tau(\,1.77,+1) \\ \nu_\tau(\,<0.024,0) \end{array} \right\}$$

Table 1.1: Three generations of leptons.

The approximate masses [1], in GeV/c^2 , and the electric charge, in units of that of the electron, are shown in the parentheses. The mass of the charged lepton increases with each generation. The mass of neutrinos are assumed zero although this assumption continues to be tested by experiment.

The list of leptons shown above is to be complimented with a corresponding list of anti-particles with the same mass but opposite electric charge and, in the case of the neutrinos, helicity[1]. The issue of neutrino's helicity is intimately linked to whether it possesses mass. All leptons are spin-$\frac{1}{2}$ particles. Leptons interact via the weak interaction. Charged leptons also interact via the electromagnetic interaction.

Quarks are the building blocks of strongly interacting particles such as mesons and baryons. There are six *flavours* of quarks named Up, (u), Down, (d), Charm, (c), Strange, (s), Top, (t) and Bottom, (b). These are also arranged in three *generations* or weak isospin doublets as shown in Table 1.2.

$$\left\{ \begin{array}{c} u(0.002-0.008,+\frac{2}{3}) \\ d(0.005-0.015,-\frac{1}{3}) \end{array} \right\}, \left\{ \begin{array}{c} c(1-1.6,+\frac{2}{3}) \\ s(0.100-0.300,-\frac{1}{3}) \end{array} \right\} \text{and} \left\{ \begin{array}{c} t(175,+\frac{2}{3}) \\ b(4.1-4.5,-\frac{1}{3}) \end{array} \right\}$$

Table 1.2: Three generations of quarks.

Quarks are also spin-$\frac{1}{2}$ particles and possess fractional units of the electric charge. Free quarks and fractional electric charges have never been shown to exist with any reasonable certainty. In addition to spin and electric charge, quarks also possess a quantum number called *colour*. Each quark can come in one of three colours: Red, (r), Blue, (b), or Green, (g). Anti-quarks have opposite electric and colour charge and the above list needs a compliment of anti-particles. Quarks can interact via the strong, weak and the electromagnetic force if electrically charged.

[1] projection of the spin vector on the direction of motion. Neutrinos and antineutrinos are only seen with negative and positive helicities, respectively.

1.3 Interactions and Theories

In the Standard Model, all interactions are assumed to be invariant under certain symmetries. Examples are translations in space and time. Another important symmetry is *local gauge invariance* which means that the phase of the wave function describing a particle may vary with its position or in time without changing the physics. This requirement necessitates the existence of the so-called gauge bosons which mediate interactions between particles. The four fundamental forces of nature and their strengths relative to the electromagnetic force are shown below in Table 1.3.

Force	**Relative Strength**
Gravitational	10^{-40}
Electromagnetic	1
Strong	100
Weak	10^{-11}

Table 1.3: The fundamental forces of nature.

The force of gravitation lacks a successful quantum formulation which may be important for describing the early stages of the universe but even at the energies available at the most powerful particle accelerators this force plays no significant role in the interactions between fundamental particles.

Particles with electric charge interact via the the electromagnetic interaction which is successfully described by the theory of Quantum Electrodynamics (QED). The gauge boson that mediates the electromagnetic force is the photon, γ, which is a spin-1 particle, and is its own anti-particle.

The force that binds quarks into hadrons and exists between hadrons themselves, at a length scale of about 1 fm, is the strong force which is described by the theory of Quantum Chromodynamics (QCD). The attribute that makes these particles interact via the strong force, analogous to the electric charge, is called colour. The gauge boson that

mediates this force is the spin-1, massless gluon. The postulate of *confinement* requires that all naturally occuring particles be colour neutral. Accordingly all gluons are linear combinations of products of colour-anticolour quantum states. Colour confinement also prevents 'colored' free quarks from existing. They can exist only in colour-neutral bound states. Forces between bound quark systems such as mesons which are colour neutral are analogous to Van der Waals forces between electrically neutral molecules.

Both quarks and leptons carry the so-called *weak charge* and are thus capable of participating in phenomena involving weak interactions. In addition to transmuting a quark or lepton to its partner within a generation, the weak interaction is capable of turning a lepton or quark from one generation into a lepton or quark, respectively, belonging to another generation. The latter are called flavour changing charge current interactions since one unit of charge is exchanged while the former are termed flavour preserving neutral current interactions. Flavour mixing means that the quark generations shown above must really be represented as

$$\left\{ \begin{array}{c} u \\ d' \end{array} \right\}, \left\{ \begin{array}{c} c \\ s' \end{array} \right\} \text{and} \left\{ \begin{array}{c} t \\ b' \end{array} \right\}$$

where, d', s' and b' are linear combinations of the d, s and b quarks described by the Cabibo-Kobayashi-Masakawa matrix. The experimentally determined 90% confidence limits on the matrix elements are shown below [1].

$$\begin{pmatrix} d' \\ s' \\ b' \end{pmatrix} = \begin{bmatrix} 0.9745 - 0.9757 & 0.219 - 0.224 & 0.002 - 0.005 \\ 0.218 - 0.224 & 0.9736 - 0.9750 & 0.036 - 0.046 \\ 0.004 - 0.014 & 0.034 - 0.046 & 0.0989 - 0.9993 \end{bmatrix} \cdot \begin{pmatrix} d \\ s \\ b \end{pmatrix}$$

Generation mixing for leptons can happen only if neutrinos have mass.

Weak interactions are described by the Glashow-Salam-Weinberg (GSW) theory of electroweak interactions which unifies the electromagnetic and the weak forces. The gauge bosons in this theory, besides the photon, are the W^+ and the W^- that transmit charged current interactions where one unit of charge is exchanged and the Z that transmits neutral current interactions. Unlike the photon, the W and the Z bosons are spin-1 particles that possess mass.

A parameter required to complete this description is the Weinberg angle, θ_W. It enters the linear combination of the massless fields of the GSW theory that manifest themselves as the photon, the charged W bosons and the neutral Z boson as a result of *spontaneous symmetry breaking*. Spontaneous symmetry breaking is induced by the Higgs field. The Higgs boson which is the quantum of this field has, to date, not been observed experimentally. The recent average of LEP and SLC measurements of $\sin^2(\theta_W)$ yielding a value of 0.23166 ± 0.00064, a world average W boson mass of 80.401 ± 0.076 GeV/c^2 and a world average top quark mass value of 175.5 ± 5.5 GeV/c^2 constrains the mass of the Higgs boson to $166 \times 2^{\pm 1}$ GeV/c^2 [2].

1.4 The Scope of this Dissertation

This work measures the charge asymmetry of muons from the decay of W bosons, as a function of their pseudorapidity. The data was collected from $p\bar{p}$ collisions at the Fermilab Tevatron at $\sqrt{s} = 1.8$ TeV using the DØ detector. This measurement may be used to select the correct parton distribution function (PDF) for use at the energy and kinematic range appropriate at the Tevatron ($Q^2 = M_W^2$, $0.01 < x < 0.3$) from the many parameterizations that are available. Prior to measurements at the Tevatron, similar to the one presented in this work, the PDF's used were based on deep inelastic scattering data and then evolved to cover the Q^2 value and the kinematic range available at the Tevatron. The asymmetry measurement offers a way to select PDF's without complications from target systematics and potential theoretical uncertainties associated with the Q^2 evolution. The choice of PDF directly affects two important measurements at the Tevatron: the mass of the W boson and the ratio of the W boson decay width to that of the Z boson. These measurements are important tests of the Standard Model and departure from currently accepted theoretical values could point to new physics. An accurate measurement of the mass of the W boson will also help to theoretically pin down the mass of the Higgs boson.

The theoretical underpinnings of this measurement are described in Chapter 2. Chapter 3 describes the DØ detector. Chapter 4 describes the selection of events for the mea-

surement and the raw asymmetry derived from these, before corrections, is presented in Chapter 5. Chapter 6 describes background corrections and detector effects are dealt with in Chapter 7. Chapter 8 presents the corrected asymmetry values along with a comparison with theoretical predictions. Chapter 9 describes the upgrades to the DØ detector and the possibility of a better measurement in the next collider run of the Tevatron.

CHAPTER 2

THEORETICAL OVERVIEW

2.1 Introduction

This chapter explores the theoretical framework of the W boson charge asymmetry measurement and explains the motivation for it.

2.2 W Boson Production at the Tevatron

Proton-antiproton ($p\bar{p}$) collisions involving a hard scattering at high Q^2 may be represented by the parton model. Each parton i carries a fraction, $x_i (0 \leq x_i \leq 1)$, of the longitudinal momentum of the hadron and its transverse momentum is assumed negligible. The partons that scatter as well as the ones that do not (spectators) are assumed to fragment to final state hadrons.

The inclusive cross section for a $p\bar{p}$ collision producing a particle c accompanied by anything else can be written as [3]

$$\sigma(p\bar{p} \rightarrow c + X) = \sum_{i,j} C_{ij} \int dx_i \, dx_j \, [f_p^i(x_i).f_{\bar{p}}^j(x_j)] \, \hat{\sigma}(p_i\bar{p}_j \rightarrow c + X) \tag{2.1}$$

where the subscripts i and j refer to the ith parton in the proton and the jth parton in the antiproton, $f_p^i(x_i)$ gives the probability that ith parton in the proton carries a momentum fraction x_i and C_{ij} is the colour-averaging factor. The functions $f^i(x_i)$ are called parton distribution functions or parton densities. $\hat{\sigma}$ is the inclusive cross section for the partons p_i and p_j to form the particle c in the collision.

In $p\bar{p}$ collisions, W bosons are produced primarily by the annihilation of valence quarks, u or d from the proton(uud) and $\bar{d}$ or $\bar{u}$ from the anti-proton($\bar{u}\bar{u}\bar{d}$), as follows

$$u(p) + \bar{d}(\bar{p}) \rightarrow W^+ + X \quad \text{and} \quad \bar{u}(\bar{p}) + d(p) \rightarrow W^- + X$$

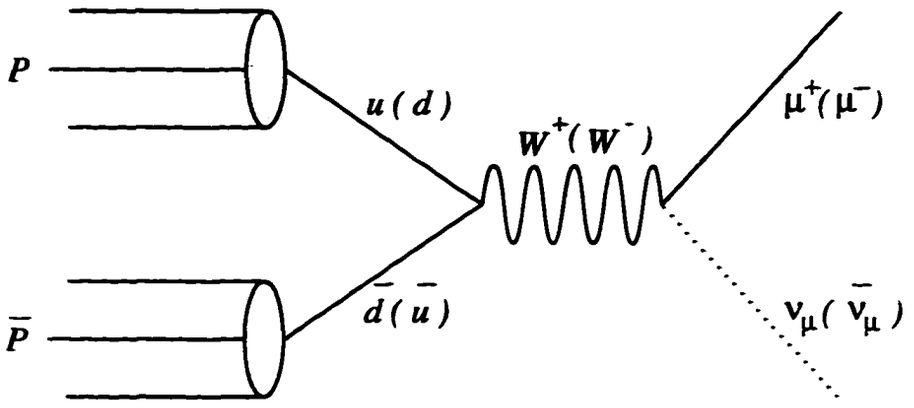

Figure 2.1: A cartoon of a $p\bar{p}$ collision producing a W^+ (W^-) which then decays to a muon, of the appropriate charge, and a neutrino (antineutrino).

The inclusive differential rapidity distribution for W^+ production can be written to the lowest order [4] as

$$\frac{d\sigma}{dy}(p\bar{p} \to W^+X) = K(y)\frac{2\pi G_F}{3\sqrt{2}}\, x_1 x_2 \{\cos^2\theta_C[u(x_1)d(x_2) + \bar{d}(x_1)\bar{u}(x_2)] + \sin^2\theta_C[u(x_1)s(x_2) + \bar{s}(x_1)\bar{u}(x_2)]\} \quad (2.2)$$

where, G_F is the Fermi constant, θ_C is the Cabibo angle and the functions u, d and s are the parton distribution functions of the up, down and strange quarks in a proton. They are in fact a function of both x and Q^2 , but, we have suppressed the second argument since in this example the quark density functions are evaluated at $Q^2 = M_W^2$. The subscripts 1 and 2 refer to the proton and the antiproton, respectively. The rapidity, with the z-axis along the proton beam, is

$$y = \frac{1}{2}\ln\left[\frac{(E + P_z)}{(E - P_z)}\right]. \quad (2.3)$$

The momentum fractions are constrained by

$$x_1 = \frac{M_W}{\sqrt{s}}\, e^{+y} \qquad \text{and} \qquad x_2 = \frac{M_W}{\sqrt{s}}\, e^{-y}, \quad (2.4)$$

where $\sqrt{s}$ is the centre of mass energy which is 1.8 TeV/c^2 at the Tevatron. K(y) is much like the Drell-Yan K-factor and corrects for QCD processes. It is independent of y to first

order and given by [3]

$$K \approx 1 + \frac{8\pi}{9}\,\alpha_S(M_W^2) \tag{2.5}$$

where α_S is the running strong coupling constant.

The differential cross section for W^- is obtained by switching the indices 1 and 2.

2.3 The W Charge Asymmetry

The W charge asymmetry is defined by

$$A(y_W) = \frac{[d\sigma/dy]_{W^+} - [d\sigma/dy]_{W^-}}{[d\sigma/dy]_{W^+} + [d\sigma/dy]_{W^-}}. \tag{2.6}$$

If a simplifying assumption of an SU(3)-symmetric sea is made, then $\bar{u}(x) = \bar{d}(x) = \bar{s}(x)$. This assumption, as we shall see later, is not borne out by experiment but it allows us to see some properties of the W charge asymmetry. The model used for theoretical calculations in this analysis does not use this assumption. Then, dropping small terms, one obtains [4]

$$A(y) \approx \frac{1}{D(\sqrt{s},y)}\left[\frac{u(x_1)-d(x_1)}{u(x_1)+d(x_1)} - \frac{u(x_2)-d(x_2)}{u(x_2)+d(x_2)}\right] + \frac{K(y)-K(-y)}{K(y)+K(-y)} \tag{2.7}$$

The function,

$$D(\sqrt{s},y) = 1 - \frac{u(x_1)-d(x_1)}{u(x_1)+d(x_1)}\frac{u(x_2)-d(x_2)}{u(x_2)+d(x_2)} + \frac{\bar{u}(x_1)+\bar{d}(x_1)}{u(x_1)+d(x_1)}\frac{\bar{u}(x_2)+\bar{d}(x_2)}{u(x_2)+d(x_2)} \tag{2.8}$$

is symmetric in the densities for partons 1 and 2. The x values available at the Tevatron, $0.01 < x < 0.3$, correspond according to (1.4) to a rapidity range of $-2.0 \leq y \leq 2.0$ for W boson production. It has been shown, by numerical calculation [4], that $K(y)$ is fairly constant at approximately 1.1 in the range $-1 < y < 1$ and $D \to 1$ as y approaches its maximum value. Also $K(-y)/K(y) = 1$ at $y = 0$ and 0.97 for $y < 1.5$. Thus we may write

$$A(y) \approx \left[\frac{u(x_1)-d(x_1)}{u(x_1)+d(x_1)} - \frac{u(x_2)-d(x_2)}{u(x_2)+d(x_2)}\right]. \tag{2.9}$$

Making the assumption that second order terms in d/u can be dropped, since deep inelastic scattering data indicate that $d < u$, gives

$$(u-d)/(u+d) \approx 1 - 2d/u.$$

This may be used to obtain

$$A(y) \approx 2\left[\frac{d(x_2)}{u(x_2)} - \frac{d(x_1)}{u(x_1)}\right]. \tag{2.10}$$

Thus, $A(y_W)$ provides direct information on the d/u ratio. Further, with the linear approximation $d(x)/u(x) = 1 - ax$,

$$A(y) \approx a\frac{M_W}{\sqrt{s}}\sinh y. \tag{2.11}$$

Thus $A(y_W)$ also yields the effective slope of the d/u ratio.

The W charge asymmetry can also be written in terms of the ratio of the structure functions of the neutron and the proton F_2^n/F_2^p [5]. The equation relating this structure function ratio to parton distribution functions is

$$1 - \frac{F_2^n}{F_2^p} \approx B\left[\frac{u-d}{u+d}\right], \tag{2.12}$$

where $B \equiv (u+d)/(4u+d+5s) \approx 1$ is a slowly varying function over the x values of interest. Comparing equations (1.9) and (1.12) gives

$$A(y) \approx B\left[\left.\frac{F_2^n}{F_2^p}\right|_{x_2} - \left.\frac{F_2^n}{F_2^p}\right|_{x_1}\right]. \tag{2.13}$$

Thus the W charge asymmetry measurement may be related to structure function measurements.

The ratio of structure functions have been made in different kinematic ranges by a number of deep inelastic scattering (DIS) experiments. These measurements are based on the fact that the differential cross section per nucleon for deep inelastic scattering, assuming single photon exchange, on an unpolarized target is related to the structure function $F_2(x,Q^2)$ and $R(x,Q^2)$ by [6]

$$\frac{d^2\sigma^{l\gamma}}{dx\,dQ^2} = \frac{4\pi\alpha^2 F_2(x,Q^2)}{Q^4 x}\left[1 - y - \frac{q^2}{4E^2} + \frac{y^2 + Q^2/E^2}{2(1+R(x,Q^2))}\right], \tag{2.14}$$

where, E is the incident lepton energy, $-Q^2$ is the four-momentum transfer, ν is the energy transfer, $y = \nu/E$ and $x = Q^2/2M\nu$ is the Bjorken scaling variable with M being the proton mass. The function $R(x, Q^2)$ is the ratio of the absorption coefficients for virtual photons of longitudinal and transverse polarizations respectively. Neglecting nuclear effects and that $R(x, Q^2)$ is target independent, $F_2^n/F_2^p = 2F_2^d/F_2^p - 1$, where, d refers to a deuteron target and p to a hydrogen target. Recent structure function measurements [1] and their kinematic ranges are summarized in Table 2.1.

Experiment [reference]	x-range	Q^2 -range GeV/c^2
E665 [7]	$10^{-6} \leq x \leq 0.3$	$10^{-3} \leq Q^2$
NMC [8] [9] [6]	$0.006 < x < 0.6$	$0.5 < Q^2 < 75$
BCDMS [10]	$0.06 \leq x \leq 0.80$	$8 \leq Q^2 \leq 260$
H1 [11]	$1.8 \times 10^{-4} < x < 0.13$	$4.5 < Q^2 < 1600$
ZEUS [12]	$3.0 \times 10^{-4} < x$	$10 < Q^2 < 4700$

Table 2.1: Recent structure function measurements.

The NMC has also obtained the Gottfried sum [13]. The Gottfried sum rule states that [14] [15]

$$S_G = \frac{1}{3}\int_x^1 dx' \left[u_v(x') - d_v(x')\right] + \frac{2}{3}\int_x^1 dx' \left[\bar{u}(x') - \bar{d}(x')\right] \tag{2.15}$$

If an SU(3)-symmetric sea is assumed ($\bar{u} = \bar{d} = \bar{s}$) then the second integral vanishes and the first term integrates to 1/3. The NMC has determined the sum from the ratio F_2^n/F_2^p, at Q^2 =4 GeV^2/c^2, to be $S_G = 0.235 \pm 0.0026$. This is significantly below the value of 1/3 predicted on the assumption of an SU(3)-symmetric sea. There have also been measurements at H2 collaboration at HERA and the BCDMS collaboration.

These measurements notwithstanding, important contributions can be made to our understanding of the parton distribution functions within the proton [4] using W charge

[1] E665 is a fixed target experiment located at Fermilab, the NMC and BCDMS experiments are located on the CERN-SPS and the H1 and ZEUS experiments are located on the HERA *ep* collider.

asymmetry measurements. The deep inelastic scattering (DIS) data require comparison of data from different targets which implies systematic uncertainties which are absent in charge asymmetry measurements. The DIS data do not directly cover the x-range covered at Tevatron energies. The parton distribution functions obtained from DIS data have to be evolved to the high Q^2 values useful at the Tevatron. Although the change with Q^2 is predicted to be small in leading order QCD, there are potential hidden uncertainties associated with higher twist components in the DIS data at low Q^2 .

2.4 The Decay of W Bosons

W bosons decay into $q\bar{q}$ channels about 72% of the time. At the DØ detector W bosons are identified mainly in the $e\nu_e$ and $\mu\nu_\mu$ decay channels because they have relatively clear experimental signals. The four-momentum of the W boson cannot be completely reconstructed because the longitudinal energy of the hard scatter cannot be accurately measured, for example, due to losses down the beam-pipe. Hence the charge asymmetry of decay leptons is measured. This poses no problem, in principle, to the program outlined above since the distribution of decay leptons from the decay of W bosons is well understood. Since the DØ detector does not possess a central field, the charge on electrons cannot be determined. However, the charge sign on muons can be determined from their deflection in magnetized iron toroids (see Chapter 3). Hence the charge asymmetry measurement is done solely using muons.

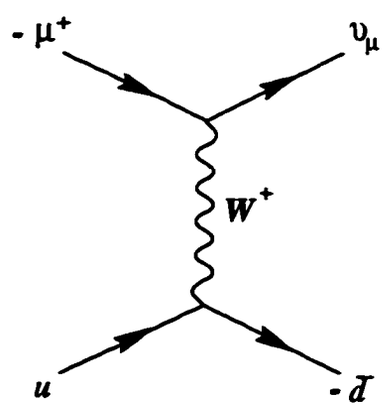

Figure 2.2: The process $ud \rightarrow \mu^+\nu$

The spin-averaged cross section for the process $ud \to \mu^+\nu$, shown in Fig. 2.2, is

$$\frac{d\hat{\sigma}}{d\cos\hat{\theta}} = \frac{|V_{ud}|^2}{\pi\hat{s}^2}\left[\frac{G_F M_W^2}{\sqrt{2}}\right]^2 \frac{(1+\cos\hat{\theta})^2}{(\hat{s}-M_W^2)^2 + (\Gamma_W M_W)^2} \tag{2.16}$$

where we have neglected the muon and the quark masses. The caret (^) denotes quantities in the W rest frame. In this frame, $\hat{\theta}$ is the angle between the $\bar{d}$ and the μ^+ directions and $\hat{s} = (p_u + p_{\bar{d}})^2$, where p_u and $p_{\bar{d}}$ are the four-momenta of the u and the $\bar{d}$ quarks that form the W, is the square of the centre of mass energy in the rest frame of the quarks and an invariant quantity. V_{ud} is the CKM matrix element and Γ_W is the total W decay width. The differential cross section vanishes at $\cos\hat{\theta} = -1$. This is dictated by the conservation of helicity in linear collisions (Fig.3.3) so that the μ^+ is preferentially emitted in the direction of the $\bar{d}$ which at the Tevatron is usually the direction of the $\bar{p}$ beam.

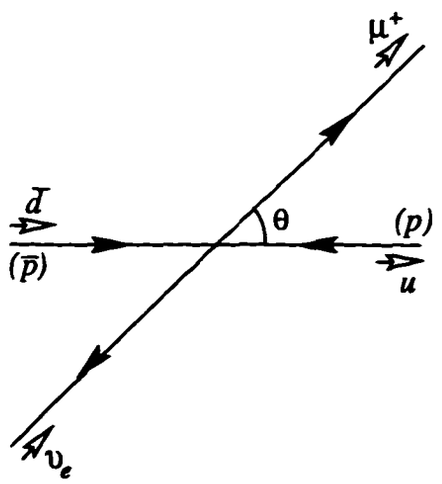

Figure 2.3: Helicities, denoted by the small open-headed arrows, and other relevant directions in the process $ud \to \mu^+\nu$

The rapidity of the decay muon in the c.m. frame is defined to be

$$\hat{\eta_\mu} = \frac{1}{2}\ln\left[\frac{E+P_L}{E-P_L}\right] = -\ln\left[\tan\left(\frac{\hat{\theta}}{2}\right)\right], \tag{2.17}$$

where E is the energy and P_L is the longitudinal momentum of the muon. In the laboratary frame it is

$$\eta_\mu = \frac{1}{2}\ln\left(\frac{x_1}{x_2}\right) + \hat{\eta_\mu}. \tag{2.18}$$

The decay angular distribution, in terms of the rapidity, may be written as

$$\frac{d\sigma_{\mu^+}}{d\eta_\mu} = \frac{1}{3}\int_0^1 dx_1 \int_0^1 dx_2 \{\cos^2\theta_C[u(x_1)d(x_2) + \bar{d}(x_1)\bar{u}(x_2)] + \sin^2\theta_C[u(x_1)s(x_2) + \bar{s}(x_1)\bar{u}(x_2)]\} \left\{\frac{d\hat{\sigma}}{d\cos\hat{\theta}}\sin^2\hat{\theta}\right\}. \tag{2.19}$$

For the negatively charged muon the above formula is true except that $\hat{\theta}$ is then the angle between the emitted μ^- and the incident d quark directions.

2.5 Origins of the Charge Asymmetry

The measured charge asymmetry is defined by

$$A\eta_\mu = \frac{d\sigma^+/d\eta_\mu - d\sigma^-/d\eta_\mu}{d\sigma^+/d\eta_\mu + d\sigma^-/d\eta_\mu}. \tag{2.20}$$

It owes its origins to two effects. Please refer to Fig 2.3 for this discussion. On one hand deep inelastic scattering data indicate that the u quark momentum distribution is harder than that of the d quark. This implies a charge asymmetry in the production of W bosons whereby W^+ have an average boost in the direction of the proton beam and W^- have an average boost in the direction of the antiproton beam. On the other hand the $(1+\cos\hat{\theta})^2$ term, which owes its origin to V-A interaction, gives a distribution where μ^+ are emitted preferentially in the direction of the antiproton beam and μ^- in the direction of the proton beam. This latter effect can also be seen as an effect of helicity conservation.

2.6 Event Generation

A fast Monte Carlo generator was used to generate W bosons. It should be noted that the simplifying assumption of an SU(3) symmetric sea used to explain the qualitative behaviour of the W charge asymmetry is not used in the following calculations.

The model assumes that the cross section can be factorized as

$$\frac{d^3\sigma}{dydp_T^W dm} = \frac{d^2\sigma}{dydp_T^W}\cdot\frac{d\sigma}{dm} \tag{2.21}$$

where dp_T^W represents the momentum of the W boson, y the rapidity and m is its mass. A relativistic Breit-Wigner shape is used to model the W resonance line shape

$$f(m) = \frac{m^2}{(m^2 - M_W^2)^2 + \frac{m^4\Gamma_W^2}{M_W^2}} \tag{2.22}$$

The probability that a quark and antiquark in the $p\bar{p}$ interaction produce an object of mass m falls with increasing mass and the mass spectrum of W bosons produced in $p\bar{p}$ collisions is different from the Breit-Wigner shape. The modifying factor is obtained as follows [16].

The differential cross section for vector boson production is given by

$$\frac{d^2\sigma}{dx_1 dx_2} = f_p^i(x_i).f_{\bar{p}}^j(x_j)\hat{\sigma}(m^2), \tag{2.23}$$

where $f_p^i(x_i)$ and $f_{\bar{p}}^j(x_j)$ are the parton distribution functions for the ith quark or antiquark in the proton and the jth antiquark or quark in the antiproton. Although, this discussion will focus on one pair, the relations derived are summed over all quark pairs that give a W boson of mass m, with cross section $\hat{\sigma}(m)$, and averaged over initial color states. Equation (3.1) is the total cross section obtained by integrating the above.

Changing variables from (x_i, x_j) to (x_i, m^2) using $m^2 = x_i x_j s$, where s is the centre of mass energy, and integrating over x_i gives

$$\begin{aligned} \frac{d\sigma}{dm} &= \frac{2m}{s}\int_{\frac{m^2}{s}}^1 \frac{dx_i}{x_i} f_p^i(x_i).f_{\bar{p}}^j\left(\frac{m^2}{sx_i}\right)\hat{\sigma}(m^2) \\ &= \frac{1}{m}\,\mathcal{F}\,\hat{\sigma}(m^2), \end{aligned} \tag{2.24}$$

where,

$$\mathcal{F} = \frac{2m^2}{s}\int_{\frac{m^2}{s}}^1 \frac{dx_i}{x_i} f_p^i(x_i).f_{\bar{p}}^j\left(\frac{m^2}{sx_i}\right) \tag{2.25}$$

is referred to as the parton luminosity although it is dimensionless. It is parameterized as $e^{-\beta m}$ [16]. The differential cross section for W bosons in this approximation is given by

$$\frac{d\sigma}{dm} = \frac{e^{-\beta m}}{m}\,\frac{m^2}{(m^2 - M_W^2)^2 + \frac{m^4\Gamma_W^2}{M_W^2}} \tag{2.26}$$

Parton distribution functions supplied by PDFLIB [17] are used to calculate the mass distribution. The calculation is done separately for the cases where atleast one of the quark involved is a sea quark and when both of them are sea quarks. W bosons of both charges are generated and the polarization is correctly chosen. The polarization of W^+ is opposite the proton direction except for the sea-sea interaction in which the $\bar{d}$ quark originates in the proton. This is the case in half the sea-sea interactions for which the W^+ polarization is the same as the proton direction. As seen above the polarization of the W boson plays an important part in manifesting the charge asymmetry.

The transverse momentum and rapidity of the W is selected at random from calculations of $d\sigma/(dydp_T^W)$ for different parton distribution functions provided by the authors of [18]. In addition to handling the conventional perturbative regime, they take into account the effect of initial state radiation of soft gluons, which does not lend itself to a perturbative treatment, in a resummation formalism. Please refer to [18] and [19] for more details on this method.

Events are generated at $\sqrt{s} = 1.8$ TeV and the event vertices are generated to give a Gaussian distribution with a mean (0 cm) and root mean square (25 cm) consistent with data. Both W^+ and W^- are generated.

The angular distribution of the decay leptons depends on whether the quarks that formed the W are valence or sea. For W^+ the cross section may be written as [16]

$$\begin{aligned}\frac{d^2\sigma}{d\cos\theta^*} &\sim (1-\cos\theta^*)^2\left[\frac{1}{2}\frac{d\sigma_s}{dy}+\frac{d\sigma_v}{dy}\right] + (1+\cos\theta^*)^2\,\frac{1}{2}\,\frac{d\sigma_s}{dy} \\ &\sim (1-\cos\theta^*)^2\,\frac{d\sigma_v}{dy} + (1+\cos^2\theta^*)\,\frac{1}{2}\,\frac{d\sigma_s}{dy} \qquad (2.27)\end{aligned}$$

where the subscripts v and s refer to valence and sea quarks and θ^* is the angle of the lepton with respect to the proton direction ($+Z$-axis) in the centre of mass frame. This equation is used for the angular distribution of leptons in θ^* while the ϕ of the lepton is generated at random to lie between 0 and 2π. The leptons are then boosted into the laboratory frame using the four vector of the generated boson. A cut of $p_T \geq 20$ GeV/c is applied to correspond to the cut applied to the muons in data. Figure 3.4 shows the charge asymmetry of leptons from W decays for various modern parton distribution func-

tions. Note that the muon momentum was not adjusted according to measured detector momentum resolution.

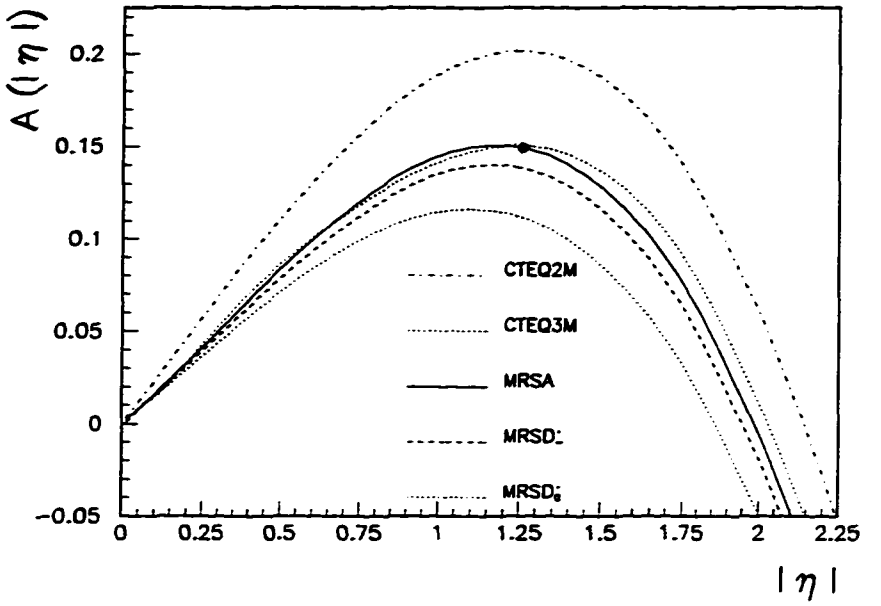

Figure 2.4: Theoretical prediction of the charge asymmetry of leptons from W decay for various modern parton distribution functions.

2.7 Motivation

As has been explained above it is important that parton distribution functions be fit with data obtained at high Q^2 values comparable with the W boson mass since DIS data cannot be reliably extrapolated to this regime. Two measurements at the Fermilab collider that will benefit from a good understanding of parton distribution functions are those of the total width of the and the W boson mass.

The W boson total width is an important test of the electroweak sector of the Standard Model and its departure from currently expected theoretical value could be an indication of new phenomena such as new decays of W or the existence of heavier electroweak gauge bosons [4]. Hadron colliders measure the ratio of the cross sections of W and Z

bosons in leptonic decay channels, for example,

$$R = \frac{\sigma_W . Br(W \rightarrow \mu\nu)}{\sigma_Z . Br(Z \rightarrow \mu^+\mu^-),}$$

This can be used in the following equation to obtain the total decay width of the W boson [20]:

$$\Gamma_W = \frac{\sigma_W}{\sigma_Z} \cdot \frac{\Gamma_Z}{\Gamma(Z \rightarrow \mu^+\mu^-)} \cdot \frac{\Gamma(W \rightarrow \mu\nu)}{R} \tag{2.28}$$

using high precision LEP measurements for $\Gamma(Z^o \rightarrow \mu\mu)/\Gamma_Z$ [1], and theoretical values for the ratio of the total W and Z boson cross sections, σ_W/σ_Z, [21] and the decay width $\Gamma(W \rightarrow \mu\nu)$ [22]. The major source of uncertainty here is the error on σ_Z/σ_W which in turn stems from the uncertainty in the ratio of the quark densities $u(x)$ to $d(x)$.

Knowledge of the mass of the W boson will enable better theoretical limits to be imposed on the mass of the Higgs boson (Section 1.3). Measurement of the W boson mass using the DØ detector is based on $W \rightarrow e\nu$ decays. The most recent value is 80.44 $\pm$ 0.11 GeV/c^2 . It is determined from a likelihood fit to the measured transverse mass, M_T^W, with templates generated, by Monte Carlo simulations, for different M_T^W values [23]. The momentum distribution of partons, described by parton distribution functions, determine the longitudinal momentum, $p_L^W = (x_1 - x_2)p_{\text{proton}}$, of the W boson and alter the mass spectrum of the W boson from the relativistic Breit-Wigner shape through the relation $m^2 = x_1 x_2 s$ and through the dependence of the production cross section on x_1 and x_2. The systematic error ascribed to the variation of M_T^W when different PDFs are input to the Monte Carlo simulations is 21 MeV/c^2 .

Currently the fits to the M_T^W distribution yields the smallest uncertainty. However, in the next run (Run 2) a better value may be obtained by fits to the transverse momentum distribution of decay electrons. The M_T^W method depends on the measurement of the missing transverse energy which degrades rapidly with luminosity. The Run 2 luminosity is expected to be an order of magnitude larger (see Chapter 9) than in Run 1. The uncertainty in the W mass from PDFs from p_T^e fits is currently 48 MeV/c^2 . Improving the p_T^e method is another strong motivation for understanding the W charge asymmetry.

CHAPTER 3

THE DØ DETECTOR

3.1 Introduction

The data used in this analysis were collected using the Tevatron accelerator and the DØ detector during the years 1992-1995. This chapter describes the Fermilab accelerator and the DØ detector with emphasis on the detection of muons since this analysis is based on the identification of muons resulting from the decay of W bosons .

3.2 The Fermilab Tevatron

The Fermilab Tevatron is presently the highest energy particle accelerator in the world. It collides protons and antiprotons with a centre-of-mass energy of $\sqrt{s}$=1.8 TeV/c^2 . A schematic overview of the acceleration process is presented in Fig. 3.1. A more detailed description than the one presented below may be found in [24].

The proton beam originates at a magnetron surface-plasma source as a 50 mA beam of 18 keV negative hydrogen ions (H^-) pulsed at 15 Hz. A five stage Cockroft-Walton accelerator increases the H^- ion energy to 750 keV . The beam then passes into the Linac through an electrostatic chopper which controls the beam current to the Linac. This is called the preaccelaration stage.

The Linac is a two stage linear accelerator that outputs a pulsed beam of H^- ions at 400 MeV . A carbon foil strips the electrons from the H^- ions before they enter the Booster. The Booster, a 151 m diameter fast cycling proton synchrotron, accepts 15 Hz pulses of bare protons and energizes them to 8 GeV before injecting them into the Main Ring. The Main Ring is a proton synchrotron with a radius of 1 km. It performs two functions. It outputs a beam of 120 GeV protons into the PBar (antiproton) source for producing antiprotons. The process of accumulating antiprotons is called stacking

and continues even when beams are colliding in the Tevatron. Secondly, it accelerates protons extracted from the booster and antiprotons from the PBar source from 8 GeV to 150 GeV before injecting them into the Tevatron for final acceleration to 900 GeV .

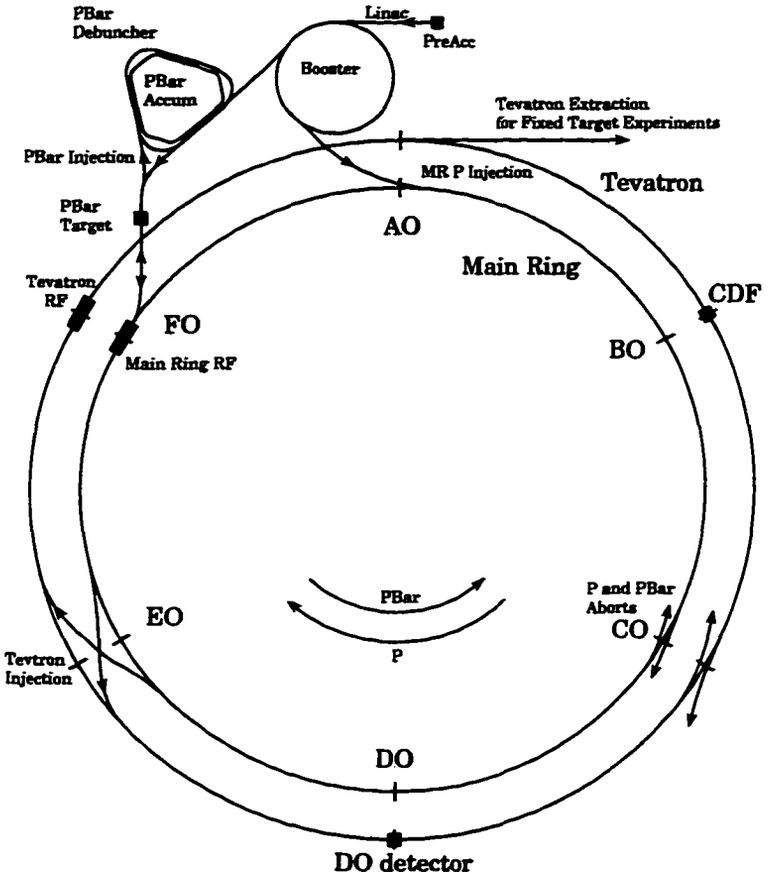

Figure 3.1: An overview of the accelerator

The PBar source accepts 83 bunches of 120 GeV protons from the Main Ring. Here for every 10^{12} protons that impinge upon a nickel target a yield of 10^{7} antiprotons, with an energy of about 8 GeV , is obtained. A cylindrical lithium lens collimates the beam and directs it via a transport line to the Debuncher. Here the momentum spread of the beam is lowered, i.e., the beam is debunched, by reducing the RF voltage over a few milliseconds. Beam pickups measure the transverse position of antiprotons and special magnets called Kickers apply small corrective "kicks" to reduce the transverse momentum of the beam. This process is called stochastic cooling. The antiprotons are then transferred to the

Accumulator where they undergo further stochastic cooling and are held for injection into the Main Ring. The store of antiprotons in the Accumulator is called a stack. The Debuncher and the Accumulator share the same tunnel.

The Tevatron is located 60 cm below the Main Ring in the same tunnel. It uses 774 dipole and 216 super-conducting magnets that operate at a temperature of 4.6° K. It accepts six proton and six antiproton bunches ($\approx 1.5 \times 10^{11}$ particles in each bunch) from the Main Ring and ramps them up to an energy of 900 GeV in each counter-rotating beam. Special super-conducting quadrupoles, called low-beta Quads, squeeze the beams till the transverse cross-section of the beam is only about 40 μm at the two luminous points, B0 and D0. The CDF and DØ detectors are centred at these points where a beam crossing occurs every 3.5 μs . The longitudinal distribution of event vertices as measured by DØ tracking chambers is Gaussian with a standard deviation of approximately 30 cm about z=0 cm.

3.3 The DØ Detector

The DØ detector was designed to study phenomenon involving large transverse momentum transfers, p_T, in $p\bar{p}$ collisions. Examples of such processes are the production off W and Z bosons and high transverse momentum jets. The detector has been used to make sensitive tests of the electroweak theory, and enhance our understanding of perturbative QCD and the production and decay of hadrons composed of b quarks. Searches for new phenomena and and particles that reveal themselves in this high p_T regime are also an important ongoing effort. In fact the primary physics goal of the two detectors at the Tevatron, DØ and CDF (Collider Detector Facility) was to search for the top quark. This culminated on March 3, 1995 with simultaneous announcements by both the experimental groups at Fermilab [25] [26]. These objectives placed specific demands on the design of the detector. It is beyond the scope of this chapter to explore each one in detail and only those aspects relevant to the analysis at hand is dealt with below. A more extensive description may be found in reference [27].

Fig 3.2 shows the elevation view of the DØ detector. Moving radially away from

the beam axis, one encounters, in order, the central tracking and transition radiation detectors, a hermetic uranium-liquid argon calorimeter, and finally the muon spectrometer consisting of a toroidal magnet and arrays of proportional drift tubes.

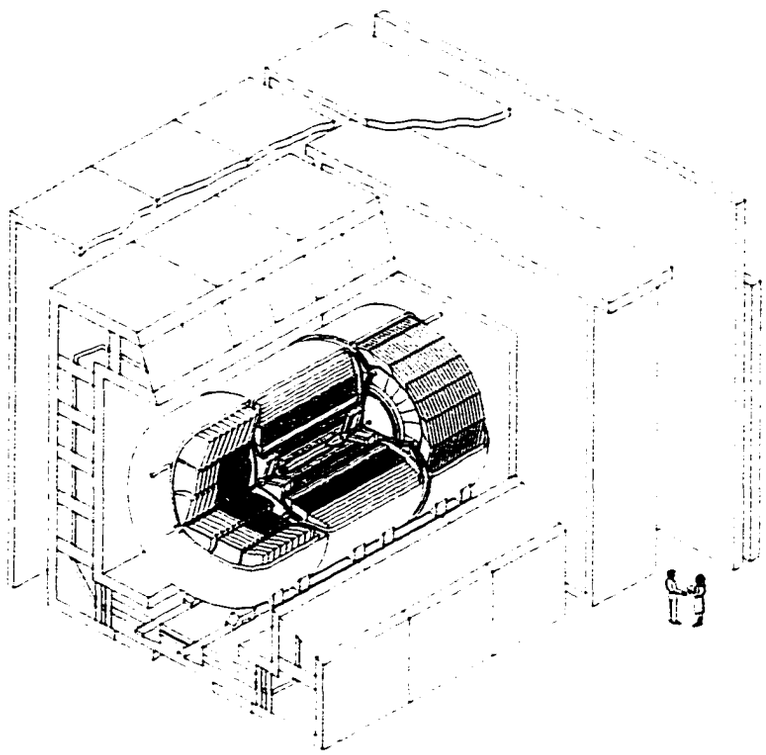

Figure 3.2: Cut away view of the DØ detector

The coordinate system used is a right handed one with the z-axis along the the proton beam direction and the y-axis along the vertical. The azimuthal angle θ is zero along the proton beam direction and the polar angle ϕ is measured from the x-axis. Another useful quantity is the pseudorapidity, $\eta = -ln[tan(\theta/2)]$, which approximates the true rapidity, $y = 1/2ln[(E + p_x)/(E - p_x)]$, for finite angles, in the limit $(m/E) \rightarrow 0$.

3.4 The Central Detectors (CD)

The DØ detector lacks a central solenoidal magnetic field for tracking. The components of the tracking system, shown in Fig. 3.3, include the vertex (VTX) chamber, the central drift chamber (CDC) and a pair of forward drift chambers (FDC). These were designed to give good track resolution and to distinguish between single electrons and conversion pairs by ionization energy measurement. A transition radiation detector (TRD) exists between the VTX chamber and the CDC to aid discrimination between electrons and pions.

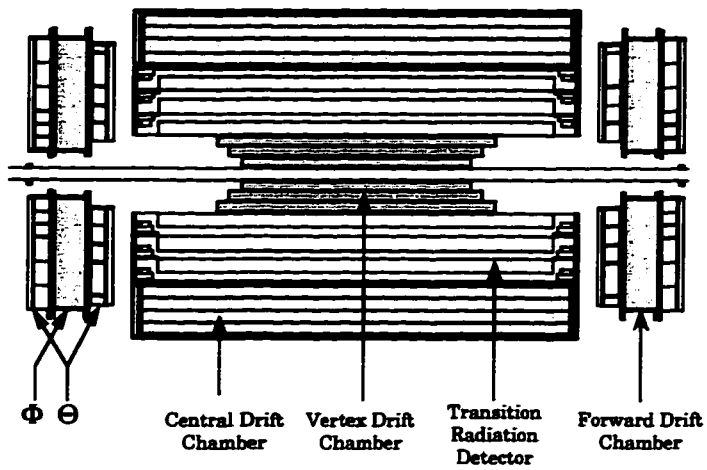

Figure 3.3: The DØ central and tracking detectors

3.4.1 Vertex Chamber (VTX)

This is the innermost of the tracking chambers with an inner radius of 3.7 cm and an outer active radius of 16.2 cm with three concentric layers of cells. The innermost shell has 16 cells and the outer two have 32 cells each. Fig 3.4 shows one quadrant. In each cell eight sense wires provide a measurement of the $r-\phi$ position. Adjacent sense wires are staggered by $\pm$ 100 μm to resolve left right ambiguities; the cells of the three layers are offset in ϕ to aid further pattern recognition and calibration. The gas used in this drift chamber is CO_2(95%)-ethane(5%) and a small amount of H_20 at one atmosphere. The average drift velocity under normal operating conditions ($\langle E \rangle \sim$1 kV/cm) is about 7.3

μm /ns and a maximum drift time of 2.2 μs . The vertex resolution along the z-axis is approximately 1.5 cm [28].

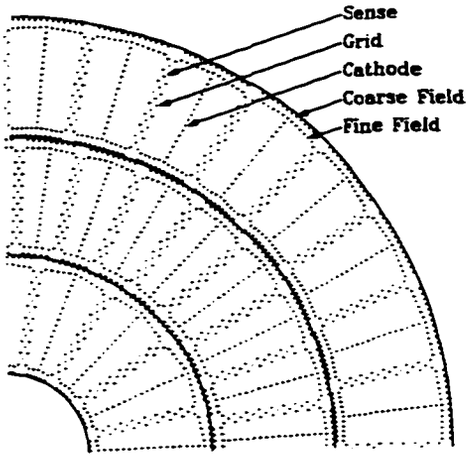

Figure 3.4: One quadrant of the vertex detector

3.4.2 Transition Radiation Detector (TRD)

The TRD provides a means of identifying electrons and rejecting pions independently of the calorimeter. Transition radiation is produced when highly relativistic particles ($\gamma > 10^3$) cross the boundary between media with different dielectric constants [29]. The total energy emitted per interface crossing [30] [31] is $W = (2/3)\alpha_{em}\omega_p\gamma$, where $\omega_p = (4\pi\alpha_{em}ZN_A\rho)/Am_e$, is the plasma frequency of the medium of density ρ. Most of the radiation is emitted within a distance called the formation length $D = (\gamma c)/\omega_p$. For a medium of unit density $\omega_p = 3 \times 10^{16}$ s^{-1} and D is tens of microns for a charged particle moving through it with γ=1000. At γ=1000, the radiation is in the form of X-rays. Since $\gamma = E/(mc^2)$ the total energy radiated is related to the mass of the charged particle this fact is used to discriminate between electrons and pions. The factor of α_{em} means that the probability for emission per transition is small. However, the radiation is forward peaked, as is characteristic of all relativistic radiation phenomenon. Thus the intensity can be improved by using a cylindrical stack of a large number of thin foils tens of microns thick, separated by air, so that transition radiation may be emitted at each face of the foil as a particle moves radially outwards. For materials commonly used and for

γ in the vicinity of 1000, the radiation falls in the X-ray regime of the electromagnetic spectrum.

The DØ TRD consists of three separate concentric cylinders, each with a radiator

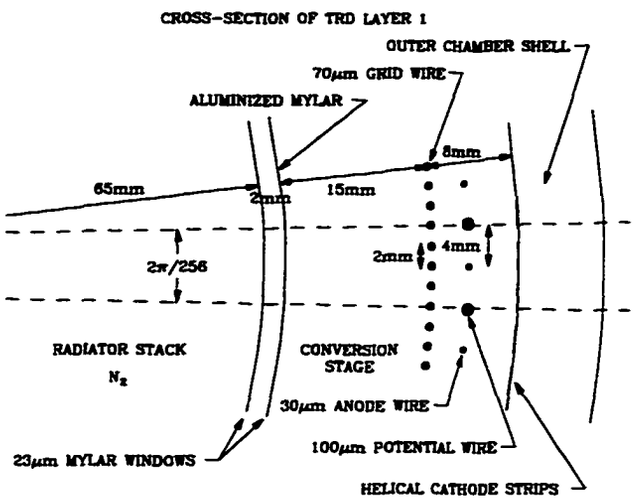

Figure 3.5: A slice of the transition radiation detector (TRD)

and an X-ray detector. The radiator consists of 393 polypropylene foils, 18 μm thick, in a volume filled with N_2. The mean gap between foils is 150 μm . The energy distribution peaks at 8 keV and is contained mainly below 30 keV . The detector is a two-stage time-expansion radial-drift proportional wire counter mounted just after the radiator. Fig. 3.5 shows a radiator followed by the conversion and amplification stages of the detector. The X-rays convert mainly in the first stage and the resulting charge drifts radially outward to the sense cells where the avalanche occurs. Ionization is also produced by all the charged particles traversing the conversion and amplification gaps. The cumulative charge is gathered over the full drift time interval of 0.6 μs . The pulse height and the arrival time of the charge clusters is used to distinguish electrons from pions.

3.4.3 Central Drift Chamber (CDC)

The CDC [32] is of cylindrical construction, concentric with the beam axis and and spans the space between the TRD and the central calorimeter(CC). It is 184 cm long with its inner radius at 49.5 cm and its outer radius at 74.5 cm from the beam axis. Fig 3.6

shows the end view of one section. It has four concentric rings, each with 32 azimuthal cells. Each cell in one layer is offset from its neighbours in adjacent layers by one half-cell to aid pattern recognition. Straddling the radial bisector of each cell are seven axial gold-plated

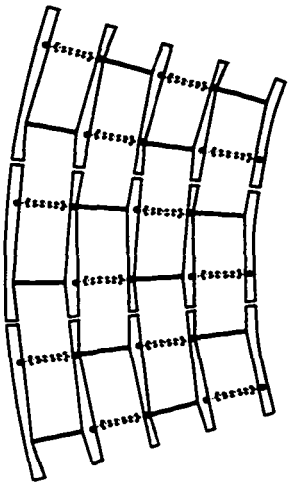

Figure 3.6: A section of the central drift chamber (CDC)

32 μm tungsten wires placed at increasing radii. These are staggered in the ϕ-coordinate by $\pm$ 200 μm to resolve the left-right ambiguity in each cell and are read out at one end. Surrounding the sense wire array is a grid of fourteen ground potential wires that isolate the sense wires from their neighbours. Embedded in the walls of the cell immediate to the first and the last sense wires are delay lines. These are inductive coils wound on a carbon fibre epoxy core. To isolate the delay lines better from the inner sense wires, the first and last sense wires have an additional ground wire inner to them. A gas mixture of Ar(92.5%)CH_4(4%)$C0_2$(3%)H_20(0.5%) is used. The inner sense wires are set at 1.45 kV while the outer sense wires are set 1.58 kV so that they induce a large signal on the delay lines. The r-ϕ position is determined by the drift time to the sense wires. The r-ϕ resolution measured from the residuals of hits for fully reconstructed tracks is 150-200 μm . The z-position is determined by the difference in the arrival time of a pulse, induced by the nearest anode wire, at the two ends of a delay line. The z-coordinate resolution is approximately 2 mm.

A single layer of 128 scintillating fibres each 1 mm in diameter, aligned parallel to the

beam axis, exists between the CDC and the CC covering 1/32 of the full azimuth. This detector is useful in regaining calibration constants when operating conditions change and to improve the knowledge of drift time versus distance relation of the CDC.

3.4.4 Forward Drift Chambers (FDC)

The FDC [32] [33] are located at either end of the VTX-TRD-CDC barrel and extend tracking coverage in the forward region down to $\theta = 5°$ at each end of the CDC. They are made up of one Φ chamber sandwiched between two Θ chambers shown separated in Fig. 3.7.

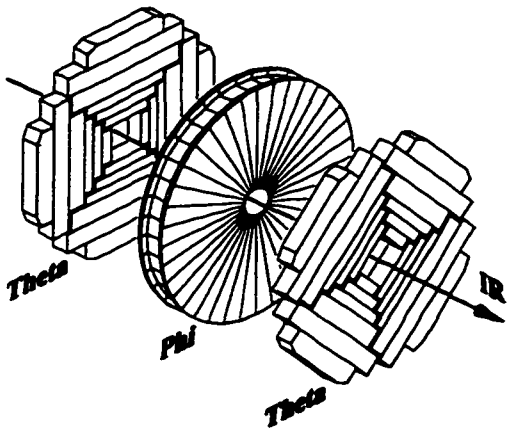

Figure 3.7: The forward drift chambers (FDC)

Each Φ chamber is a single chamber with 36 sectors over the full azimuth, each with 16 anode wires along the z-coordinate. Each Θ chamber consists of four individual quadrants with six rectangular cells at increasing radii. Each cell has eight anode wires in z and one delay line to give a local measurement of the orthogonal coordinate. The two Θ modules are rotated by 45° with respect to each other. The side walls of the Θ and Φ cells and the front and back of each module have conductive coatings. The Θ module also employs two grounded wires between adjacent anodes as in the CDC. The FDC uses the same gas and operating voltages as the CDC with similar values for gas gain. The resolution measured from the residuals of hits for fully reconstructed tracks is 150-200 μm in the drift direction r-ϕ for the Φ chamber and r-θ for the Θ chambers.

3.4.5 Central Detector Electronics

The electronics employed for read out are almost the same for all CD devices with three stages of signal processing: preamplification is done locally on the chambers, shaping is done at the detector platform and the flash ADC digitizers are located in the second floor moving counting house (MCH). Further digital signal processing is considered part of the data acquisition system (DAQ).

3.5 Calorimeter

Calorimeters measure the energy of incident particles which interact in a large mass generating secondary particles, which may do likewise, until the energy of the incident particle appears as ionization or excitation in the calorimeter medium.

The DØ calorimeter helps in the identification of electrons, photons, jets and muons. At DØ calorimetry is the only means of measuring the energy of electrons, photons and jets since a central magnetic field is absent. Being a sampling calorimeter it measures energy at only a few points along the path of a shower rather than measuring its total energy. Sampling calorimeters use an active medium, in this case liquid argon (LAr), contained between inactive materials, such as depleted U^{232}, Cu or stainless steel to reduce the effective radiation and absorption lengths thus making the detector more compact and cheaper. LAr has unit gain, is easy to calibrate and relatively insensitive to radiation damage. U^{232} is used to enhance the energy released by hadronic shower. Fast neutron and photon induced fission of U^{232} releases energy in the form of gamma ray photons which would otherwise be lost due to nuclear breakup.

The DØ calorimeter consists of three sections: the central (CC) covers the pseudorapidity range $|\eta| < 1$ and the end modules to the north (ECN) and south (ECS) provide coverage up to $|\eta| \approx 4.0$. Each calorimeter has three different modules. Radially outward, closest to the beam axis, is the electromagnetic (EM) section with thin U^{232} absorber plates, next is a fine hadronic section with thicker U^{232} plates and finally a coarse hadronic section with thick copper or stainless steel plates. At η=0, the CC depth is 7.2 nuclear absorption lengths, λ_A, and at η=4 the EC depth is 10.3 λ_A.

A typical calorimeter cell is shown in Fig. 3.8. The absorber plate is grounded and to the G-10 resistive coated copper pads, a voltage of +(2.0-2.5) kV is applied. Electron drift time across the 2.3 mm gap is $\approx$ 450 n .

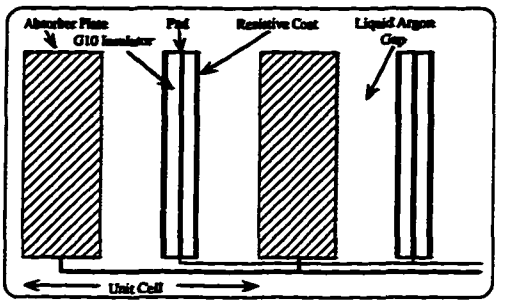

Figure 3.8: A typical cell of the calorimeter

The cells are arranged in a 'pseudo-projective' [1] set of readout towers. Figure 3.9 shows a section of the calorimeter with this segmentation pattern. Typical transverse tower size in both the EM and hadronic sections is $\Delta\eta \approx \Delta\phi \approx 0.1$. The third layer of the EM calorimeter, where EM shower maximum is expected has finer segmentation of $\Delta\eta \approx \Delta\phi \approx 0.5$.

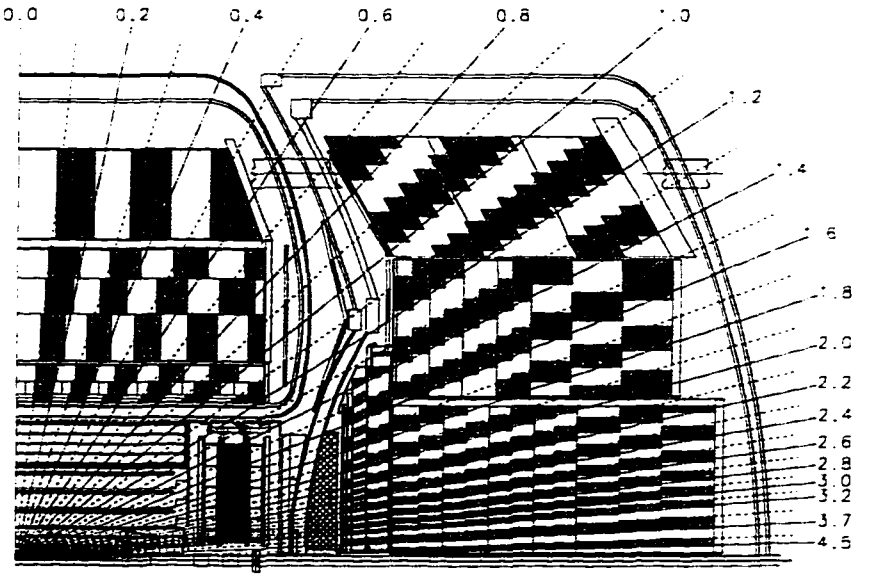

Figure 3.9: Tower geometry of the calorimeter

[1] the centers of the cells of increasing shower depth lie on rays pointing to the centre of the interaction region, but the cell boundaries are perpendicular to the absorber plates

The energy resolution is parameterized by

$$\left(\frac{\sigma}{E}\right)^2 = C^2 + \frac{S^2}{E} + \frac{N^2}{E},$$

where the constants C, S and N represent the calibration errors, sampling fluctuation and noise contributions, respectively. For electrons, the resolution constants are

$$C = 0.003 \pm 0.002,\ S = 0.157 \pm 0.005\ (\text{GeV})^{\frac{1}{2}},\ N \approx 0.140\ \text{GeV},$$

and for pions, they are

$$C = 0.032 \pm 0.004,\ S = 0.41 \pm 0.04\ (\text{GeV})^{\frac{1}{2}},\ N \approx 1.28\ \text{GeV}.$$

This analysis uses the calorimeter to ensure that a tower, with energy consistent with a minimum ionizing particle, matches a muon track. This reduces the contamination of the data sample by cosmic ray muons since these arrive from all directions and only a small fraction will point to the beam axis along the direction of a tower. It is also used to measure missing transverse energy in the event which is used to compute the transverse energy of the neutrino accompanying the decay of the W boson .

3.6 Intercryostat Detectors (ICD) and Massless Gaps

The region $0.8 \leq |\eta| \leq 1.4$, between the central and end cryostats, contains a large amount of uninstrumented material in the form of cryostat walls, stiffening rings and module end-plates. Two arrays of scintillation counters called the ICD, each with 384 Bicron BC-414 scintillator matching the calorimeter cell size of $\Delta\eta = \Delta\phi = 0.1$, are used to correct for energy deposited in the uninstrumented walls. Separate single cell structures called massless gaps also exist in the CC and the EC. Together, the ICD and the massless gaps provide a good approximation to the standard DØ sampling of EM showers.

3.7 Level Zero Detector

This detector registers the presence of inelastic collisions and serves as a luminosity monitor. As shown in Fig, 3.10, it consists of two hodoscopes of scintillation counters

mounted on the outer surfaces of the end calorimeters. These hodoscopes have a checkerboard-like pattern of scintillators with partial coverage for $1.9 < |\eta| < 4.3$ and almost full coverage for $2.3 < |\eta| < 3.9$. The rapidity coverage is such that the coincidence probability of both detectors is more than 0.99 for non-diffractive collisions. The z-coordinate is determined from the difference in the arrival time of particles at the two level 0 detectors.

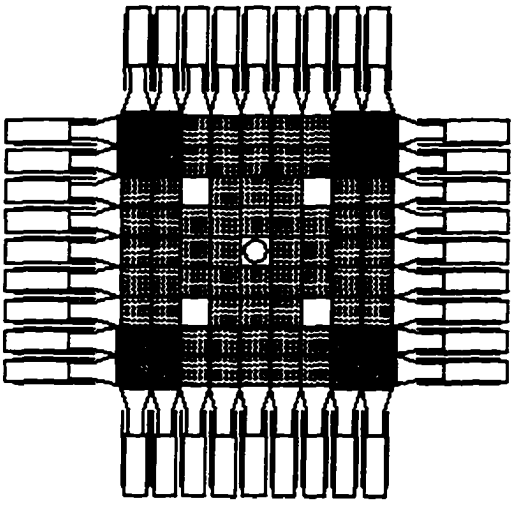

Figure 3.10: One of the Level Zero detectors

Non-diffractive inelastic collisions are selected by requiring Level 0 coincidence and $|z_{vtx}| < 100$ cm. The vertex cut ensures that events originate in beam-beam and not beam-gas or beam-halo interactions. These events allow calculation of the Tevatron luminosity. Scalers count live crossings, coincidences satisfying the vertex cut and single hits in groups of similar counters with and without valid coincidences. This allows the luminosity to be measured independently for each beam bunch [34] [35].

3.8 Muon Spectrometer

The DØ muon spectrometer consists of five separate toroids together with three layers of proportional drift tube chambers (PDT's). Hits in the inner layer (A) together with the interaction point provides a measurement of the track before it is bent by the toroidal magnetic field. Two more layers (B & C) outside the toroids provide a measurement after

the bend. Knowledge of the bend angle and the magnetic field allow the momentum of the muon track to be computed. In the central region, the error in muon momentum measurement can be represented by

$$\sigma(1/p)/(1/p) = \sqrt{(0.18(p-2)/p)^2 + ((0.003 \pm 0.001)p)^2}$$

where the muon momentum, p, is in GeV/c . The first term under the radical sign is due to multiple Coulomb scattering while the second term is due to chamber resolution.

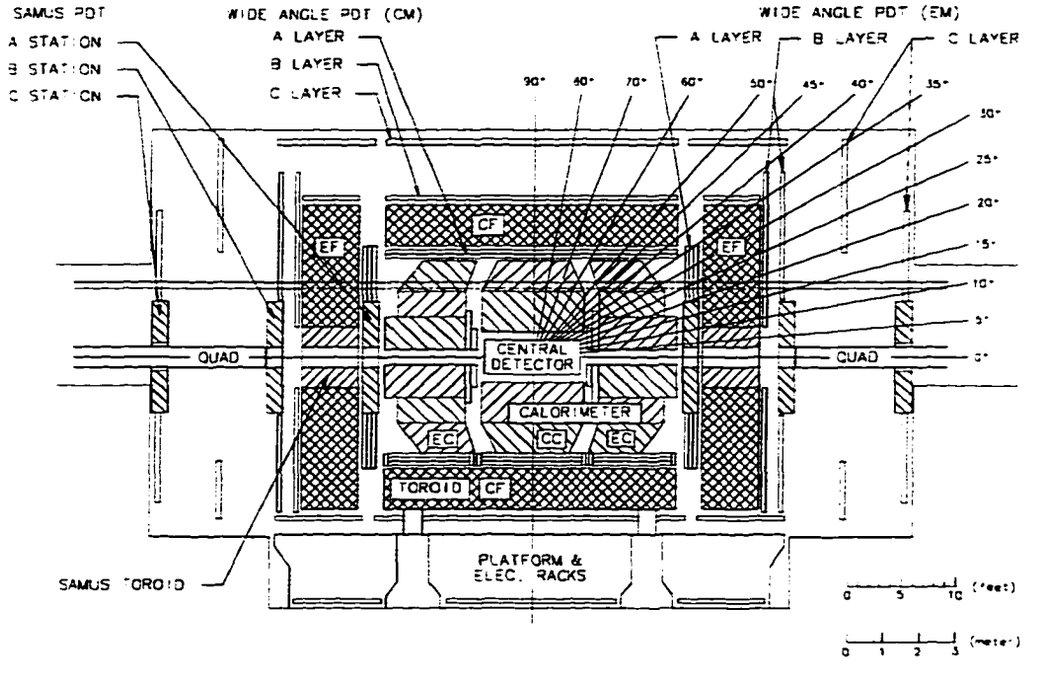

Figure 3.11: Elevation view of the DØ detector showing the location of the muon spectrometer components

The central (CF) toroid, covering $|\eta| \leq 1.0$, and the two end (EF) toroids, covering $1.0 < |\eta| \leq 2.5$, belong to the wide angle muon system (WAMUS). The small angle muon system (SAMUS) toroids are located in the central hole of the EF region toroids. The metre thick CF region toroid is a square annulus in centred on the the beam. A current of 2500 A gives a field of 1.9 T. The fringe field near the interaction point is 0.01 T. The EF region toroids also carry a current of 2500 A giving a maximum field

of 2T. The EF region toroids on each end have a square inner hole centred at the beam line and it is here that the SAMUS toroids rest. These carry 1000 A giving a field of 2T. The magnetic field has the same direction in all five toroids during data taking. The field was defined to be forward polarity when the field lines were wound counter-clockwise viewed toward the positive z-axis. The opposite case represents reverse polarity.

For tracking and triggering purposes, the muon system is divided into convenient geometric regions. These are listed in Table 3.1 along with their pseudorapidity coverage and the type of proportional drift tube used.

Region	Coverage	WAMUS PDT's	SAMUS PDT's
CF	$\|\eta\| < 1.0$	Yes	No
EF	$1.0 < \|\eta\| < 1.7$	Yes	No
Overlap	$1.7 < \|\eta\| < 2.5$	Yes	Yes
SAMUS	$2.5 < \|\eta\| < 3.4$	No	Yes

Table 3.1: Geometric regions, pseudorapidity coverage of the muon system and the type of PDT's used.

Due to high trigger rates, limited bandwidth and difficulty in reconstructing track and momenta, due to mixed orientations and types of detectors, there were no high p_T triggers in the Overlap region during normal running.

The calorimeter and the toroids present a fairly thick shield against hadronic punch-through [36]. Fig. 3.11 shows the number of nuclear interaction lengths presented by the calorimeter and the toroids. The probability for hadronic punch-through has been measured using a test beam [37]. The material distribution and detection system in this experiment closely resembled that of the DØ detector. The punch-through probability for 200 GeV hadrons is of the order 10^{-5}.

As seen from Fig. 3.11, WAMUS chambers are arranged in three layers. They all have the same basic cell structure but may vary in length, width or number of decks.

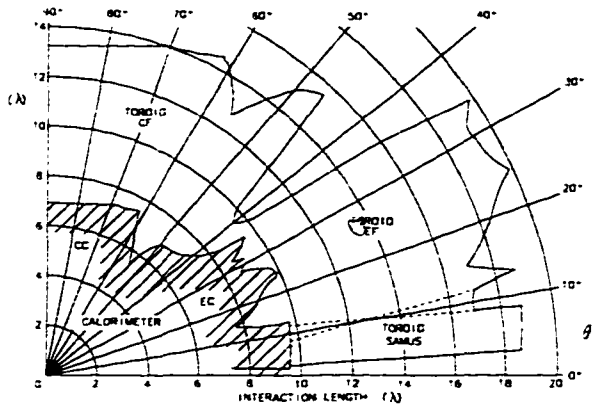

Figure 3.12: Interaction lengths in the DØ detector

A-layer chambers have four decks of cells while B- and C-layer chambers have three decks. The decks of cells are staggered so as to yield position information up to that of a half cell and to break the left-right drift-time ambiguity.

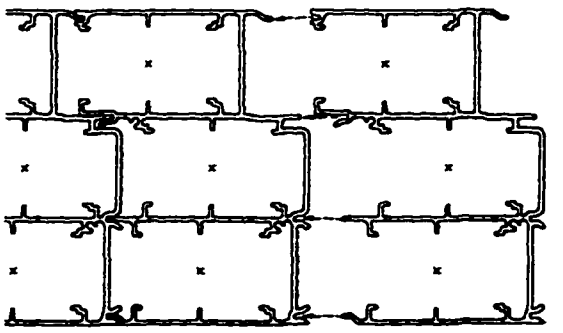

Figure 3.13: Structure of WAMUS chamber cells

The PDT's are formed from aluminum extrusions as shown in Fig 3.12. Each cell is 10 cm across with cathode pads made of copper-clad Glassteel inserted into the top and bottom of each cell and a 50 μm gold-plated tungsten anode wire held at 300 g tension by a special plug mounted in aluminum extrusion end caps. The aluminum extrusion is kept at ground potential while the cathode pads at and the anode wires are held at +2.3 kV and +4.6 kV respectively. Fig 3.13 shows a cross-section of equipotential surfaces in a typical WAMUS cell. The chambers are operated with a gas mixture of Ar(90%)CF_4(5%)$C0_2$(5%) for which the drift velocity is about 6.4 cm/μs .

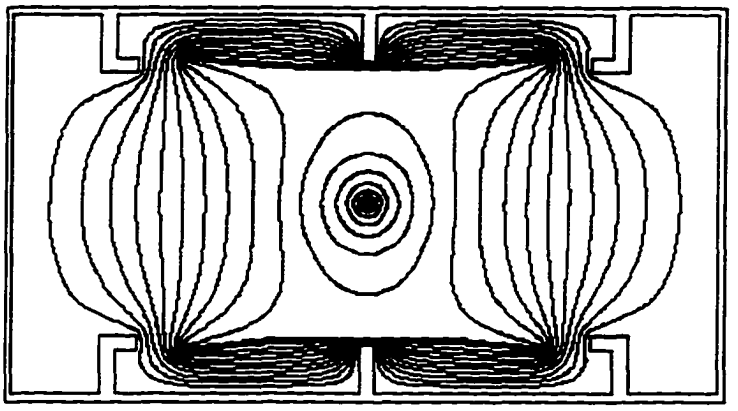

Figure 3.14: A cross-section of equipotential surfaces in a WAMUS cell

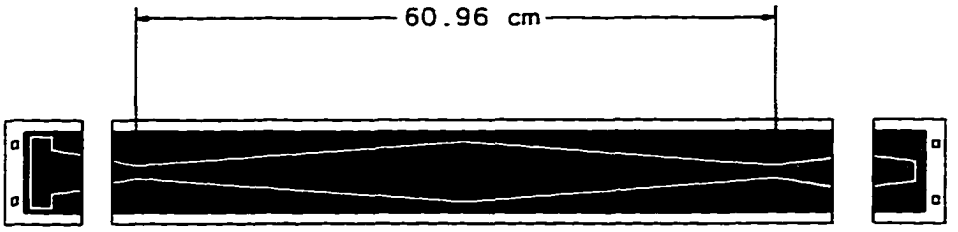

Figure 3.15: The cathode-pad pattern used in WAMUS drift cells

Wires from adjacent cells are jumpered at one end and read out at the other as shown in Fig 3.15. Measuring the difference in the time taken by pulses from a given hit to arrive at the two ends, ΔT, gives the position along the wire, ξ, to within $\pm$ 10-20 cm. Finer ξ resolution is obtained from cathode pad signals. The upper and lower pads consist of two separate electrodes forming the inner and outer parts of a diamond pattern repeated every 61 cm as shown in Fig. 3.14

The inner pads are read independently of the outer ones. The difference between the inner and the outer pad signals to their sum gives the ξ coordinate modulo the half length of a diamond $\approx$ 30 cm. The ΔT measurement indicates the correct diamond and the half of it over which the wire was hit. The ξ resolution achieved in a given chamber $\approx \pm$ 3 mm.

Early in Run 1, the EF region WAMUS chambers were found to be highly inefficient compared to the CF region chambers but it was only towards the end that the cause of this inefficiency was found and corrected. In the high radiation environment, vapours of

Glassteel, used in the construction of cathode pads, settled on the anode wires to form an insulating coat. The affected wires were cleaned by passing a high current to quickly heat it to just below the melting point of gold when the whole coat simply vaporized as described in [38]. The cleaned chambers were found to be as efficient as chambers fitted with new wires. By this time, the accelerator was steadily delivering high luminosities and this necessitated some change in the electronics to handle the high trigger rates (Section 1.10.4).

The SAMUS consists of three stations: designated A, before the toroid and B & C, respectively, after and away from the toroid. Each station consists of three doublets, X, Y and U (at 45° to X,Y). PDT's in each doublet are in a close packed arrangement with adjacent tubes offset by one tube radius for increased detection efficiency. SAMUS PDT's are 3 cm external diameter stainless steel tubes which are electrically grounded. The anode is a 50 μm gold-plated tungsten wire at 208 g tension and maintained at +4.0 kV. The gas used is a $CF_4(90\%)CH_4(10\%)$ mixture with an average drift velocity of 9.7 cm/μs and a maximum drift time of 150 n .

During Run 1b the CF region received an addition of scintillation counters in a phased manner [39]. C-layer PDTs in all octants, except the bottom, are covered with counters made of 0.5 in thick Bicron 404A scintillator.

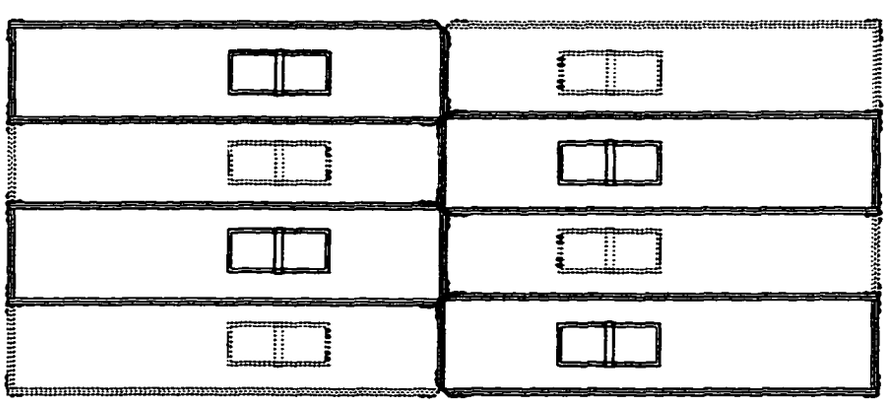

Figure 3.16: Cosmic scintillator module: Counters depicted in solid line are offset in height from the ones shown with dashed lines. The small rectangles represent enclosures for the PMTs.

Eight counters per PDT module spanning two octants are arranged in a nested configuration to reduce geometric inefficiencies as shown in Fig 3.15. Light collection is achieved by wavelength shifting Bicron BCF91A fibres secured in grooves with Bicron 600 optical epoxy so that each fibre covers half the length of a counter. Together the fibres cover half the area of a counter. The fibres are brought back to the centre of the counter in two bundles; one for fibres from each half-length area of the counter. Each bundle is epoxied in an acrylic cookie and read out using an EMI 9902KA photomultiplier tube.

3.9 Muon Electronics

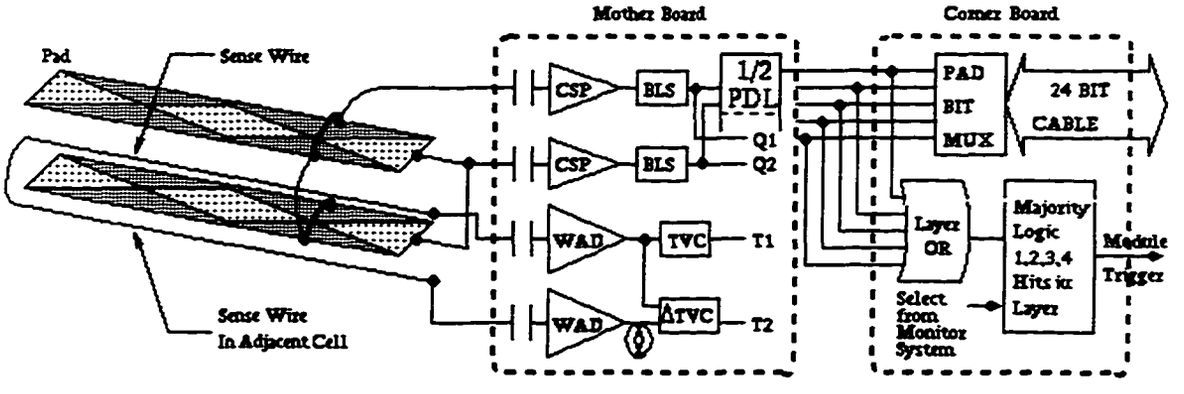

Figure 3.17: Schematic of the muon readout electronics.

Due to the large spread of the muon system, much of the signal processing is done locally. Each chamber carries a 'mother board', MoBo. As shown in Fig. 3.16, for each cell the sum of the upper and lower cathode pads from the inner and outer portion of the diamond pattern is brought to a charge sensitive preamplifier (CSP) which is followed by a baseline subtracter (BLS) circuit that samples signals before and after beam crossing and stores the difference on one of two output capacitors. Signals from the ends of jumpered anode wires are brought to a two-wire amplifier discriminator (WAD) whose output goes to two time-to-voltage converters (TVD) and two ΔT-to-voltage converters (DVD). This circuitry can handle up to two hits on the wire pair. The final stage of the MoBo is a pad-latch circuit that records the PDT cell hit based on the output of the BLS circuit. Each chamber also carries a 'corner board', CoBo. The CoBo multiplexes and

transmits analog signals from the BLSs, TVDs and DVDs to digitizers in the moving counting house (MCH). It transmits pad latch information, multiplexed by four, to the MCH. It OR's latch bits to provide summary information on muon activity. The CoBo also contains the test pulser for front-end electronics calibration.

Signals from the C-layer muon scintillators first go to the scintillation counter trigger board (SciBo) which is located on the muon module. Each board has sixteen inputs, two from each of the eight counters on a chamber, and outputs trigger signals, based on the inputs and AND/OR logic settings, which go to NIM crates on the second floor of the MCH for further processing. It also communicates the latches to the MoBo so that they look like 'hits' in the fourth deck of the muon module. These than go the route of PDT hits, via the CoBo, to the third floor of the MCH for readout. The SciBo also carries a test pulse generator for diagnostics.

3.10 The DØ Trigger System

The DØ trigger system uses several levels of hardware and software filtering of events to keep only those that interesting physics and calibration events. These are described below.

3.10.1 The Level 0 trigger

The Level 0 trigger registers the presence of inelastic collisions based on hits in the level zero counters described above. In addition, this trigger also supplies information on the z-coordinate of the primary collision vertex. This is important since transverse energy corrections require a position resolution of 8 cm at Level 1 and 3 cm at Level 2 . A multiple interaction flag is set in case the level zero time difference is ambiguous. At a luminosity of 5-15 $\times 10^{32}$ $cm^{-2}s^{-1}$the Level 0 trigger rate is about 200 kHz.

3.10.2 Level 1 Framework

This framework gathers digital information from each of the specific Level 1 trigger devices and decides whether an event is to be kept for further processing.

Trigger selection is done with a two-dimensional AND-OR network. Latch bits, numbering 256, bear specific pieces of detector information and form the inputs to the network. Logical AND-OR Combinations of these inputs, asserted, negated or ignored, are made to yield 32 Specific Level 1 triggers. If no vetoes or front-end busy signals exist, triggers satisfying the AND-OR conditions are readied for readout. If a Level 1.5 requirement exists, the Framework forms that decision based on input from Level 1.5 systems. It communicates the results to the DAQ system and provides a summary of all conditions leading to the positive Level 1 decision.

Below, we consider some of the specific Level 1 triggers. All Level 1 and Level 1.5 trigger computations are hardwired.

3.10.3 Level 1 Calorimeter Trigger

This trigger operates on analog trigger signals from BLS circuits, summed into $\delta\eta = \delta\phi = 0.2$ trigger towers out to $|\eta| = 4.0$. For each of the EM and hadronic sections, 1280 separate inputs are provided for each of the calorimeters. The input signal is weighted by the sine of the trigger tower polar angle, interaction assumed at $z = 0$, and digitized by an 8-bit flash ADC and clocked into latches. Combined with z-vertex information from Level 0 memory lookups then provide EM and hadronic transverse energies (E_T) above a fixed cut. These E_T from each trtw are summed and stored in a 9-bit register. The sum is used to lookup $x-$ and $y-$ components of E_T. The full event missing transverse energy $\not\!\!E_T$ is then formed from the x- and y- components of the global E_T. Cuts are performed on the E_T variables, both corrected and uncorrected for vertex effects and the result forms the input to the Level 1 AND-OR network.

This analysis uses the Level 1 $\not\!\!E_T$ trigger as the signature of the neutrino accompanying the decay of the W boson .

3.10.4 Level 1 Muon Trigger

The basic information used here is a single latch bit from each of the 16700 drift cells of the muon system and the scintillators covering the CF region PDTs. This information gives the bend coordinate of the hit drift cells with a granularity of 10 cm in WAMUS and

3 cm in SAMUS. As described above, this information is sent by CoBos up to the MCH where it is received by module address cards (MAC). There is one MAC for each module. These cards perform zero-suppression and determine hit centroids. A centroid is defined as the most likely half cell (5cm in WAMUS and 1.5 cm in SAMUS) through which a track is most likely to traverse when projected to the mid-plane of the module. Centroid finding logic, optimized to account for the z-vertex spread of σ= 30 cm and for delta-ray hits, is programmed into PALS. The change in the muon electronics late in Run 1b, mentioned above, to handle high trigger rates from clean chambers involved optimizing the EF region centroid logic further so that the track segments in each module pointed towards the vertex and not towards the low-beta Quads which deflect charged particles from the beam halo into EF region chambers. Logically OR'ed centroids are sent to coarse centroid trigger (CCT) cards for an Level 1 muon trigger decision. Fine centroid information is sent to octant trigger cards (OTC's) that provide further rejection at Level 1.5 .

Each CCT card can accept inputs from up to 13 MACs. For example, a WAMUS CCT takes 3,5 and 5 inputs from the A, B and C layers respectively. WAMUS CCT cards further OR the centroid pattern by 4 to a hodoscopic pattern 6 cells (60 cm) wide. B and C layer MAC bit patterns are input to two PALS which produce a 12-bit pattern corresponding to all possible 'roads' for A-layer hits. These are compared to the actual A-layer bit pattern to decide the Level 1 trigger. In SAMUS, CCT's first form $x - y - u$ triplets in each of the three stations. Bits from good triplets are used to search for independent 12 cm wide x, y and u roads. Bits from valid roads are then used to find triple coincidences corresponding to good A station space points. For a given eta region, a summing CCT counts muon candidates and presents two bits of multiplicity information to the Trigger Monitor Card (TRGMON). CCT decisions are completed and latched in 3.5 μs and read out by the CCT latch cards in the OTC crates.

Following a positive Level 1 trigger, the full MAC centroid lists are strobed into OTC's for Level 1.5 confirmation. Each OTC accepts inputs from 3 layers of MACS and uses the A, B and C centroids as addresses to a pair of SRAMS whose patterns correspond to tracks above a given p_T threshold (typically 3 to 7 GeV). In the SAMUS,

OTCs are first used to find separate roads in x and y for the three layers and good x-y-u triplets in the B-layer. Centroids from these are sent to a second level of OTCs which link the B-layer centroids from good x and y roads with the B layer centroids of good x-y-u triplets. Processing times are typically 2 μs in WAMUS and 100 μs or more in SAMUS. After each OTC completes processing, the centroids for good triggers and a status word are read out from its output FIFO by the OTC Manager (OTCMGR) card. The OTCMGR filters the centroids through a second p_T threshold. The OTCMGR for each eta region sends three bits to the TRGMON corresponding to p_T , multiplicity and geography. Upon receipt of good Level 1 or Level 1.5 trigger from the framework all trigger words in the OTCMGR are read by the VME Buffer/Driver in each OTC crate.

The TRGMON receives two bits of Level 1 multiplicity and three bits of Level 1.5 information from each eta region which are mapped into 16 Level 1 and Level 1.5 physics bits. These 32 bits are sent to the AND-OR network of the trigger framework.

The muon scintillator trigger is generated as follows. The SciBo requires both PMTs on a counter to fire for a trigger from that board. The trigger signals from all eight scintillation counters are OR'ed and the result sent to two NIM crates in the collision hall. Triggers from all counters in a given octant are then OR'ed to obtain a single signal (SCINT) for each of the six octants with counters. These are sent to logic units in NIM crates in the MCH along with CCT pulses from the PDTs. A coincidence of CCT and SCINT pulses defines the SCINT_CONFIRM trigger term. Absence of SCINT and presence of CCT defines the SCINT_VETO term. The final trigger term used was formed by the presence of SCINT_VETO and absence of SCINT_CONFIRM called SCINT_VETO_CONFIRM_BAR. If there is a valid SCINT-CCT coincidence in one octant, a veto from any other octant is ignored. The trigger decision is conveyed to the Level 1 trigger framework. Since the CCT signal is valid only for a short interval, a gate of 50 n was used for forming the above trigger terms. The scintillator trigger is thus useful in rejecting cosmic ray muons.

Some efforts were made to identify W bosons in SAMUS but isolation of muon tracks from hadronic activity poses a major problem at these large rapidities and the number of high p_T events were relatively small due to large prescales in this region.

There was also no high p_T trigger defined in the Overlap region. Hence this analysis was restricted to triggered muons with $|\eta| < 1.7$.

3.11 The Level 2 Trigger

Level 2 triggering is a Software filtering of events is done on 50 Vaxstations nodes, controlled by the Host Cluster, which reduces the 200 Hz output rate out of Level 1 to 2 Hz. For a detailed discussion of the Level 2 and DAQ systems please see reference 1 in the bibliography.

Level 2 does a partial reconstruction of events based on FORTRAN routines called tools. Some tools identify objects, such as jets or muons, or event characteristics such as EM clusters or $\not\!\!E_T$. Others recognize noise or background conditions. Sets of tools are logically combined into with one of the 32 Level 1 trigger bits to form filter scripts. There can be as many as 128 Level 2 scripts and events passing these are written out to 8 mm tapes for off-line reconstruction and analysis.

CHAPTER 4

DATA SELECTION

4.1 Introduction

This Chapter describes the determination of luminosity, data reconstruction, the real time or online triggers used to select data and finally the off-line criteria used to select data for the W charge asymmetry analysis.

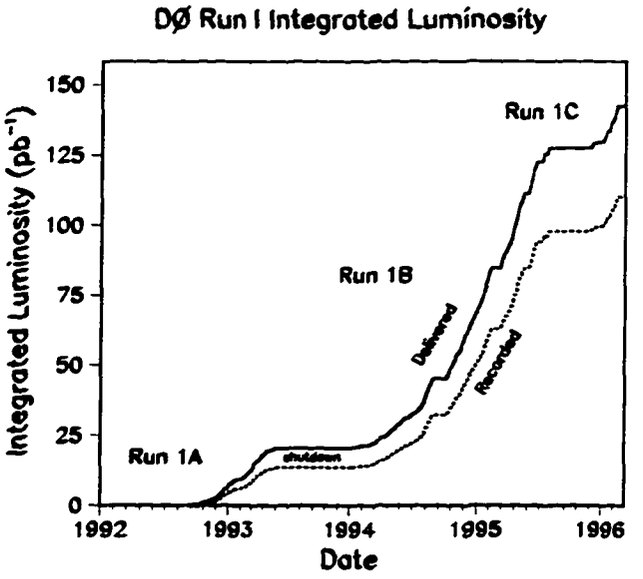

Figure 4.1: The DØ integrated luminosity as a function of time.

Run 1 of the Tevatron extended from late 1992 to 1996. The running period was broken into three distinct periods separated by shutdowns for maintenance and/or upgrade of both the accelerator and the detectors. These are called Run 1A(1992-1993), Run 1B(1994-1995) and Run 1C(1996). Figure 1 shows the integrated luminosity as a

function of time. The plateaus indicate the shutdowns. This analysis only uses data from the periods labeled 1A and 1B since part of Run 1C was run at 630 GeV to study jet and b-quark cross. Results at this energy could be compared with that of the UA2 experiment. The remaining part of Run 1C was too brief to add significantly to the $W \rightarrow \mu\nu$ data sample. In this period, triggers were dedicated to understanding the energy scale of the calorimeter and systematic errors and backgrounds to various analyses in progress.

4.2 Luminosity Measurement

As mentioned in Chapter 3, the beam luminosity at the DØ detector is monitored using the Level Zero (L0) detector. The instantaneous luminosity $\mathcal{L}$ is related to the counting rate in the L0 counters by

$$\mathcal{L} = \frac{R_{L0}}{\sigma_{L0}} \tag{4.1}$$

where σ_{L0}, called the luminosity monitor constant [34], is the cross section subtended at the L0 counters. The counting rate (and, thus the luminosity $\mathcal{L}$) is measured for each of the six bunch crossings.

If there are multiple interactions per crossing then the counting rate is less than the interaction rate. The average number of interactions per crossing, $\bar{n}$, is based on Poisson statistics, and given by

$$\bar{n} = \mathcal{L}\tau\sigma_{L0} \tag{4.2}$$

where τ, the beam crossing interval, is approximately 3.5 μs . The multiple interaction correction factor is then [34]

$$\frac{\mathcal{L}}{\mathcal{L}_{meas}} = \frac{\bar{n}}{1 - e^{-\bar{n}}} = \frac{-\ln[1 - \mathcal{L}_{meas}\tau\sigma_{L0}]}{\mathcal{L}_{meas}\tau\sigma_{L0}} \tag{4.3}$$

The numerical value for σ_{L0} is given by [35]

$$\sigma_{L0} = \epsilon_{L0}[A_{SD}\sigma SD + A_{DD}\sigma DD + A_{SD}\sigma DD].$$

Here ϵ_{L0} is the L0 trigger efficiency which was determined by using data samples triggered solely on the crossing time of the $p\bar{p}$ beams at the DØ collision region and not on

the presence of an interaction. The terms in the square bracket together represent the total inelastic cross section seen by the L0 detector. The subscripts SD, DD and HC stand for single diffractive, double diffractive and hard core scatterings, respectively, and the symbols A and σ denote the L0 acceptances for these processes and their cross sections. The acceptances were obtained by using Monte Carlo simulations of these processes followed by full detector simulation and off-line reconstruction. For the cross sections the world-average based on the measurements of the CDF detector [40][41][42] and the E710 [43] experiment at Fermilab is used. Thus [35],

$$\sigma_{L0} = 46.7 \pm 2.5 \text{ mb}$$

Events, such as $W \rightarrow \mu\nu$ are selected by online computers based on specific triggers described in the next section and the integrated luminosity, $\int Ldt$, for each such trigger is recorded into a database for later use.

4.3 The $W \rightarrow \mu\nu$ trigger

The hardware description of the trigger was given in the the last chapter. Here, the selection of muons coming from W decays is described. The main characteristics of these muons are that they are isolated, i.e. the muon tracks do not occur in or near jets, they have large transverse momenta and they are accompanied by an equal amount of 'missing' transverse momentum from the neutrino that accompanies the decay.

Recall, from chapter 3, that a combination of Level 1 requirements is called a specific trigger and that 32 of these were permitted each composed of combinations of the AND_OR terms. Each specific trigger can have several level 2 filters. The list of specific triggers with various filters attached to them is called a triggerlist [44] which is loaded into the host computer for data-taking before each run.

The Level 1 specific trigger employed for collecting data used in this analysis varied. It was called MU_1_HIGH with pseudorapidity coverage out to 1.7 through Run 1A and until run number 89000 of Run 1B. It was at this point in time that the EF WAMUS chambers were cleaned and were expected to be more efficient. To keep the event rate manageable,

L2 Executable	Trigger Menu	Run Range	Effective Date
4.3	7.1	60639-60832	Feb 07, 1993
4.4- 4.7	7.1	60833-62157	??? ??, 1993
4.8- 4.9	7.2	62158-64085	Mar 10, 1993
4.9-4.13	7.3	64086-65879	Apr 21, 1993

Table 4.1: Trigger list major version numbers and Level 2 executable version numbers for Run 1a post-shutdown data used in this analysis.

L2 Executable	Trigger Menu	Run Range	Effective Date
6.03	8.1	73643-73724	Jan 18, 1994
	8.2	73725-74192	Jan 19, 1994
	8.3	74193-74499	Jan 29, 1994
6.05	8.3	74500-75038	?
	8.4	75039-75142	Feb 22, 1994
	8.5	75143-75178	Feb 24, 1994
6.06	8.5	75179-75176	Feb 24, 1994
	8.6	75177-76304	Mar 20, 1994
6.07	8.6	76411-77824	Mar 26, 1994
	8.7	77825-78431	Apr 24, 1994
6.08	8.7	78432-78943	May 10, 1994
6.09	8.7	78944-79478	May 19, 1994
6.10	8.7	79479-79982	May 29, 1994
	9.0	79983-80979	Jun 09, 1994

Table 4.2: Trigger list major version numbers and Level 2 executable version numbers for the Run 1b data used in this analysis. Continued on next page ...

L2 Executable	Trigger Menu	Run Range	Effective Date
6.11	9.0	80980-81906	Jun 30, 1994
	9.1	81907-82596	Jul 21, 1994
6.12	9.1	82597-83212	Aug 11, 1994
	9.2	83212-84303	Aug 23, 1994
7.03	9.2	84304-84720	Oct 04, 1994
7.04	9.2	84721-85203	Oct 17, 1994
7.05	9.2	85204-85276	Oct 28, 1994
	10.0	85277-85401	Oct 31, 1994
7.06	10.0	85402-86278	Nov 04, 1994
	10.1	86279-86467	Nov 28, 1994
7.07	10.1	86468-87115	Dec 01, 1994
7.18	10.1	87116-87803	Dec 19, 1994
	10.2	87804-89246	Jan 09, 1995
7.11	10.2	89247-89328	Mar 07, 1995
7.12	10.2	89329-89517	Mar 09, 1995
	10.3	89518-89891	Mar 14, 1995
	10.4	89892-90794	Mar 26, 1995
7.13	10.4	90795-91675	Apr 25, 1995
7.14	10.4	91676-91922	May 26, 1995
	10.5	91923-92827	Jun 03, 1995
7.15	10.6	92828-?????	Jul 12, 1995

Table 5.2: (Continued from last page) Trigger list major version numbers and Level 2 executable version numbers for the Run 1b data used in this analysis.

a new specific trigger called MU_1_CENT was defined for $|\eta| < 1.0$ and MU_1_HIGH was used for $1 < |\eta| < 1.7$ only at a high prescale.

Run No	L1 Specific Trigger	
	CF	EF
< 89000	MU_1_HIGH	
> 89000	MU_1_CENT	MU_1_HIGH

Table 4.3: Level 1 (L1) specific trigger names.

The Level 1 trigger requires at least one muon track in the WAMUS region to pass the CCT logic. Starting from run 81907 during Run 1B, scintillator veto was used. Muon tracks passing the Level 1 trigger were then required to satisfy the high p_T OTC logic at Level 1.5. This effectively imposed a transverse momentum requirement of 7 GeV/c on the muon track.

In addition there were terms that ensured that beam conditions were good. One source of concern is the main ring. Recall that the Main Ring accelerates protons even as beams are colliding in the Tevatron. The main ring passes through the coarse hadronic section of calorimeter. Losses from the main ring during injection or extraction of bunches show up in the detector. In particular, the high voltage supplies to the muon chambers just above the main ring tend to sag temporarily. Data collection is avoided during these episodes by using a term called MRBS_LOSS. This term based on accelerator clock signals effectively vetos data-taking during injection and extraction of Main Ring bunches. Losses can also occur when a Main Ring bunch passes through the detector. The term MICRO_BLANK is used to veto out a $p\bar{p}$ event if a Main Ring bunch is present in the detector within 800 ns of a $p\bar{p}$ bunch crossing. The Level 1 trigger also carries a prescale term. Of all events only one out of the value assigned to this scale term is considered by the trigger. This is used to keep the bandwidth in check.

The level 2 filters also varied. The filter used for runs prior to 89000 was called MU_1_MAX and covered the entire WAMUS region. For runs later than 89000 the filter

MU_1_CENT_MAX was used for the CF region under MU_1_CENT and MU_1_MAX was used for the EF region under MU_1_HIGH with a higher level 2 prescale. The prescales were set to get the maximum possible integrated luminosity within the bandwidth allocation.

Run No	L2 Filter	
	CF	EF
< 89000	MU_1_MAX	
> 89000	MU_1_CENT_MAX	MU_1_MAX

Table 4.4: Level 2 (L2) filter names.

The level 2 trigger is a software filter. Raw hits undergo partial reconstruction into physics quantities which can be used to select events of interest. The level 2 requirement on muons from W bosons were (i) that there be at least one muon with transverse momentum, $p_T^{\mu} \geq$ 15 GeV/c , (ii) that the flag word IFW4 (explained in the next section) has a value of zero and consequently the track is of the best quality, (iii) that the muon is confirmed by a corresponding trace of energy in the calorimeter and (iv) that it survives scintillator veto and MUCTAG cuts (discussed below) to remove cosmic ray muons.

Trigger	Efficiency, CF		Efficiency, EF	
	Pre-cleaning	Post-cleaning	Pre-cleaning	Post-cleaning
Level 1	0.785 ± 0.007	0.765 ± 0.011	0.171 ± 0.022	0.588 ± 0.032
Scintillator	0.983 ± 0.017	0.970 ± 0.030	N/A	N/A
Level 1.5	0.697 ± 0.008	0.686 ± 0.013	0.820 ± 0.054	0.759 ± 0.037
Level 2	0.863 ± 0.013	0.872 ± 0.019	0.724 ± 0.100	0.857 ± 0.076

Table 4.5: Run 1B trigger efficiencies for high p_T CF and EF region muons before and after "cleaning" (run 89000).

Although not used in this analysis, Table 4.3 shows the efficiencies of the different levels of trigger used in Run 1B [20]. Level 1.5 refers to triggering based on the octant trigger card (see Chapter 3). In particular, note the improvement in Level 1 efficiency by a factor of more than 5. The trigger efficiencies are determined using muons that pass the complete set of cuts in Table 4.3 but triggered by a non-muon trigger irrespective of whether they also fired a muon trigger.

The total integrated luminosities used in this analysis, obtained from the production database using the Level 2 filter name as the key, for the two Run 1 periods is as follows:

Period	Luminosity pb^{-1}	
Run 1A	6.5 ± 0.4	
Run 1B	CF	EF
	55.4 ± 3.0	38.0 ± 2.1

Table 4.6: Integrated luminosities for Run 1A and Run 1B.

Only late in Run 1A was it realized that reversing magnet polarities was essential for reducing certain systematic uncertainties which will be explained in a later chapter. Hence the integrated luminosity in this analysis is less than that used in the cross section analysis at DØ.

4.4 Off-line Reconstruction

The level 2 trigger (Section 4.11) does only a partial reconstruction for lack of time. The output from level 2, stored on 8 mm tapes, is called raw data that consists of digital information such as pulse heights and drift times from various detector components. This information must be reconstructed into physics objects such as electrons, muons, photons or jets. Track and kinematic variables associated with them must also be extracted for meaningful physics analyses. This is accomplished by a computer program called DØ RECO [27]. The output of DØ RECO is written out in various data streams. The ALL

stream consists of all the events processed. This analysis uses data output to the WZM stream. The selection criteria for the WZM stream are rather loose. At least one muon with the following requirements had to be found for the WZM filter to pass an event. Section 4.5 describes each of the quantities used in these cuts in detail.

1. Pseudorapidity, $|\eta_\mu| < 2.4$
2. Transverse momentum, $p_T^\mu \geq$ 15 GeV/c
3. Track quality flag-word, IFW4 ≤ 1
4. Pass cosmic rejection with MUCTAG (see Below)
5. Bend view impact parameter, $b_{\text{bend}} \leq 25$ cm
6. Calorimeter confirmation, $E_{\text{cal}}^{\text{1nn}} \geq 0.5$ [1.0] for the CF region [EF region]

regions, respectively

7. Floating time, $t_0^f \leq 600$ ns
8. HFRACT ≥ 0.6 (Run 1B only)

The WZM data from Run 1A were stored on disk in DST format (Data Summary Tape) which contains only reconstructed information. During Run 1B, a smaller data format called μDST (Micro DST) containing only the most relevant reconstructed information was used. The version of the reconstruction program used to stream Run 1A data was 11.19. These events were later rerun through version 12.15 to obtain the newly defined global fit definition.

The EF region events for Run 1B were selected in the following manner. Events were selected from the HLP stream, of which the WZM stream is a sub-stream, requiring

$$p_T^\mu \geq 15 \text{ GeV/c} \text{ , HFRACT} \geq 0.6 \text{ and IFW4} \leq 1.$$

Roughly 15000 events resulted. These events were picked from tape [1] and processed through a program called DØ FIX. This was necessitated since the global fit was not performed correctly for the EF region during regular streaming.

Below, those aspects of the reconstruction program relevant to this analysis are described. In particular, since the analysis is restricted to $|\eta_\mu| < 1.7$, muon reconstruction is described only for the WAMUS detector.

[1] Thanks to Norman Graf for this effort.

4.4.1 The Event Vertex

The interaction vertex needs to be known to good precision for good track fitting and transverse momentum determination. It is found using the central detectors. The vertex chamber is used to obtain the $r - \phi$ position of the vertex. Since it is approximately stable during each run, the average $r - \phi$ position is used for every event of a given run [45]. The z coordinate of the vertex, called z-vertex, is determined using the central or the forward drift chambers by extrapolating reconstructed tracks. A Gaussian fit is performed on each cluster of tracks associated with a vertex yielding the z-vertex with a position resolution of 0.65-0.95 cm depending on the number of tracks associated with each vertex. The vertex with the largest number of tracks associated with it is called the primary vertex. Two vertices can be resolved if they are separated by more than 7 cm.

4.4.2 Muon Track Reconstruction

Raw data consists, for each PDT, of a pad-latch bit indicating a possible hit and analog signals representing drift tine, delta time and cathode pad charges associated with the pad-latch. Muon reconstruction processes this data in three steps: (i) hit sorting, (ii) track finding, and (iii) a global fit. The first two steps use information from the muon system and the last part makes use of information from other subsystems. [46]. The first two stages are equivalent to the processing done by the Level 2 trigger software.

The **Hit sorting** part of the muon reconstruction program converts the raw data from muon chambers into three dimensional space points in the global DØ coordinate system as follows. It goes over the list of chambers with hits and corrects the drift time and delta time constants with calibration constants. It uses the pad latch bits and time information to assign the hit to an even or an odd cell and flags inconsistent data. The address of each hit is then converted to the global coordinate system using detector geometry values. It corrects the pad values for pedestals and gains and determines the two vernier pad solutions. It converts the time division to a distance from the wire centre, estimates time of flight corrections. It then converts the corrected drift time to a drift distance.

Track-finding is a pattern recognition algorithm that determines whether or not a set

of sorted hits is consistent with the passage of a single charged particle through the muon system. Track-finding starts from the list of hits and looks for a BC segment with at least four points. If this is found, a search is made for a matching A layer segment with at least two hits. If no BC segment is found, the search starts by searching for an A segment with three points, of which one may be the vertex, and then extends it into the outer layers. All segments are required to point to the vertex within 3-5 m. Each segment found in this manner is stored as a possible candidate and the best one is selected from the number of hits and the quality of fit. The search is done three times or until six tracks are found per quadrant. The first pass looks for only three layer (ABC) tracks, the second allows two layer tracks and the third expands the road search window by 50%.

If a track is found, a fit is performed in both the bend view (the $r - z$ plane perpendicular to the wires) and the non-bend view (the $x - y$ plane parallel to the wires). In the non-bend view, a straight line is fit through the magnet and the track is constrained to pass through the vertex. In the bend-view, the fit depends on whether the tracks are two or three layer tracks. For an ABC track, a line is fit to the BC points and extrapolated to the centre of the magnet. The resulting point is combined with the A layer hits to fit the segment inside the magnet. Here the vertex point is used in the fit only if there are less than three hits in the A layer. BC tracks are fit by projecting the BC segment to the centre of the magnet and using this point and the vertex to form the segment inside the magnet. The internal segments for AB or AC tracks are fit using the vertex and the A layer hits to project to the center of the magnet. This point is then used in the fit with B or C layer hits for the external segment.

The bend in the track gives a first estimate of the momentum. A preliminary track quality flag is set using the projection of the track to the vertex and the quality of fit in each view.

The **global fit** [20][47] provides the final determination of muon momentum and position based on information from the muon system, the vertex chamber, the central and forward drift chambers and the calorimeter. It combines these inputs using a least squares fit. The input parameters number sixteen: two vertex positions from the vertex chamber and the drift chambers, four tracking measurements from the drift chambers, two an-

gles representing the multiple scattering of the muon in the calorimeter, four tracking measurements from the muon A layer and four tracking measurements from the muon BC layers. These are fit with seven parameters: four describe the position of the muon track, in both the bend and non-bend views, before the calorimeter as provided by the drift chambers. Two describe the bending of the muon track due to multiple scattering in the calorimeter as predicted by Monte Carlo combined with detector simulation. The seventh parameter is the inverse of the track momentum, $1/p$.

The resolution for low momentum muons is dominated by multiple Coulomb scattering in the toroids and that for high momentum muons by the resolution of space point measurements ($\approx$ 2mm). Chamber inefficiencies and misalignment ($\approx$ 1mm) also contribute to muon momentum uncertainties.

4.5 $W \rightarrow \mu\nu$ Event Selection

Some requirements are imposed both at the time of data acquisition to keep a large percentage of good muon track candidates in the data. Additional off-line selection or "cuts" are needed to extract muons originating from from W boson decays. Backgrounds include other physics processes, fake tracks from accidental hits or noise and cosmic ray muons.

A summary of all the cuts used to identify $W \rightarrow \mu\nu$ events is listed in Table 4.5. Each of these cuts is discussed in detail below .

4.5.1 Pseudorapidity Range

This analysis uses muons detected by the pure WAMUS spectrometer in the pseudorapidity range

$$|\eta_\mu| < 1.6$$

The region $2.5 < |\eta| \leq 3.4$ is covered by the SAMUS spectrometer was excluded because it is extremely difficult to identify isolated muon tracks in this region. The region $1.7 < |\eta| \leq 2.5$ is partly covered by WAMUS PDT's and partly by SAMUS tubes and is called the Overlap region. This region was excluded because muon reconstruction in

Cuts	CF	EF
Muon Pseudorapidity	$\|\eta\| < 1.7$	
Fiducial Cut	$\int B.dl \geq 0.6$ GeV/c	
Muon Quality Flag (IFW4)	IFW4 $\leq$ 1	
Muon Layers Hit	2 or 3	3 (7 points on track, 1B)
Impact Parameter (bend view)	$b_{\text{bend}} \leq 15$ cm	$b_{\text{bend}} \leq 20$ cm
Impact Parameter (non-bend view)	$b_{\text{non-bend}} \leq 20$ cm	$b_{\text{non-bend}} \leq 25$ cm
Muon-CD track match	$\Delta\phi \leq 0.04$ radians and $\Delta\theta \leq 0.12$ radians	
Global Fit	$0 \leq \chi^2 \leq 100$ (1A) and $0 \leq \chi^2 \leq 20$ (1B)	
MUCTAG (cosmic rejection)	No opp. hits	No opp. hits or tracks
Calorimeter confirmation	$E_{\text{cal}}^{\text{1nn}} \geq 1.0$ GeV	$E_{\text{cal}}^{\text{1nn}} \geq 1.5$ GeV
HFRACT (MTC)	HFRACT ≥ 0.6	HFRACT ≥ 0.75
EFRACTH1 (MTC)	EFRACTH1> 0.0 if HFRACT < 1.0	
Scintillator Veto	Yes (1A only)	No
Floating time shift	$\Delta t_0^f \leq$ 100 ns	
2nn Isolation	$I_\mu^{2nn} \leq 3$	
Halo Energy	$E_{\text{cal}}(0.6) - E_{\text{cal}}(0.2) \leq 6$ GeV	
Kiematic cuts	$p_T^\mu \geq 20$ GeV/c and $\not\!\!E_T \geq 20$ GeV	

Table 4.7: $W \rightarrow \mu\nu$ selection cuts at a glance. The labels 1A and 1B indicate cuts specific to Run 1A and Run 1B. In Table 4.2, related cuts have grouped in rows seperated by double lines. The first group of cuts define the geometric regions of the detector used in this analysis. The second (track-quality), third (confirmation in the calorimeter) and fourth (timing) groups of cuts select good quality beam-produced muons and reduce cosmic ray contamination. The fifth (isolated tracks) and sixth (kinematic cuts) enhance the $W \rightarrow \mu\nu$ signal.

this region is very complicated due to the mixed types of detectors and varied orientations.

4.5.2 Fiducial Cut

To enforce proper momentum measurement especially for muon tracks in the region near the CF-EF boundary, $0.7 < |\eta| < 1.0$, where the thickness of magnetized iron traversed through can be small, a minimum value is imposed on the integral of the magnetic field along the muon track,

$$\int B.dl \geq 0.6 \text{ GeV/c}$$

4.5.3 Impact Parameter

The "impact parameter" of the muon track obtained using only the muon system is restricted to the following values in the bend view (b_{bend}) and non-bend views ($b_{\text{non-bend}}$).

Impact parameters in the CF: $b_{\text{bend}} \leq 15$ cm, $b_{\text{non-bend}} \leq 20$ cm

Impact parameters in the EF: $b_{\text{bend}} \leq 20$ cm, $b_{\text{non-bend}} \leq 25$ cm

This ensures that the muon tracks originate from the beam and cuts out cosmic ray muons and spurious tracks from combinatorics.

4.5.4 Muon Quality Flag-word (IFW4)

A flag-word (IFW4) indicating muon track quality is incremented by one, during reconstruction, for every failure of a muon track when tested against the following criteria:

1. No missing muon chamber layers.
2. The non-bend view impact parameter, $b_{\text{non-bend}} \leq 100$ cm.
3. The bend view impact parameter, b_{bend} 80 cm.
4. The non-bend view fit has an RMS residual ≤ 7 cm.
5. The bend view fit has an RMS residual ≤ 1 cm.

A muon with an IFW4 value of zero has the best track quality. This analysis uses a cut of IFW4 ≤ 1.

4.5.5 Three Layer Tracks

To reduce the number of fake tracks due to combinatorics in the EF region, all tracks must have hits in all three layers of the muon system. The total number of hits is required to be at least seven which must be distributed as three, two and two among the A, B and C layers, respectively. Two or three layer tracks are allowed in the CF region.

4.5.6 Global Fit

The global fit has been described above. All muons used in this analysis are required to have a successful global fit and the least squares fit, χ^2 , is required to have the following values for the two run periods.

For the CF region: $0 \leq \chi^2 \leq 20$

For the EF region: $0 \leq \chi^2 \leq 10$

A value of -1 for the global fit χ^2 corresponds to muon tracks that do not have a matching central detector and these are excluded. The tighter χ^2 requirement for the EF region reduces the dominant background due to accidental hits in this region.

4.5.7 Calorimeter Confirmation

A muon track passing through the calorimeter will deposit energy similar to that from a minimum ionizing particle. The calorimeter confirmation tool CAL_CONFIRM, used in the in the Level 2 trigger, ensures that a total energy greater 5 GeV is deposited in calorimeter cells along the muon track without shower development or hadronic activity. Calorimeter confirmation ensures that the muon track has continuity through the calorimeter towards the interaction region and is thus useful in reducing the cosmic ray muon background.

Off-line, two other criteria related to energy deposited in the calorimeter were employed. These use results of the Muon Tracking in Calorimeter (MTC) package. This software provides a number of tools to track muons in the calorimeter [48]. Two of these are used, off-line, in this analysis.

The variable HFRACT is the fraction of hadronic calorimeter layers used in the track fit by MTC out of the maximum possible number. Ideal tracks would have HFRACT=1.0.

In this analysis, this requirement has been relaxed to the following values to gain efficiency.

For the CF region: HFRACT ≥ 0.60

For the EF region: HFRACT ≥ 0.75

The variable EFRACTH1 is fraction of the total 3x3 calorimeter tower energy in the last hadronic layer. A 3x3 tower is the projection of a nine by nine array of cells centred around the η and ϕ of the candidate muon track. If HFRACT is less than 1.0, EFRACTH1 is required to be nonzero, i.e., some energy must be present in the last hadronic layer. Studies have shown that the combination of HFRACT and EFRACTH1 has a larger signal to background ratio than the HFRACT by itself [49]. Thus, it is required that

If HFRACT < 1, EFRACTH1 > 0.

4.5.8 Central Detector Track Match

It is required that a CD track is located within a cone around the muon such that

$\Delta\phi(\text{muontrack, CDtrack}) \leq 0.04$ radians

$\Delta\theta(\text{muontrack, CDtrack}) \leq 0.12$ radians

Such a match is not expected for fake tracks constructed out of accidental hits or noise. This cut reduces the background from such tracks.

4.5.9 Floating Time

The floating time is an estimate, obtained from PDT drift times, of the time offset of the muon from beam crossing extrapolated back to the interaction point. For each value of a time offset that is tested, the drift times for each point on the track is offset by same time increment and new drift distances are computed. These distances are used to do a bend-view (drift-view) track fit and the χ^2 of the fit determined. The best value of the time offset is selected by first requiring the most number of points to be used in the fit, and then requiring the best track-fit χ^2 . The floating time distribution of real beam muons should peak at zero. Due to the fact that time runs backward in the digitization circuits

(TDC's), the sign of the floating time is reversed from what is expected: positive floating times correspond to early particles and negative to late particles.

Figure 4.2a shows the floating time distributions for beam produced muons obtained with very tight requirements on calorimeter confirm and impact parameter besides the usual quality cuts. Fig. 4.2b shows muons with large impact parameter and poor calorimeter confirmation such as cosmic ray muons or tracks reconstructed out of accidental or noise hits. The selection criteria for these signal and background distributions are described in Section 6.2. This analysis requires

$$t_0^f \leq 100 \text{ ns}.$$

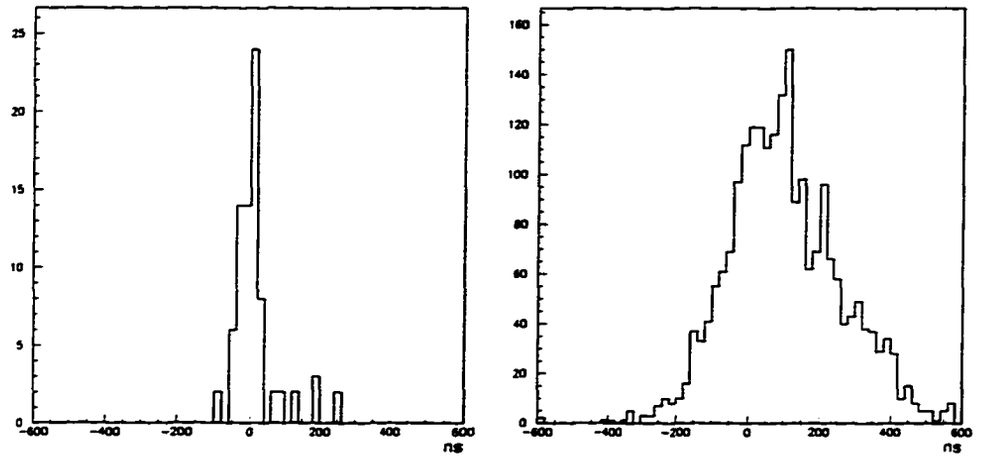

(a) Signal (b) Background

Figure 4.2: The floating time distribution for signal and background events.

4.5.10 MUCTAG

This software tool is used to remove cosmic muons. It sets separate bits in a flag word, IFW2, if muon modules opposite (in ϕ) each other are hit or if there are reconstructed tracks opposite to each other. In the CF region, where the geometric acceptance for cosmic ray muons is high, those candidates with opposite hits are removed and in the EF region, those candidates with opposite tracks are removed.

4.5.11 Scintillator Veto

The scintillator veto term was added to the Level 1 trigger beginning at run number 81907. The manner in which this AND_OR term is generated is described in Section 3.9.4. While the time-of-flight as measured by scintillator would be a powerful parameter to reduce cosmic ray muons, there were problems with the reconstruction code that extracts this information from the raw data. Hence it has not been used in this analysis.

4.5.12 Isolation

Muons originating from W decays are isolated. Two isolation variables have been used.

The variable I_{μ}^{2nn} is given by

$$I_{\mu}^{2nn} = \frac{E_{cal}^{2nn} - E_{cal,Expected}^{2nn}}{\sigma_{Expected}}$$

where E_{cal}^{2nn} is the sum of the calorimeter energy in cells hit by the muon and the two nearest neighbour cells, $E_{cal,Expected}^{2nn}$ is the expected contribution from the muon ionization and $\sigma_{Expected}$ is expected error. The expected quantities are found using tables generated by detector simulations. The cut used to select isolated muons is

$$I_{\mu}^{2nn} \leq 3.$$

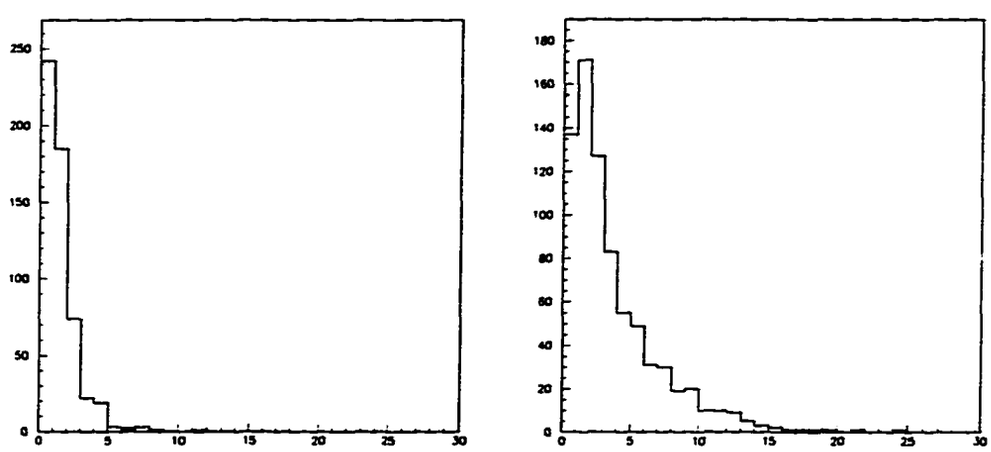

(a) Signal (b) Background

Figure 4.3: The I_{μ}^{2nn} distribution for signal and background events.

Figure 4.3a shows the distribution of I_{μ}^{2nn} variable for signal events that pass all the selection criteria enumerated here and the additional requirement that there are no jets in the opposite hemisphere in ϕ with respect to the muon.

Another parameter used is the muon halo energy defined as the difference in the energy deposited in two coaxial $\eta - \phi$ cones of 0.6 and 0.2 around the muon in the calorimeter. The cut used was

$$E_{\rm cal}(0.6) - E_{\rm cal}(0.2) \leq 6\,{\rm GeV}$$

Figure 4.3b shows the I_{μ}^{2nn} distribution for background distribution for muons with all but the isolation requirements and with $5 < p_T^{\mu} < 15$ GeV/c .

Figures 4.4a and 4.4b show the halo energy distribution for signal and background samples chosen exactly as for the I_{μ}^{2nn} distributions in Figures 4.3a and 4.3b.

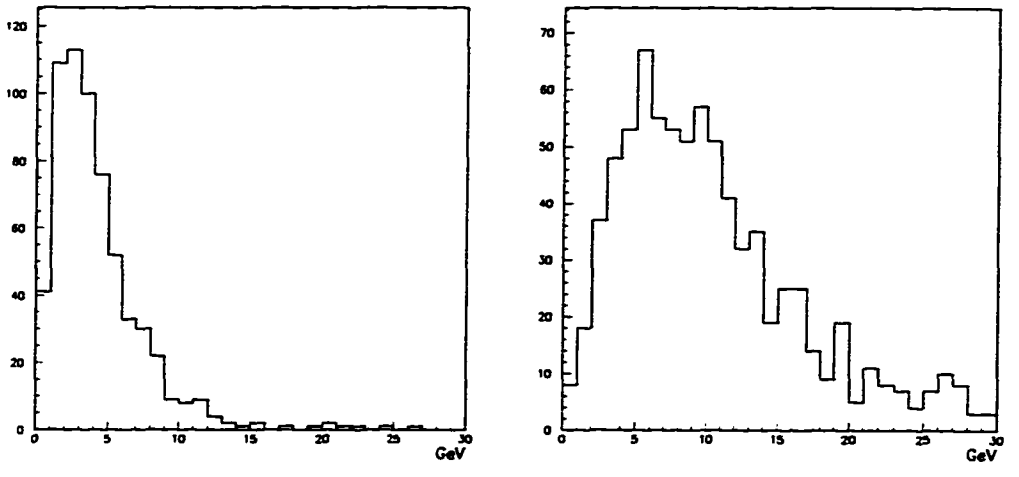

(a) Signal (b) Background

Figure 4.4: The Halo energy distribution for signal and background events.

4.5.13 Kinematic cuts

The transverse momentum cut is imposed.

$$p_T^{\mu} \geq 20\ {\rm GeV/c}$$

A similar cut is placed on neutrinos accompanying them.

Since a neutrino interacts very weakly with matter, we can infer its transverse momentum by the fact that the total transverse momentum in a W decay must be conserved and equal to zero. The missing transverse energy in the calorimeter is defined by

$$\not\!\!E_T^{\rm cal} = \sqrt{(\not\!\!E_{Tx}^{\rm cal})^2 + (\not\!\!E_{Ty}^{\rm cal})^2}$$

where,

$$\not\!\!E_{Tx}^{\rm cal} = -\sum iE_i \sin(\theta_i) \cos(\phi_i),$$

and

$$\not\!\!E_{Ty}^{\rm cal} = -\sum iE_i \sin(\theta_i) \sin(\phi_i).$$

Here the sum is over all the cells in the calorimeter with signal amplitude 2σ above mean channel noise and E_i, θ_i and ϕ_i are the deposited energy, polar and azimuthal angles respectively.

For events with muon neutrinos, which are of interest here, this must be corrected with the muon transverse momentum as

$$\not\!\!E_{Tx} = \not\!\!E_{Tx}^{\rm cal} - p_{Tx}$$

$$\not\!\!E_{Ty} = \not\!\!E_{Ty}^{\rm cal} - p_{Ty}$$

We require that

$$\not\!\!E_T^{\mu} \geq 20 \text{ GeV/c}.$$

The missing transverse energy resolution is affected by many factors, such as energy fluctuation in the calorimeters, energy lost in and around the beam pipe and cracks in the central calorimeter, signal fluctuations caused by radioactive noise from uranium, electronic noise etc. A global quantity called the scalar transverse energy, defined by

$$\widetilde{\not\!\!E_T} = \sum E_i \sin(\theta_i)$$

is used to parameterize the resolution as

$$\sigma_{\not\!\!E} = a + b \cdot \tilde{\not\!\!E}_T$$

with a =1.08 GeV and b =0.019 GeV for minimum bias data.

4.5.14 Selection Efficiency

This analysis does not need to take efficiencies into account since the the charge asymmetry is a ratio. The total efficiency for Run 1B for the cuts used [20], determined using the $Z^o \rightarrow \mu\mu$ sample, is given below.

CF	EF
0.645 ± 0.023	0.233 ± 0.044

Table 4.8: Run 1B selection efficiencies for high p_T muons in the CF and EF regions.

4.6 Final Sample

The following Table lists the number of events that survive these cuts in the CF and EF regions for the two running periods.

Period	CF	EF
Run 1A	1088	76
Run 1B	7743	588

Table 4.9: Number of W candidates for Run 1A and Run 1B.

The selection criteria used here are the same as those used in the $W \rightarrow \mu\nu$ cross section analysis. It has been verified that the number of muons obtained with the above cuts yield the correct cross section in the CF region for Run 1A [50] and Run 1b [20]. The efficiencies for the various cuts made here are not completely understood in the EF, but a rough estimate of the cross section in this region, with the above cuts, yields the W cross section within errors[51]. Figures 4.5 and 4.6 show the transverse momentum of the muons and the transverse mass of the W boson , respectively, for the CF region and 4.7 and 4.8 show these distributions for the EF region. These are consistent with the distributions expected from $W \rightarrow \mu\nu$ decay given the resolution of the muon system.

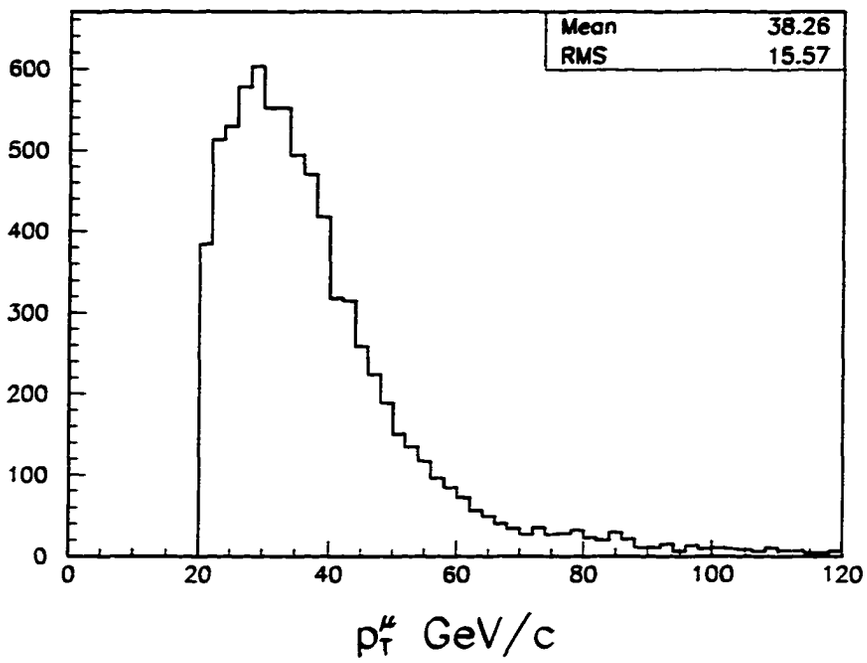

Figure 4.5: Transverse momenta of muons from Run 1B for the CF region.

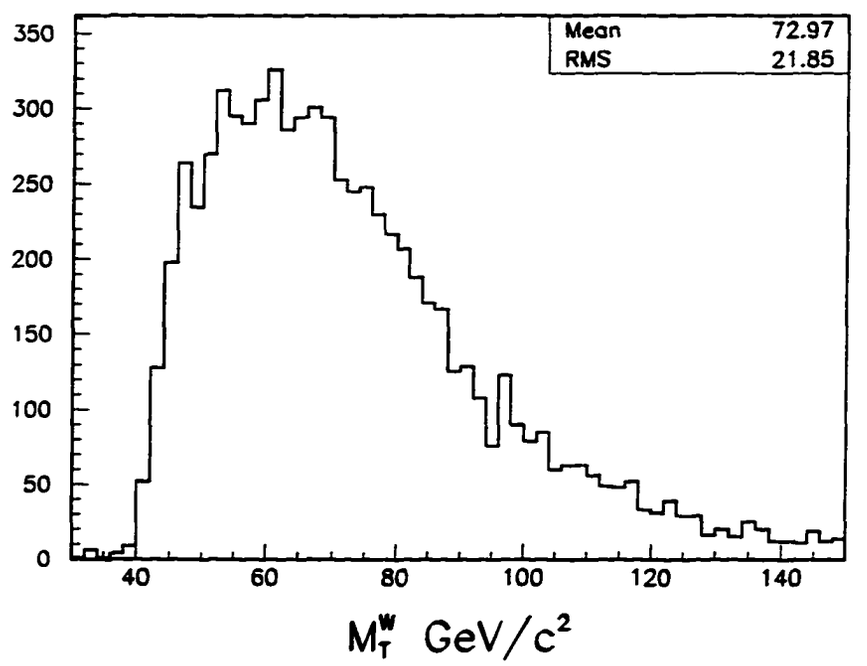

Figure 4.6: W boson transverse mass for Run 1B for the CF region.

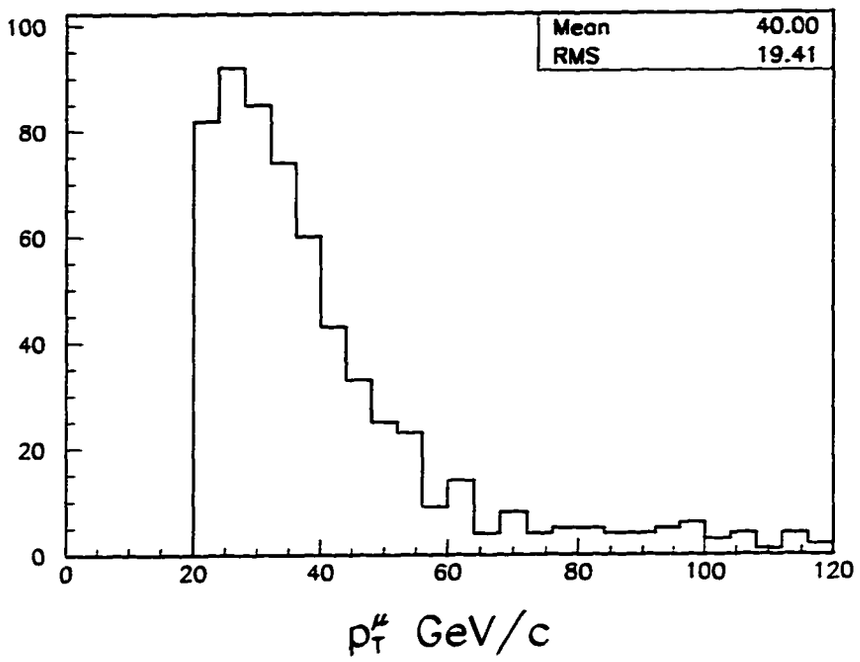

Figure 4.7: Transverse momenta of muons from Run 1B for the EF region.

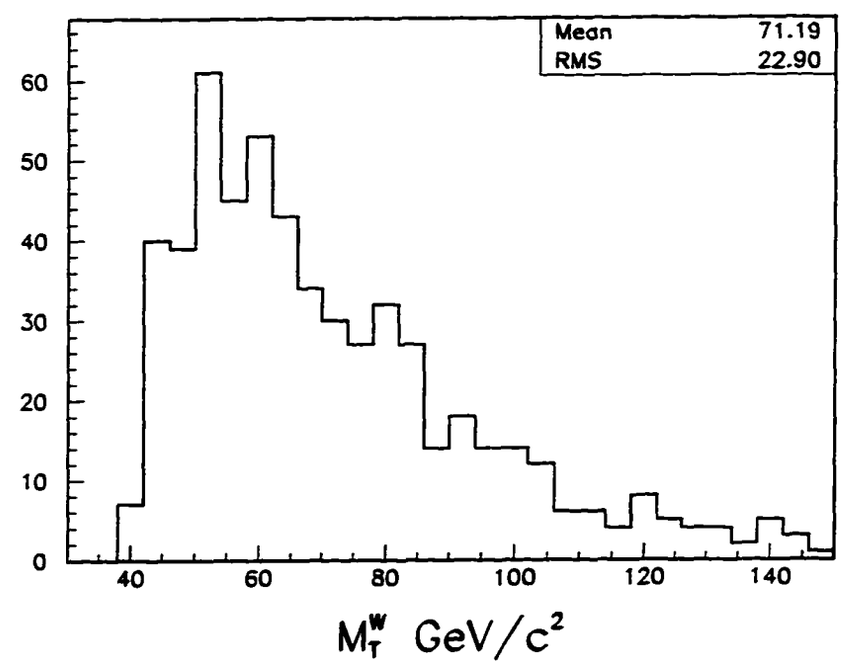

Figure 4.8: W boson transverse mass for Run 1B for the EF region.

CHAPTER 5

THE RAW CHARGE ASYMMETRY

5.1 Introduction

This chapter describes the raw charge asymmetry of the sample of muons selected with the criteria enumerated in Table 4.5. At this stage, the sample is contaminated by various background sources. It is also uncorrected for systematic effects. Thus it cannot be directly compared to theory. However describing the raw asymmetry is a convenient way to introduce some formulas and notations needed later. It can also be compared to the corrected asymmetry to show the effect of systematic and background corrections.

5.2 The Charge Asymmetry of Muons from W Decay

As explained in Chapter 2, the charge asymmetry of W bosons cannot be directly measured since the total momentum of the neutrino accompanying the decay cannot be measured. Instead the charge asymmetry of the decay leptons is measured. The DØ detector cannot differentiate between electrons and positrons owing to the lack of a central solenoidal magnetic field. The measurement is thus carried out using muons only. The charge asymmetry defined by (2.21) is

$$A(\eta_\mu) = \frac{d\sigma^+/d\eta_\mu - d\sigma^-/d\eta_\mu}{d\sigma^+/d\eta_\mu + d\sigma^-/d\eta_\mu}. \tag{5.1}$$

According to CP conservation the distribution of muons of one charge in the positive pseudorapidity half is equivalent to the distribution of oppositely charged muons in the negative pseudorapidity half. Thus we may combine the two pseudorapidity halves, effectively doubling the statistics in each η bin, and write (5.1) as

$$A(|\eta_\mu|) = \frac{N^+(|\eta_\mu|) - N^-(|\eta_\mu|)}{N^+(|\eta_\mu|) + N^-(|\eta_\mu|)}, \tag{5.2}$$

where,

$$\eta = \log\{\cot(\theta/2)\}$$

N^+ = number of μ^+ in the region $\eta > 0$ and μ^- in the region $\eta < 0$, and

N^- = number of μ^+ in the region $\eta < 0$ and μ^- in the region $\eta > 0$.

Tables 5.1 and 5.2 shows the number of muons of each charge in each eta bin for run 1A and run 1B, respectively, with the selection criteria described in the last chapter. The asymmetry obtained with this sample is termed the raw asymmetry since it has not yet been corrected for systematic effects or background contamination.

The statistical error on the raw asymmetry in Tables 5.1 and 5.2 and plotted in Figures 5.1 and 5.2 are given by

$$\sigma_A = \sqrt{4N^+N^-/(N^+ + N^-)^3}. \tag{5.3}$$

Here it has been assumed that the error in the numbers N^+ , N^- and N is Gaussian and thus equal to their square roots. If the asymmetry is small, then $(N^+ + N^- \approx N)$, $N^+ \approx N/2$, $N^- \approx N/2$ and $\sigma_A \approx \sqrt{1/N}$. This is true for the data in Tables 5.1 and 5.2.

The raw asymmetry is plotted in Figures 5.1 and 5.2. The horizontal bars show the extension of the bin used and the vertical bars indicate the statistical error. The points are plotted at the average η of the bin.

$< \lvert\eta_\mu\rvert >$	N^+	N^-	A($\lvert\eta_\mu\rvert$)
0.09	202	211	-0.022 ± 0.049
0.30	149	141	0.028 ± 0.059
0.50	147	124	0.085 ± 0.061
0.67	53	56	-0.028 ± 0.096
0.82	1	2	-0.333 ± 0.544
1.10	16	12	0.143 ± 0.187
1.36	25	23	0.042 ± 0.144

Table 5.1: The run 1A raw asymmetry.

$< \lvert\eta_\mu\rvert >$	N^+	N^-	A($\lvert\eta_\mu\rvert$)
0.09	1576	1549	0.009 ± 0.018
0.30	986	907	0.042 ± 0.023
0.49	1058	903	0.079 ± 0.023
0.68	414	330	0.113 ± 0.036
0.84	11	9	0.100 ± 0.223
1.11	132	116	0.065 ± 0.063
1.34	180	160	0.059 ± 0.054

Table 5.2: The run 1B raw asymmetry.

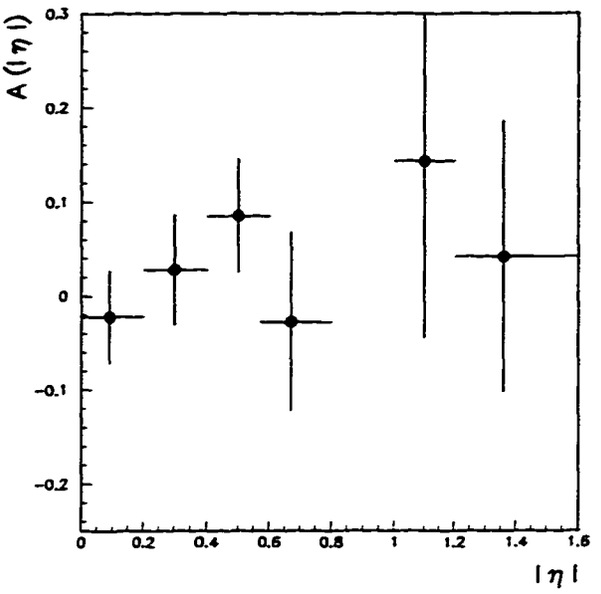

Figure 5.1: The run 1A raw asymmetry as a function of the muon pseudorapidity.

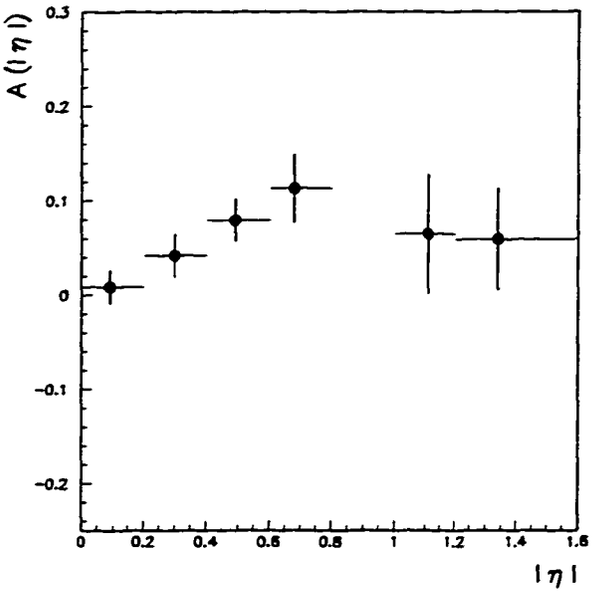

Figure 5.2: The run 1B raw asymmetry as a function of the muon pseudorapidity.

The unfolded raw asymmetry for run 1B is shown in Figure 5.3. It shows that the positive and negative pseudorapidity halves of the detector are symmetric and we are justified in presenting the folded asymmetry. Hence forth all discussions pertain only to the folded asymmetry.

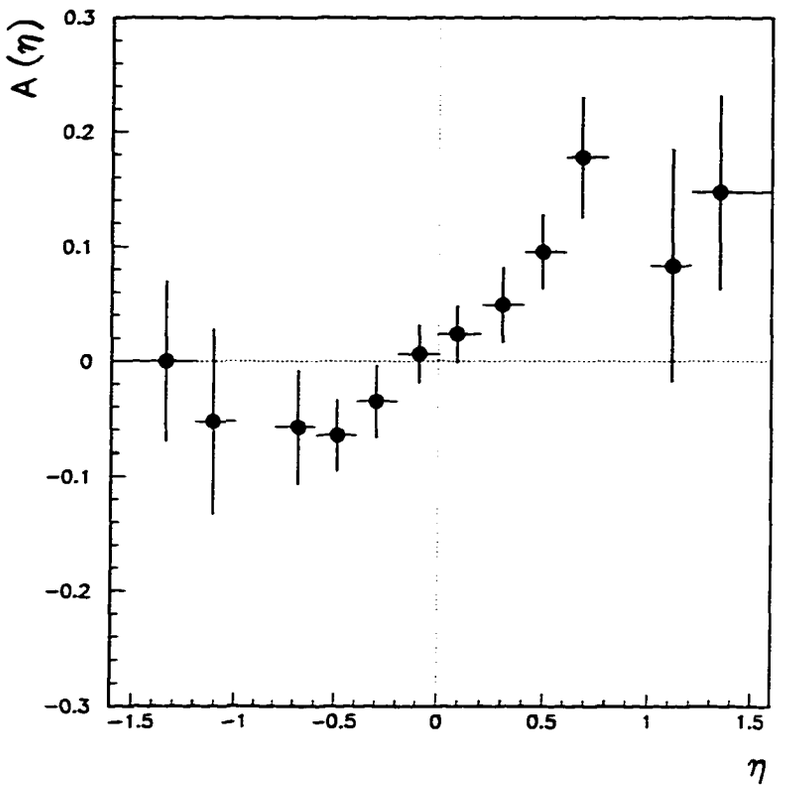

Figure 5.3: The run 1B unfolded raw asymmetry as a function of the muon pseudorapidity.

Corrections that need to be applied to the raw asymmetry are explained in the next two chapters.

CHAPTER 6

BACKGROUNDS

6.1 Introduction

The main contaminants in the W boson sample are cosmic ray muons, accidental hits in the muon detectors that mimic a muon track (termed combinatorics), muons from QCD processes, muons from the process $W \rightarrow \tau \rightarrow \mu$, and muons from the processes $Z^o \rightarrow (\mu)\mu$ and $Z^o \rightarrow \tau\tau \rightarrow (\mu)\mu$, where only one of the muons is detected.

Estimates of backgrounds due to cosmic ray muons, accidental hits and muons from QCD processes were made using data. The contribution from $Z^o \rightarrow (\mu)\mu$ was estimated from Monte Carlo studies since the number of these events numbered only 119 from Run 1A and 455 from Run 1B.

High purity samples of signal and background events were extracted from the WZM and the ALL stream respectively (Section 4.4). Variables that give distinct distributions for the two samples were identified. Fits to the data were then made using these signal and background distributions. The fractions of background events in the W candidate sample were found from these fits. Fits were performed separately for the CF and EF regions where the backgrounds are expected to be different.

6.2 Background due to Cosmic Ray Muons and Combinatorics

To find the background contribution of cosmic ray muons we first obtain a **signal** sample with the following cuts:

1. Muon $p_T > 5$ GeV/c
2. A matching track in the CD
3. Global Fit $0 < \chi^2 < 5$

4. Energy deposited in the calorimeter in a $\Delta(R) = \sqrt{\Delta\eta^2 + \Delta\phi^2}$= 0.2 cone, E(0.2) > 5 GeV
5. Non-bend view impact parameter, $b_{\text{non-bend}} < 20$ cm
6. Three layer tracks
7. Fraction of Calorimeter hadronic layers hit, HFRACT ≥ 0.75
8. IFW4=0

These selection criteria ensure that the muon tracks are of high quality. Since cosmic ray muons do not in general pass through the collision vertex, these cuts also substantially suppress cosmic ray and combinatoric backgrounds.

The **background** sample is obtained with the following cuts:

1. no matching CD track
2. Energy deposited in the calorimeter in a ΔR cone of 0.2, E(0.2) < 0.5 GeV
3. Fraction of Calorimeter hadronic layers hit, HFRACT ≤ 0.5
4. Non-bend view impact parameter, $b_{\text{non-bend}} > 40$ cm
5. Three layer track
6. IFW4=0

The last two cuts ensure that there are good reconstructed tracks while the first three cuts pick up cosmic ray muons and combinatorics.

Figure 6.1 shows the t_0^f distribution for the signal and background samples. Recall (Section 4.5.9) that t_0^f is an estimate of the time offset of the muon from beam crossing. The floating time distribution of beam-produced muons should peak at 0 ns. The arrival time of cosmic ray muons is random with respect to beam crossing and ideally the floating time distribution for cosmic ray muons should be flat. However, hits are recorded

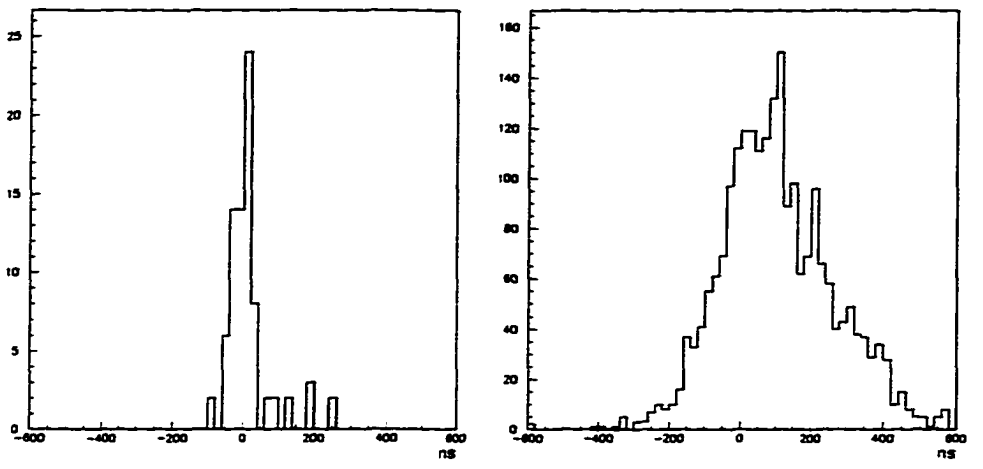

(a) Signal (b) Background

Figure 6.1: EF region floating time distribution for Run 1B signal and background events.

only if they drift to the wire inside an 800 ns "TSTOP" gate. In addition, the cathode pad latch circuits which flag a cell as being hit have a relatively slow rise time ($\approx$ 50 ns). These effects combine to give a broadly humped distribution which peaks around +100 ns. Recall that positive values correspond to early particles. The reasoning is not so clear for accidental and noise hits. However, they have a similar distribution [52].

The t_0^f distribution of the candidate sample is fit with a linear combination of the background and the signal distributions in t_0^f. Let the constants in this linear combination be P_1 and P_2, respectively. Then the background fraction in the candidate sample is

$$\frac{P1 * \epsilon_B^{\mathrm{CUT}}}{(P_1 + P_2)/\epsilon_S^{\mathrm{CUT}}}$$

where, ϵ_B^{CUT} is the efficiency of the 100 ns cut on the background distribution and $\epsilon_S^{\mathrm{CUT}}$ is the efficiency of the cut on the signal distribution. Figures 6.2 and 6.3 show the results of the fitting procedure for Run 1B. The values obtained for the cosmic ray muon and combinatoric background, $b_{\mathrm{Cos/Com}}$, are shown in Table 6.1. The errors shown are statistical errors. These values have been cross-checked by scanning for a small subset of the candidate sample.

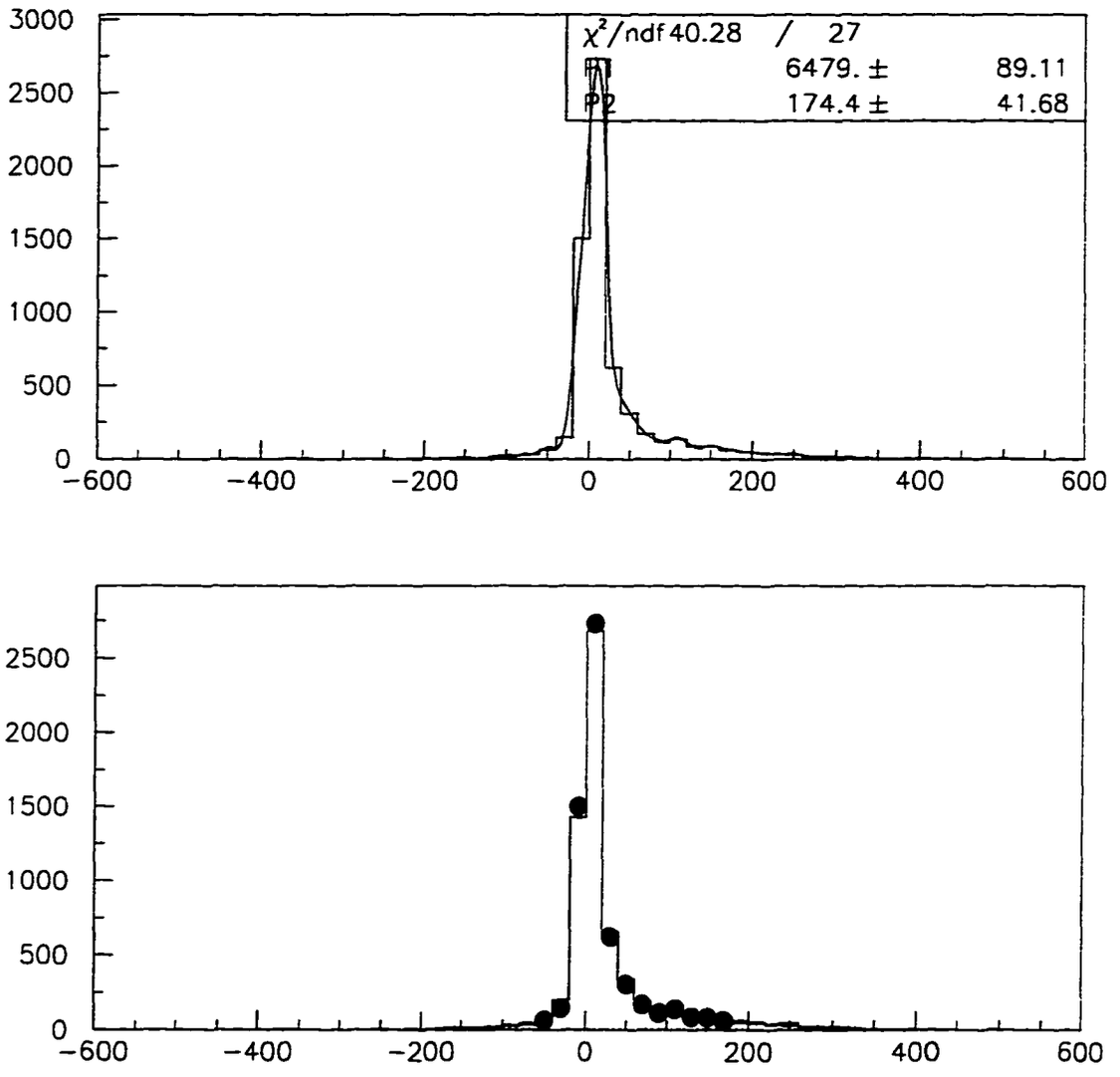

Figure 6.2: The top plot shows the linear combination of the signal and the background t_0^f distribution with the constants $P1$ and $P2$ indicated in the inset box. In the lower plot, the data points are shown as the points with the error bars, the histogram in dashed line represents the signal, the dotted line, the background, and the solid line, the linear combination. This plot is for the CF region for Run 1B.

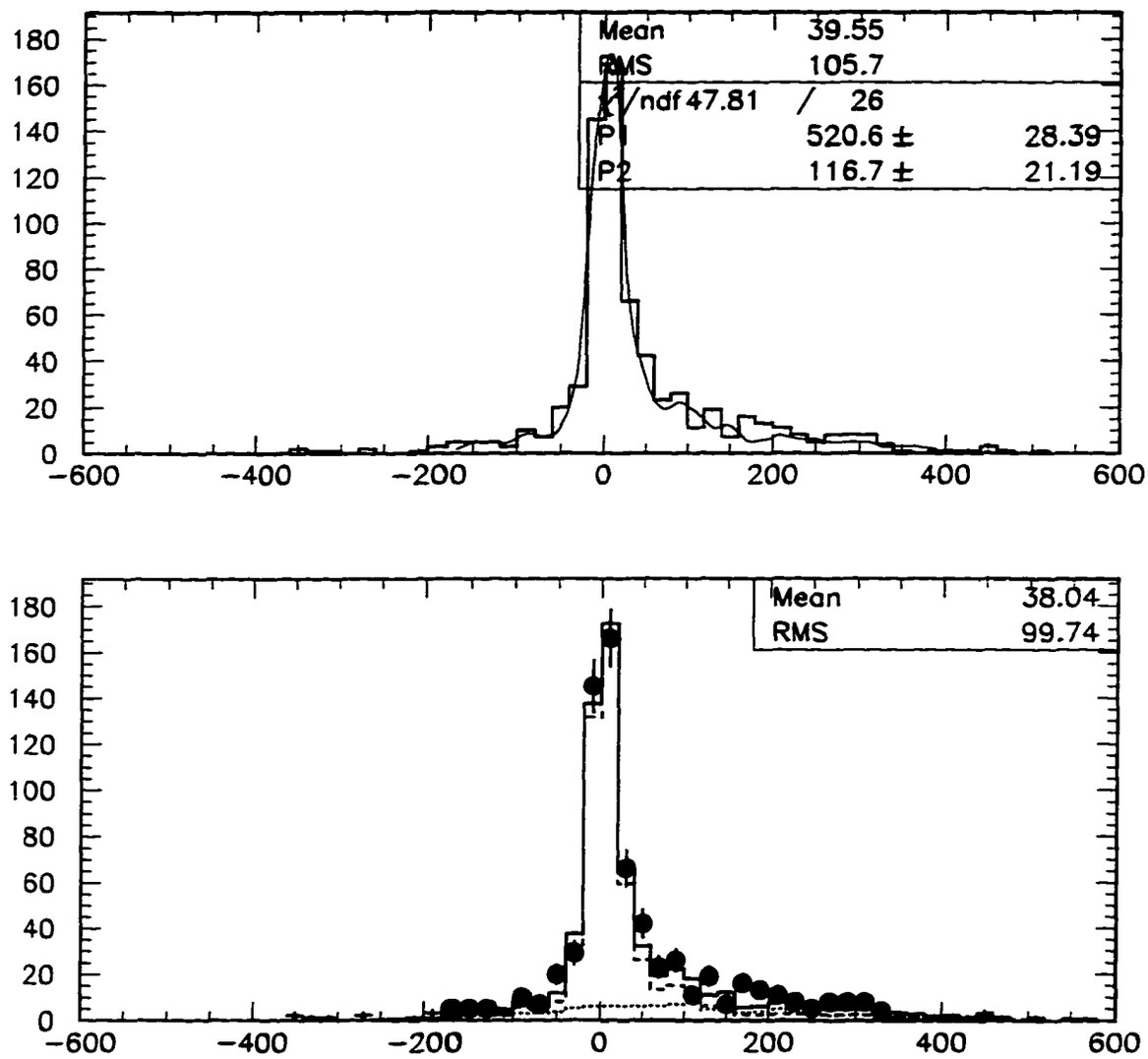

Figure 6.3: The top plot shows the linear combination of the signal and the background t_0^f distribution with the constants $P1$ and $P2$ indicated in the inset box. In the lower plot, the data points are shown as the points with the error bars, the histogram in dashed line represents the signal, the dotted line, the background, and the solid line, the linear combination. This plot is for the EF region for Run 1B.

Period	$b_{\text{Cos/Com}}$	
	CF	EF
Run 1A	3.8 ± 1.6	7.0 ± 5.4
Run 1B	1.1 ± 0.2	7.4 ± 1.3

Table 6.1: The percentage cosmic ray muon and combinatoric background.

6.3 Background from QCD Processes

The background from QCD processes consists mainly of non-isolated muons from b and c quark decays. Thus one would expect energy associated with the fragmentation of the b or c-quark to be deposited in the calorimeter in the vicinity of the track. π/K decays could also contribute but their decay cross section falls steeply with momentum. The track segments in the calorimeter for such muons are surrounded by cells with energy deposition. To estimate the background due to these processes, we use a parameter called the halo energy, $E_{\text{Halo}}(0.6 - 0.2)$. It is the energy deposited between two coaxial cones of radius 0.6 and 0.2 in $\eta - \phi$ space.

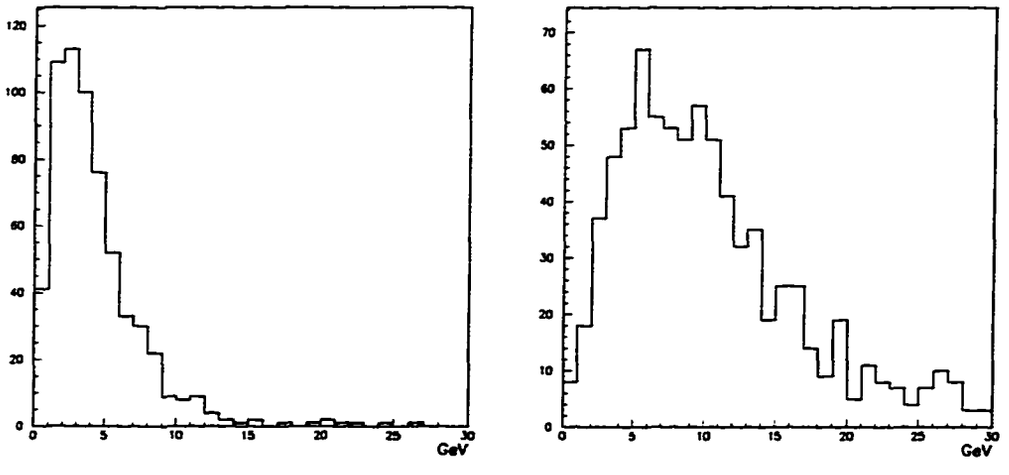

(a) Signal

(b) Background

Figure 6.4: EF region Halo energy distribution for Run 1B signal and background events.

The **signal sample** is the same as the $W \rightarrow \mu\nu$ sample (Table 4.2) with the additional requirement that there be no jet in the opposite hemisphere, in ϕ, with respect to the muon. The **background sample** consists of muons passing the $W \rightarrow \mu\nu$ selection cuts except that their p_T is required to lie between 5 GeV/c and 10 GeV/c . The fitting procedure is the same as that for the estimation of the cosmic and combinatoric backgrounds. The halo energy distributions for the signal and background samples are shown in Fig 6.4. Figures 6.5 and 6.6 show the results of the fitting procedure for Run 1B.

The background fraction due to muons from heavy or light quark decay in the $W \rightarrow \mu\nu$ sample is given in Table 6.2.

Period	b_{QCD}	
	CF	EF
Run 1A	5.1 ± 0.8	8.3 ± 1.1
Run 1B	6.4 ± 0.2	14.6 ± 2.4

Table 6.2: The percentage background from QCD processes.

As mentioned in Sections 3.8 and 3.9.4, the PDT's and the electronics for the EF region underwent changes during Run 1B. About half the Run 1B sample, from roughly a fifth of the total integrated luminosity, was obtained with fully efficient chambers. Also, the luminosities at which data was recorded were about a factor of 2 higher during Run 1B. These factors may explain the differences for the EF region numbers for Run 1A and Run 1b but this has not been verified.

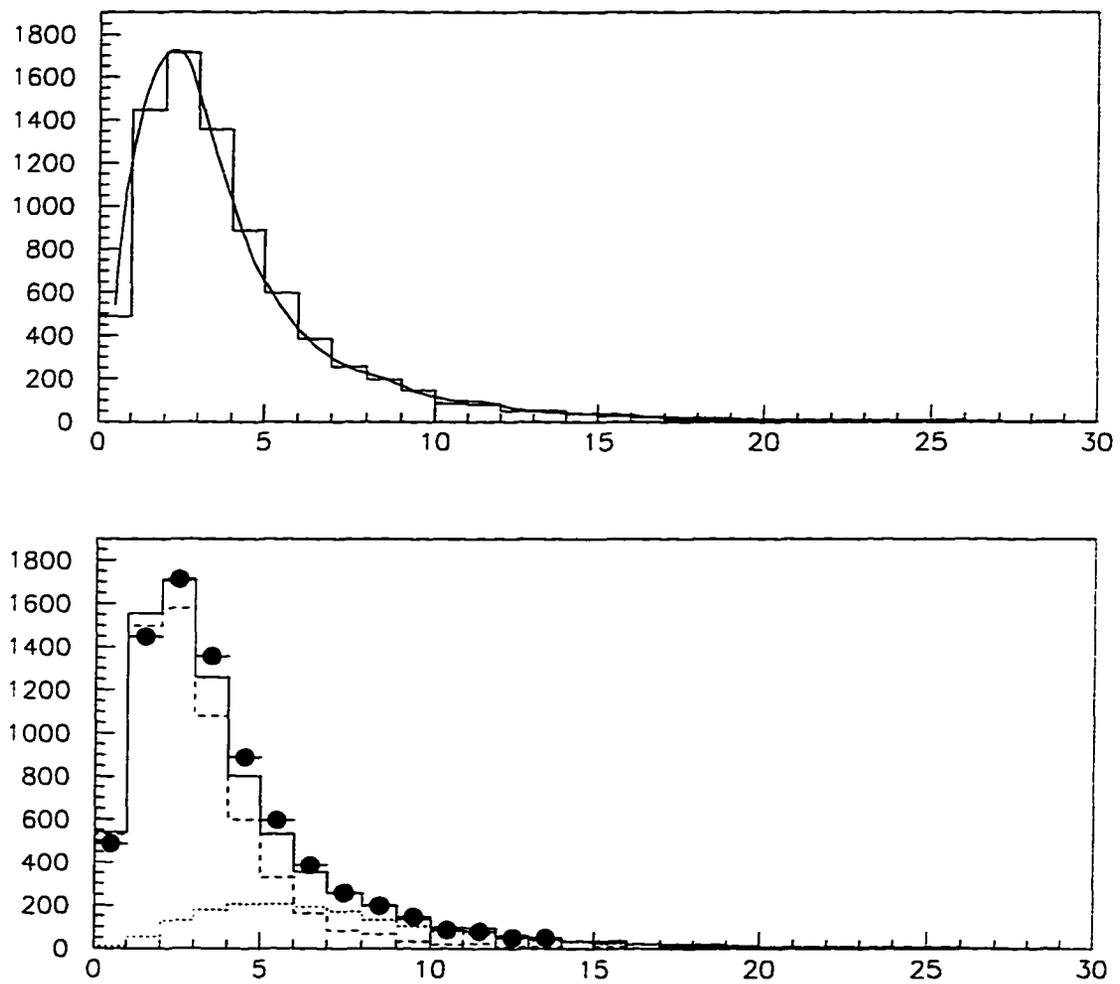

Figure 6.5: The top plot shows the linear combination of the signal and the background E_{Halo} distribution with the constants $P1$ and $P2$ indicated in the inset box. In the lower plot, the data points are shown as the points with the error bars, the histogram in dashed line represents the signal, the dotted line, the background, and the solid line, the linear combination. This plot is for the CF region for Run 1B.

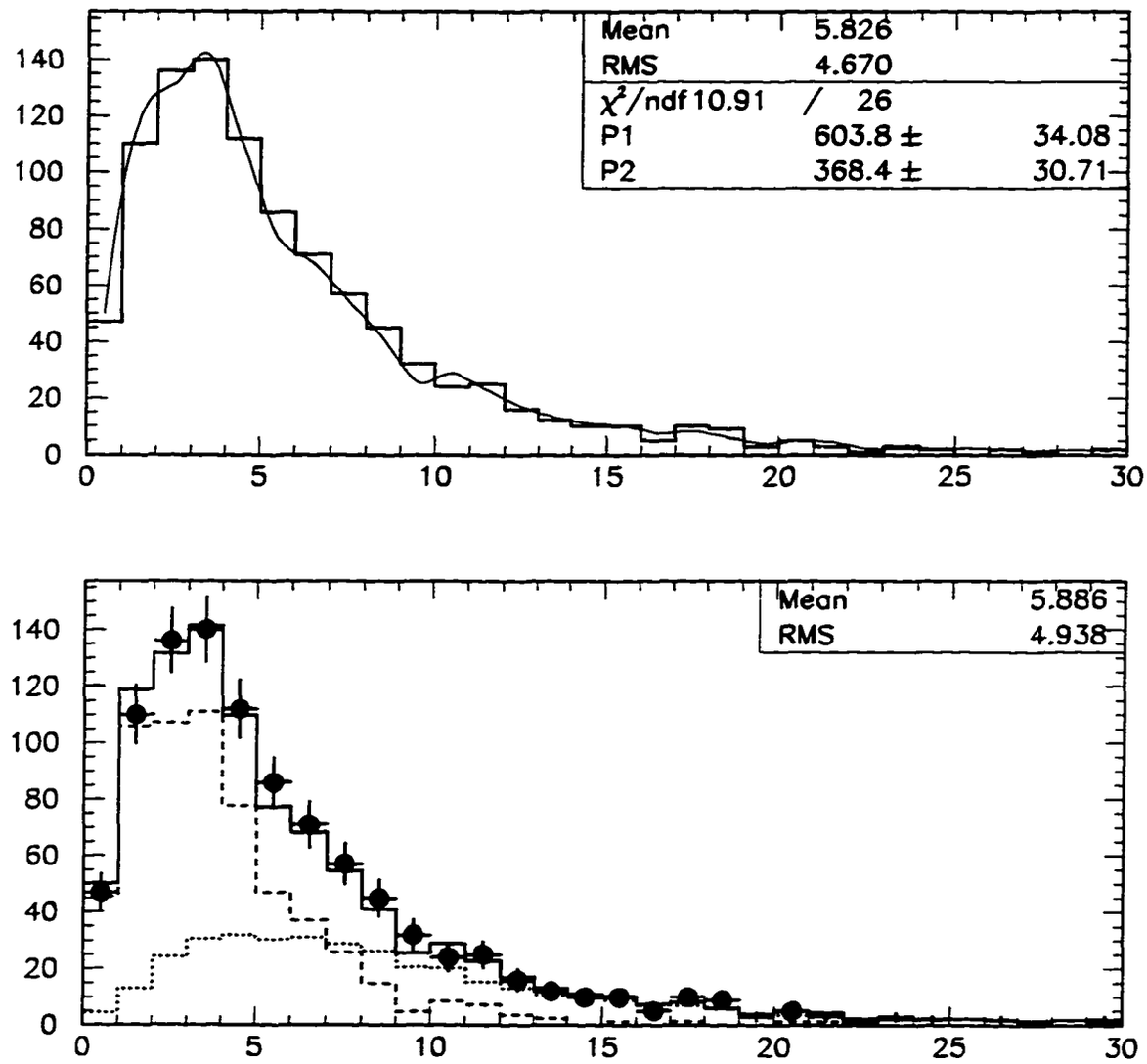

Figure 6.6: The top plot shows the linear combination of the signal and the background E_{Halo} distribution with the constants $P1$ and $P2$ indicated in the inset box. In the lower plot, the data points are shown as the points with the error bars, the histogram in dashed line represents the signal, the dotted line, the background, and the solid line, the linear combination. This plot is for the EF region for Run 1B.

6.4 One Legged $Z \rightarrow \mu\mu$

In the following discussion a Z decay refers to both $Z^o \rightarrow (\mu)\mu$ and $Z^o \rightarrow \tau\tau \rightarrow (\mu)\mu$. If one of the muons in a Z decay is not detected because it goes through uninstrumented regions of muon system or an inefficient portion of it, the event will look like a $W \rightarrow \mu\nu$ event because the single detected muon will be isolated and have large p_T while the p_T of the undetected muon will be accounted for as the missing $\not\!\!E_T$ associated with a neutrino. This background is estimated using Monte Carlo (MC) events since the data sample of Z events is small. Z decays do have a natural asymmetry which is not related to PDF's. This asymmetry stems from a term linear in $cos\theta$ due to the interference between the Z vector and axial vector couplings in the Z decay cross section [3]. This asymmetry is accounted for by the method employed here (6.4).

Z decay events from $p\bar{p}$ collisions at $\sqrt{s} = 1.8$ TeV are generated using the ISAJET 7.13 program. The events are then passed through full detector simulation based on the GEANT package. An additional package, based on collider data, called MUSMEAR[53] is used to make the detector model realistic. MUSMEAR "worsens" time resolutions. It also drops hits to simulate real efficiencies. These smearing effects are based on measurements from beam data. It also modifies muon geometry files to simulate chamber misalignments based on surveys done whenever the detector is accessed for repairs or maintenance. By using data files from different periods [20], MUSMEAR can simulate time dependent changes in efficiency and resolution of the muon system such as the dramatic improvement in efficiency of the EF regions chambers late in Run 1B.

The background may be estimated as follows

$$\begin{aligned} b_{Z^o \rightarrow (\mu)\mu} &= \frac{N_{Z_{[W]}}}{N_{W_{[W]}}} = \frac{\sigma_Z \cdot \mathcal{L} \cdot \mathcal{A}_{Z_{[W]}}}{\sigma_W \cdot \mathcal{L} \cdot \mathcal{A}_{W_{[W]}}} \\ &= \frac{\sigma_Z \cdot N^{[MC]}_{Z_{[W]}} \,/\, N^{[MC]}_{Z_{total}}}{\sigma_W \cdot N^{[MC]}_{W_{[W]}} \,/\, N^{[MC]}_{W_{total}}} \equiv f^{(MC)}_{Z^o \rightarrow (\mu)\mu} \end{aligned} \tag{6.1}$$

Here, $\mathcal{L}$ represents the luminosity, $\mathcal{A}$ is the acceptance and N denotes number of events. The subscripts $W_{[W]}$ and $Z_{[W]}$ stand for W selected with W selection cuts and Z selected with W selection cuts, respectively. To account for the fact that we have removed the

cosmic ray muon and combinatoric backgrounds from the data but not the other sources that we extract from Monte Carlo, we must use the following relation for the denominator in the first line of the above derivation.

$$\sigma_W \cdot \mathcal{L} \cdot \mathcal{A}_{W_{[W]}} \cdot (1 + \sum_i f_i^{(MC)}) = N_{\text{cand}}(1 - b_{\text{cos/comb}} - b_{\text{QCD}}). \qquad (6.2)$$

Here, the $f_i^{(MC)}$ are the fractions of respective Monte Carlo decay events that are detected as W boson for various sources. The sum is over all sources. In our case these sources are $Z^o \rightarrow \mu\mu$, $Z^o \rightarrow \tau\tau \rightarrow \mu\mu$ and $W \rightarrow \tau \rightarrow \mu$. $b_{\text{cos/comb}}$ and b_{QCD} are the background sources for cosmic ray muons plus combinatorics and muons from QCD processes. N_{cand} is the number of candidates.

Thus the background fraction is given by

$$b_{Z^o \rightarrow (\mu)\mu} = f^{(MC)}_{Z^o \rightarrow (\mu)\mu} \cdot \frac{(1 - b_{\text{cos/comb}} - b_{\text{QCD}})}{(1 + \sum_i f_i^{(MC)})}. \qquad (6.3)$$

The fraction of one legged Z background,in the $W \rightarrow \mu\nu$ sample, obtained in this manner, are shown in Table 6.3

Period	$b_{Z^o \rightarrow (\mu)\mu}$	
	CF	EF
Run 1A	7.3 ± 0.5	8.3 ± 1.1
Run 1B	7.0 ± 0.4	6.1 ± 0.8

Table 6.3: The percentage one legged Z background.

6.5 Background Subtraction

The background is subtracted bin by bin for each of the charge varieties N^+ and N^- for cosmic ray muons and combinatorics, muons from QCD sources and single legged Z decays.

The number of back ground events in each folded η-bin is determined separately for the CF and EF regions. It is assumed that the background fraction b is constant within these regions. For a given background source, the number of background events of each sign in each folded η-bin is given by

$$N_{BG}^{\pm}(\eta) = N_{\text{total}} \times b \times F(\eta) \times Q^{\pm}(\eta). \tag{6.4}$$

Here N_{total} is the total number of muons in the candidate sample, b represents the background fractions from Table 6.4 which are specific to the CF or the EF regions, $F(\eta)$ is the fraction of the events in each bin and $Q^{\pm}(\eta)$ is the respective fraction of the folded charge varieties N^+ or N^- within each bin. Figures 6.7 and 6.8 show the pseudorapidity distribution for the folded positive and negative charges, N^+ and N^-, for the candidate sample and the combined background for Run 1A and Run 1B data, respectively.

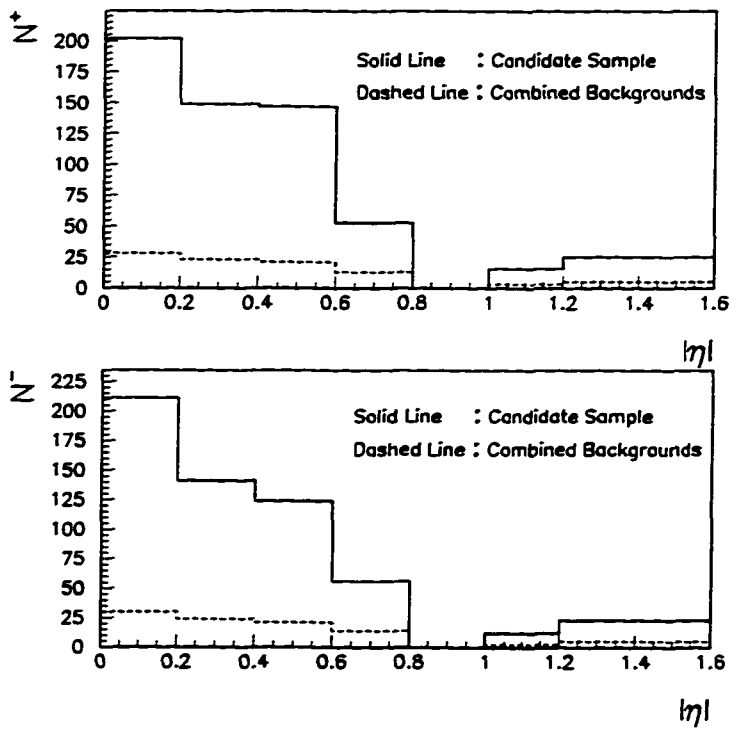

Figure 6.7: The distribution of N^+ and N^- in pseudo-rapidity in comparison with the number of candidates in each sample for Run 1A.

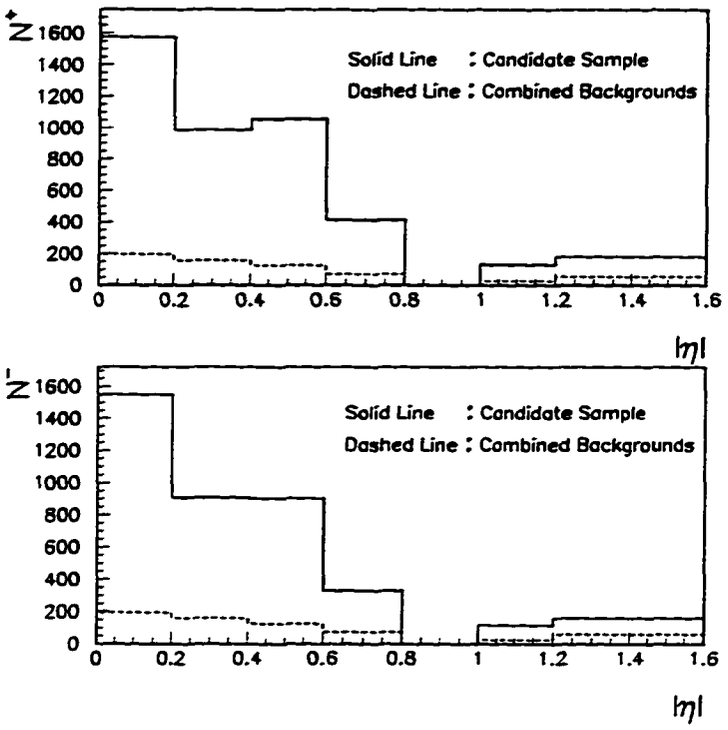

Figure 6.8: The distribution of N^+ and N^- in pseudo-rapidity in comparison with the number of candidates in each sample for Run 1B.

6.6 Correction for the $W \to \tau \to \mu$ Background

Muons from the sequential decay $W \to \tau \to \mu$ have a softer p_T spectrum. The branching ratio for these events, Br($\tau \to \mu\nu$)$\approx$ 17%. These muons have a different asymmetry than those from prompt $W \to \mu\nu$ decays.

Similar to $Z^o \to (\mu)\mu$, we first find the fraction

$$f^{(\mathrm{MC})}_{W\to\tau\to\mu} = \frac{\mathcal{A}_{W\to\tau\to\mu}}{\mathcal{A}_{W\to\mu\nu}} \times \mathrm{Br}(\tau \to \mu\nu)$$

Then the fraction of $W \to \tau \to \mu$ in the candidate sample is

$$b_{W\to\tau\to\mu} = f^{(\mathrm{MC})}_{W\to\tau\to\mu} \cdot \frac{(1 - b_{\mathrm{cos/comb}} - b_{\mathrm{QCD}})}{(1 + \sum_i f_i^{(MC)})}.$$

Period	$b_{W\to\tau\to\mu}$	
	CF	EF
Run 1A	5.9 ± 0.5	5.7 ± 0.9
Run 1B	4.4 ± 0.4	4.8 ± 0.6

Table 6.4: The percentage $W \to \tau \to \mu$ background.

Note that $b_{W\to\tau\to\mu}$ is the combined background due to muons of both charges. However, if the background to N^+ and N^- are b^+ and b^- , respectively, then

$$A_{\text{true}} = \frac{N^+ + (1-b^+) - N^-(1-b^-)}{N^+ + (1-b^+) + N^-(1-b^-)} = \frac{(N^+ - N^-) - (N^+b^+ - N^-b^-)}{(N^+ - N^-) - (N^+b^+ + N^-b^-)}.$$

Then using

$$(N^+b^+ + N^-b^-) = b_{W\to\tau\to\mu}(N^+ + N^-)$$

and identifying the asymmetry due to the $W \to \tau \to \mu$ to be

$$A_\tau = \frac{N^+b^+ - N^-b^-}{N^+b^+ - N^-b^-}$$

we get the true asymmetry to be

$$A_{\text{true}} = \frac{A_{\text{meas}} - A_\tau b_{W\to\tau\to\mu}}{1 - b_{W\to\tau\to\mu}}. \tag{6.5}$$

Since ISAJET does not handle W polarization, we use the fast Monte Carlo generator (Section. 2.6) to generate $W \to \tau \to \mu$ events and calculate their asymmetry $A_\tau(|\eta|)$. The asymmetry in each bin is then corrected according to (6.5).

The nominal value of A_τ is that obtained from using MRSA for the input PDF. The uncertainty assigned to A_τ is equal to the difference in A_τ values obtained by using MRSA and CTEQ2M. The values used in the correction are listed in Table 6.5.

$< \lvert\eta_\mu\rvert >$	$A(\lvert\eta_\mu\rvert)$
0.10	0.036 ± 0.005
0.30	0.054 ± 0.018
0.50	0.090 ± 0.028
0.70	0.125 ± 0.037
1.10	0.184 ± 0.050
1.40	0.211 ± 0.056

Table 6.5: The charge asymmetry of muons from $W \rightarrow \tau \rightarrow \mu$ decays.

6.7 Summary of Backgrounds

Source	Percentage Background			
	Run 1A		Run 1B	
	CF	EF	CF	EF
Cosmic Ray/Combinatorics	3.8 ± 1.6	7.0 ± 5.4	1.1 ± 0.2	7.4 ± 1.3
QCD	5.1 ± 0.8	5.3 ± 2.5	6.4 ± 0.2	14.6 ± 2.4
$Z^o \rightarrow (\mu)\mu$	7.3 ± 0.5	8.3 ± 1.1	7.0 ± 0.4	6.1 ± 0.8
$W \rightarrow \tau \rightarrow \mu$	5.9 ± 0.5	5.7 ± 0.9	4.4 ± 0.4	4.8 ± 0.6

Table 6.6: The percentage background in the candidate sample for Run 1A and Run 1B for the CF and the EF regions.

6.8 Background Corrected Asymmetry

The number of folded positive and negative muons, N^+ and N^- , from W decay after subtracting backgrounds due to cosmic rays and combinatorics, QCD processes and one-legged Z events are listed in Table 6.7 for Run 1A and 6.8 for Run 1B. The resulting

charge asymmetry values corrected for the $W \rightarrow \tau \rightarrow \mu$ background are also shown.

$< \lvert\eta_\mu\rvert >$	N^+	N^-	A($\lvert\eta_\mu\rvert$)
0.09	174	181	-0.024±0.059
0.30	126	118	0.032±0.072
0.50	126	103	0.101±0.074
0.67	40	42	-0.033±0.130
1.10	14	10	0.159±0.229
1.36	20	18	0.056±0.194

Table 6.7: Background corrected charge asymmetry for Run 1A.

$< \lvert\eta_\mu\rvert >$	N^+	N^-	A($\lvert\eta_\mu\rvert$)
0.09	1379	1354	0.008±0.022
0.30	829	749	0.051±0.030
0.49	932	777	0.091±0.027
0.68	345	258	0.144±0.048
1.11	106	93	0.060±0.084
1.34	126	102	0.097±0.093

Table 6.8: Background corrected charge asymmetry for Run 1B.

These asymmetries must be corrected for detector effects that are discussed in the next chapter.

6.9 A Note on the Charge Asymmetry of Background Sources

Assume that we have a charge symmetric background source and that its fraction in the candidate sample is b. If N^+ and N^- are the true folded charge varieties, the measured charge asymmetry will be

$$\begin{aligned} A_{\text{measured}} &= \frac{N^+ + (N^+ + N^-)b/2 - N^- - (N^+ + N^-)b/2}{N^+ + (N^+ + N^-)b/2 + N^- + (N^+ + N^-)b/2} \\ &= \frac{N^+ - N^-}{N^+ + N^-} \cdot \frac{1}{(1+b)}, \\ \text{or, } A_{\text{true}} &= A_{\text{measured}}(1+b). \end{aligned} \tag{6.6}$$

Thus a charge symmetric background source would *dilute* the charge asymmetry.

Figure 6.9 shows the charge asymmetry for the Run 1B background sample consisting of comsic ray muons and accidental hits selected with the cuts defined in Section 6.2. The asymmetry is flat in pseudorapidity with a value of -0.044 $\pm$ 0.022.

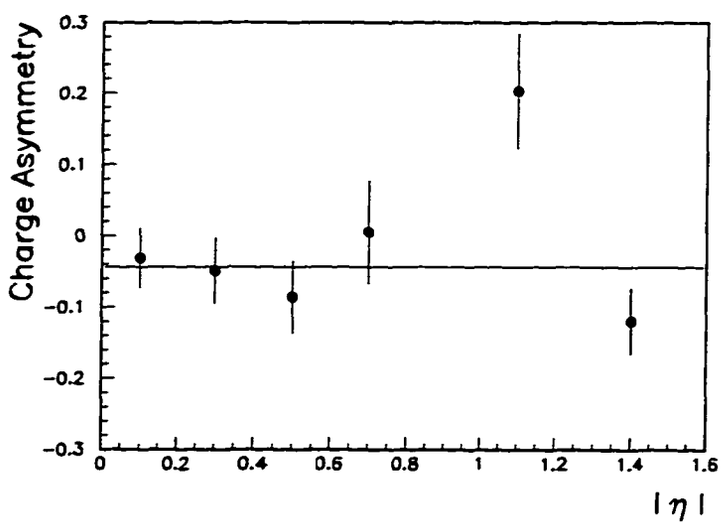

Figure 6.9: The charge asymmetry for the cosmic/combinatoric sample for Run 1B.

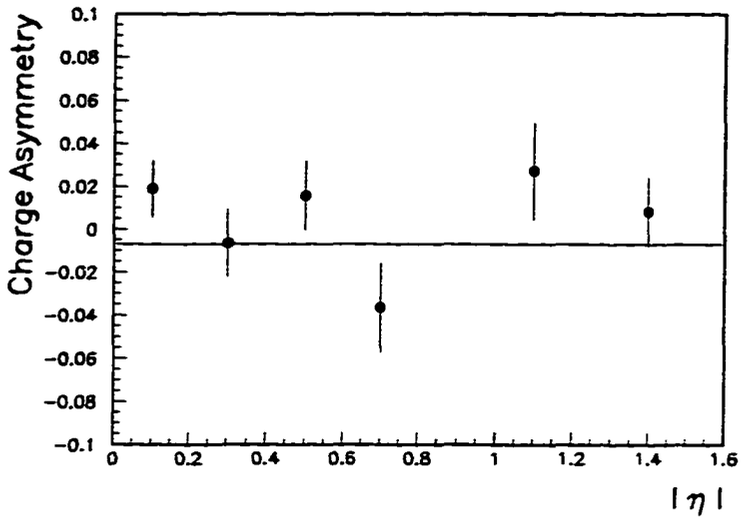

Figure 6.10: The charge asymmetry for the QCD sample for Run 1B.

Figure 6.10 shows the charge asymmetry for the Run 1B background sample consisting of muons selected from QCD processes with the cuts defined in Section 6.3. The asymmetry is flat in pseudorapidity with a value of -0.007 $\pm$ 0.007.

CHAPTER 7

DETECTOR EFFECTS

7.1 Introduction

The detector can contribute a charge asymmetry if μ^+ and μ^- particles are detected with different efficiencies. This chapter describes how this systematic effect was minimized and the steps taken to correct for that remaining in the sample.

7.2 Detector Asymmetry

There are numerous cracks in the coverage of the muon drift chambers, for example, due to support structures. If muons of one charge are bent into drift chambers while those with the other are bent into a region without a detector or an inefficient one, then we have a difference in detection efficiency for the two charges. Vertex shifts can also produce such an effect. Figure 7.1 shows a schematic representation of this effect.

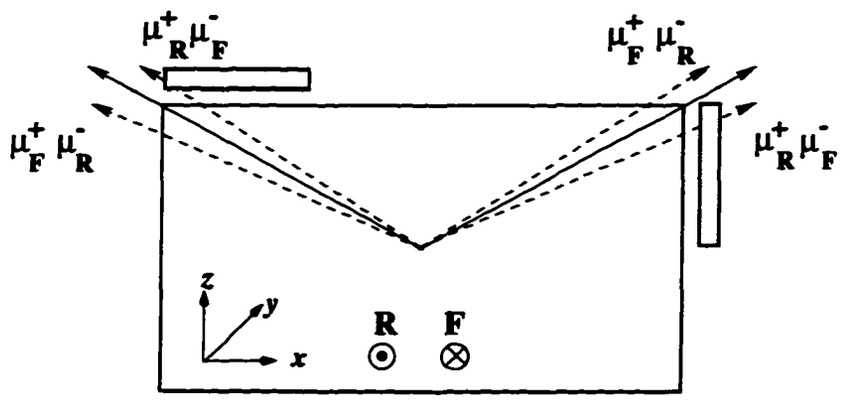

Figure 7.1: Cartoon of a detector asymmetry effect.

In Figure 7.1, **F** and **R** represent the forward and reverse polarities of the muon toroid. The solid arrow represents a track of infinite momentum and the dashed arrows repre-

sent the direction muons with smaller momenta have when they reach a layer of muon chambers outside the iron toroid.

Figure 7.2 shows the raw asymmetries computed separately for data collected with forward and reverse polarities for Run 1A and Figure 7.3 shows a similar plot for Run 1B.

7.3 Corrections for Detector Asymmetry

Let the efficiencies for detecting N^+ and N^- be ϵ^+ and ϵ^- respectively. The measured asymmetry, A_M, will then be given by

$$A_M(|\eta|) = \frac{N^+(|\eta|)\epsilon^+(|\eta|) - N^-(|\eta|)\epsilon^-(|\eta|)}{N^+(|\eta|)\epsilon^+(|\eta|) + N^-(|\eta|)\epsilon^-(|\eta|)}. \tag{7.1}$$

From here on, in this discussion, it is taken as understood that all quantities mentioned herein are functions of the absolute value of the pseudo-rapidity, $|\eta|$. The last equation can be written as

$$A_M(|\eta|) = \frac{N^+ - (1+\epsilon)N^-}{N^+ + (1-\epsilon)N^-}, \tag{7.2}$$

where,

$$\epsilon = (\epsilon^- - \epsilon^+)/\epsilon^+.$$

The true asymmetry, A_T, is then given by

$$A_T \approx A_M + \frac{\epsilon}{2}(1 - {A_T}^2), \tag{7.3}$$

or, to first order,

$$A_T = A_M + \frac{\epsilon}{2}. \tag{7.4}$$

The factor ϵ can be found by taking data with magnet polarities in the forward and reverse directions and measuring the double ratio

$$\begin{aligned} D &= \frac{\text{Observed No: } N_F^+ \text{ / Observed No: } N_F^-}{\text{Observed No: } N_R^+ \text{ / Observed No: } N_R^-} \\ &= \frac{N_F^+\epsilon_F^+ \,/\, N_F^-\epsilon_F^-}{N_R^+\epsilon_R^+ \,/\, N_R^-\epsilon_R^-}\ . \end{aligned} \tag{7.5}$$

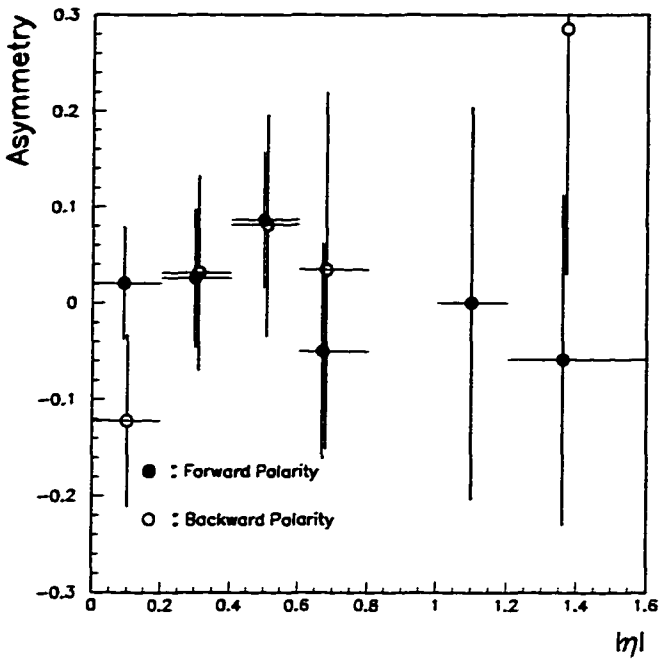

Figure 7.2: The raw asymmetry for forward and backward polarities for Run 1A.

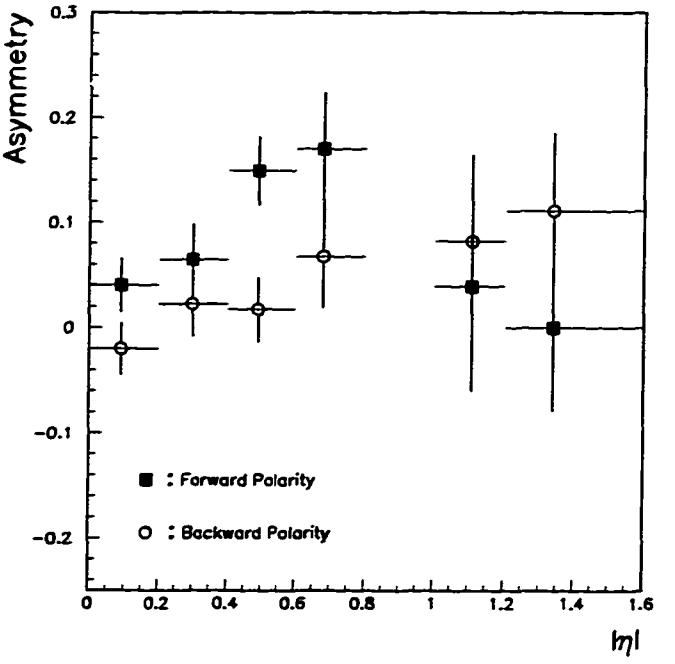

Figure 7.3: The raw asymmetry for forward and backward polarities for Run 1B.

Here, $N_{F(R)}^{+(-)}$ are the number of $\mu^{+(-)}$ incident upon a $|\eta|$-bin with the magnet polarity in the forward (reverse) directions respectively. $\epsilon_{F(R)}^{+(-)}$ are the respective detection efficiencies.

Now, since the μ^+ and μ^- are produced in equal numbers and the detection efficiency of muon chambers is independent of the charge, it is true that

$$N_F^+ = N_F^-,\ N_R^+ = N_R^-,\ \epsilon_F^+ = \epsilon_R^- \text{ and } \epsilon_F^- = \epsilon_R^+. \tag{7.6}$$

Hence the double ratio can be written as

$$D = \frac{\epsilon_F^+ / \epsilon_F^-}{\epsilon_R^+ / \epsilon_R^-} = \left(\frac{\epsilon_F^+}{\epsilon_F^-}\right)^{-2} = \left(\frac{\epsilon_F^-}{\epsilon_F^+} - \frac{\epsilon_F^+}{\epsilon_F^+} + 1\right)^{-2} = (1+\epsilon_F)^{-2}. \tag{7.7}$$

Similarly,

$$D = \left(\frac{\epsilon_R^+}{\epsilon_R^-} - \frac{\epsilon_R^-}{\epsilon_R^-} + 1\right)^{-2} = (1-\epsilon_R)^{-2}. \tag{7.8}$$

Denoting

$$\epsilon_F = -\epsilon_R = \epsilon,$$

yields,

$$D = \frac{1}{(1+\epsilon)^2}. \tag{7.9}$$

Since the magnitude of ϵ must be less than unity, the only solution for ϵ is

$$\epsilon = \frac{1}{\sqrt{D}} - 1 \tag{7.10}$$

and the error on ϵ is given by

$$\sigma_\epsilon = \frac{1}{2} D^{-3/2}\, \sigma_D\ . \tag{7.11}$$

If, as it happened during both Run 1A and Run 1B, unequal amounts of data are taken with forward and reverse polarities, then ϵ must be multiplied by $\mathcal{L}_X$, the fractional difference between the forward and reversed luminosities

$$\mathcal{L}_X = \frac{\mathcal{L}_F - \mathcal{L}_R}{\mathcal{L}_{total}}, \qquad \text{with} \qquad \mathcal{L}_F + \mathcal{L}_R = \mathcal{L}_{total}$$

Then equation 7.4 becomes

$$A_T = A_M + \frac{\epsilon}{2} \cdot \mathcal{L}_X \,. \tag{7.12}$$

The numerical values of the unbalanced luminosities and the detector asymmetry parameters for the two run periods are given in the next two sections.

7.4 Unbalanced Luminosity

During Run 1A, the benefits of taking equal amounts of data with alternate magnet polarities was realized late into the run. For this period $\mathcal{L}_X$=0.2. During Run 1B the magnet polarity was switched every week to collect roughly equal amounts of data with forward and reverse polarities. Over the course of Run 1B the triggers for the CF and EF Run 1B were prescaled differently. Thus there are two different values: $\mathcal{L}_X^{CF}$=-0.064 and $\mathcal{L}_X^{EF}$=-0.030. So there was a small excess of events with the toroid in reverse polarity.

7.5 Detector Asymmetry Parameters: D and ϵ

For Run 1A the double ratio was obtained from a set of events that contained a muon and a jet used in the t-quark search analysis since this was a larger sample than the $W \rightarrow \mu\nu$ data sample. The isolation requirement was removed and all other cuts used were the same as for the selection of W-candidates except that the p_T requirement was lowered to be at least 14 GeV/c to gain statistics. The detector asymmetry obtained in this fashion would be an overestimate because the lower transverse momentum muons bend more in the toroidal magnetic field. Figure 7.4 shows the double ratio D and the detector asymmetry parameter ϵ for Run 1A.

For Run 1B the double ratio was obtained from the $W \rightarrow \mu\nu$ candidate sample. Figure 1.5 shows the double ratio D and the detector asymmetry parameter ϵ for Run 1B.

7.6 Detector asymmetry corrected values

The detector asymmetry corrections shown in Figures 7.4 and 7.5 are applied to each $|\eta|$-bin in accordance with equation 7.12 with the appropriate values of $\mathcal{L}_X$. The corrected

charge asymmetry values are shown in Table 7.1 for Run 1A and Table 7.2 for Run 1B, respectively.

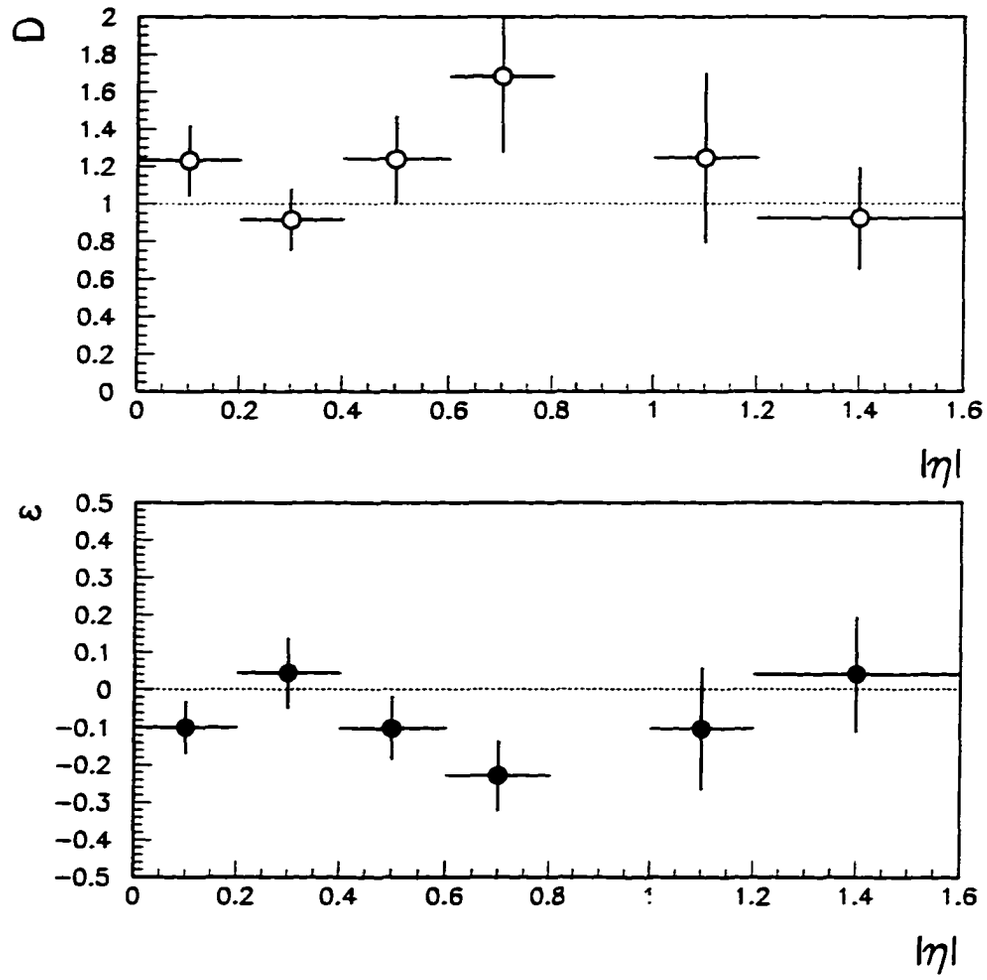

Figure 7.4: The top plot shows the double ratio D for each η-bin for Run 1A. The dotted line at $D = 1$ indicates the value for a perfect detector. The bottom plot shows ϵ which should be zero for an ideal detector as indicated by the dotted line.

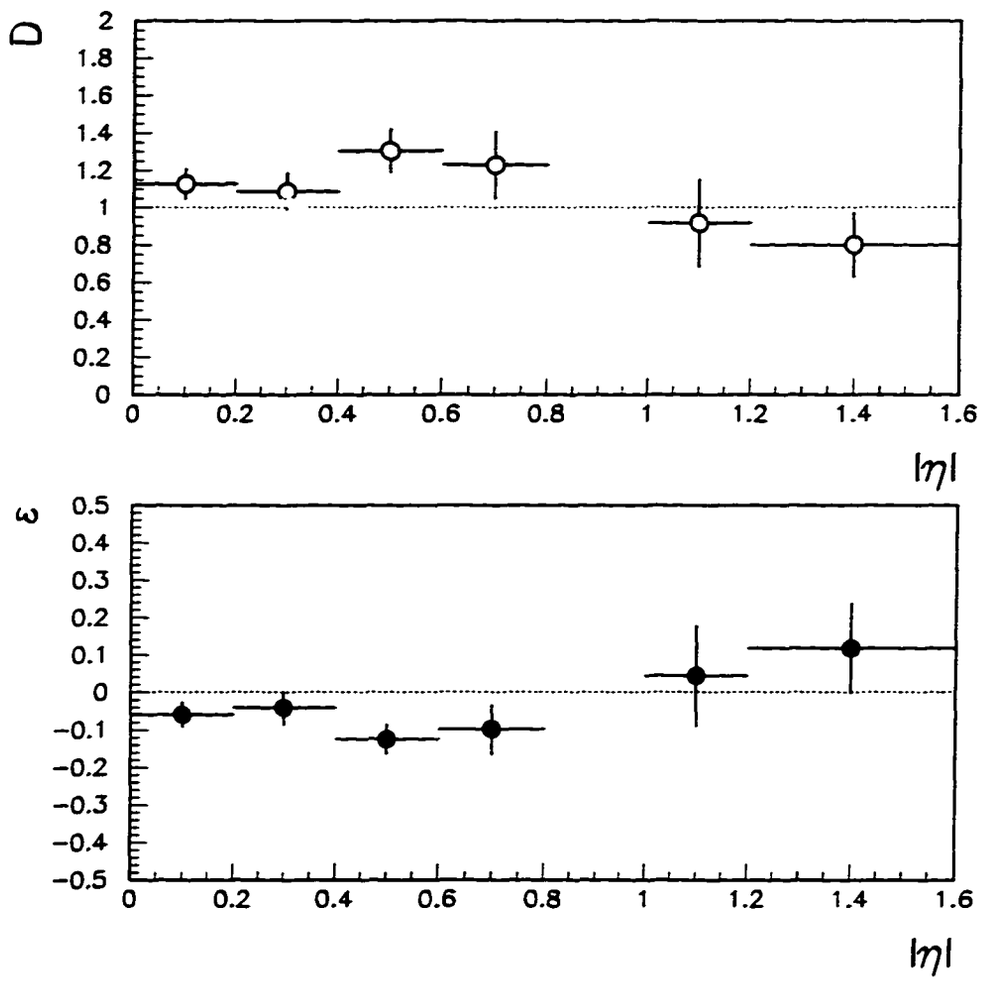

Figure 7.5: The top plot shows the double ratio D for each η-bin for Run 1B. The dotted line at $D = 1$ indicates the value for a perfect detector. The bottom plot shows ϵ which should be zero for an ideal detector as indicated by the dotted line.

$< \|\eta_\mu\| >$	N^+	N^-	ϵ	A($\|\eta_\mu\|$)
0.09	174	181	-0.099 ± 0.069	-0.034±0.060
0.30	126	118	0.045 ± 0.093	0.036±0.074
0.50	126	103	-0.101 ± 0.084	0.091±0.075
0.67	40	42	-0.229 ± 0.094	-0.056±0.130
1.10	14	10	-0.104 ± 0.163	0.148±0.230
1.36	20	18	0.041 ± 0.153	0.060±0.195

Table 7.1: The Run 1A asymmetry after background and detector asymmetry corrections.

$< \|\eta_\mu\| >$	N^+	N^-	ϵ	A($\|\eta_\mu\|$)
0.09	1379	1354	-0.059 ± 0.034	0.010±0.022
0.30	829	749	-0.041 ± 0.044	0.053±0.030
0.49	932	777	-0.125 ± 0.040	0.095±0.027
0.68	345	258	-0.596 ± 0.205	0.148±0.048
1.11	106	93	0.044 ± 0.135	0.059±0.084
1.34	126	102	0.118 ± 0.122	0.095±0.094

Table 7.2: The Run 1B asymmetry after background and detector asymmetry corrections.

7.7 Charge Mismeasurement

If the charge sign of the muon is misidentified, the charge asymmetry will be diluted. The probability of sign misidentification is estimated and corrected for as follows. Since the p_T^μ and η^μ distributions from W and Z bosons are similar, we use a sample of muons from Z decays.

Muons tracks originating in a Z decay event have to satisfy the same quality cuts as muons from a W -decay (Table 4.5). Both muons are required to have a p_T of at least 20 GeV/c . This is a tighter cut than the one used for Z candidate selection where one leg is

allowed to have a minimum p_T of 15 GeV/c . To suppress cosmic ray muons an angular separation in the polar and azimuthal angle less than 170 degrees is required. To suppress low mass dimuon pairs such as those from b-meson decays, the angular separation in the azimuthal angle between the two tracks is required to be greater than 30 degrees.

The total number of muon pairs that satisfy these Z selection criteria when no cut is made on the charge sign of the muon tracks is found. Next, the number of pairs that satisfy the Z selection criteria with both tracks having the same sign is found. The ratio, R, of the second to the first number is related to the charge misidentification probability, p_c, since the tracks in a Z event must have opposite signs. This relation is derived below

We have measured

$$R = \frac{\text{Number of same sign pairs}}{\text{Total number of pairs}}$$

Let F be the sign mismeasurement probability for one track. A same sign pair is seen if only one of the muon track is identified with the wrong sign but not both. Probability theory gives the identity for the probability of one or the other of two mutually exclusive events A and B, to be

$$P(A+B) = P(A) + P(B) - 2P(AB), \tag{7.13}$$

The probability of seeing a same sign pair may be obtained by substituting $P(A) = P(B) = F$ and $P(AB) = P(A) \cdot P(B)$. Thus,

$$R = 2 \cdot F \cdot (1 - F). \tag{7.14}$$

Solving for F gives

$$F = \frac{1}{2}(1 \pm \sqrt{1 - 2R}) \tag{7.15}$$

The relation between R and F is plotted in Figure 7.7. Since R must satisfy $0 \leq R \leq 1.0$, the realistic root is the one that gives $F \leq 0.5$

$$F = \frac{1}{2}(1 - \sqrt{1 - 2R}). \tag{7.16}$$

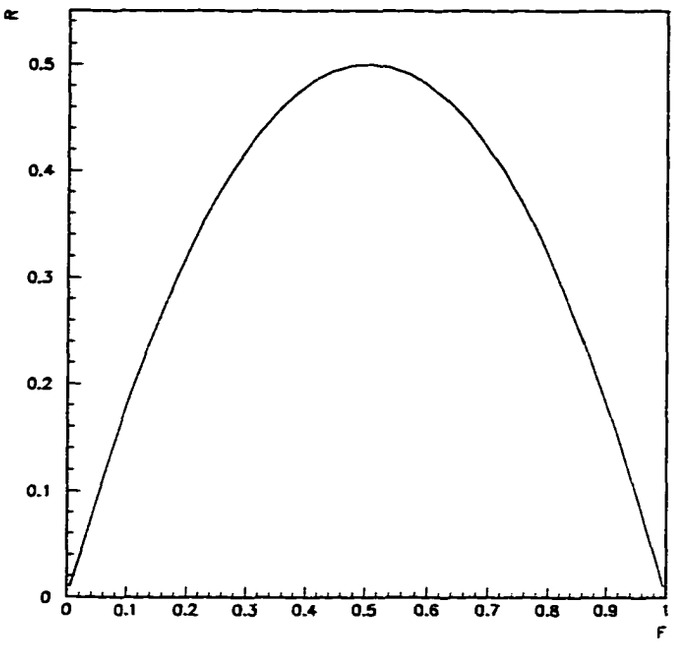

Figure 7.6: A plot of R versus F. The chosen root corresponds to the first half of the parabola for values of $F \leq 0.5$

The same sign ratio and the sign misidentification probability for Run 1A and Run 1B are listed in Table 7.3. It must be noted that the sample used consists of Z events with atleast one muon track in the CF region.

Period	R	F
Run 1A	0.160 ± 0.086	0.088 ± 0.154
Run 1B	0.053 ± 0.014	0.027 ± 0.007

Table 7.3: The ratio of same sign pairs, R, in a sample of Z -events and the associated sign misidentification probability.

If there is a non-zero sign misidentification probability, the measured asymmetry is given by

$$A_M = \frac{N^+(1-F) + N^-F - N^-(1-F) - N^+F}{N^+ + N^-}.$$

The true asymmetry is then

$$A_T = \frac{A_M}{(1-F)}. \tag{7.17}$$

Tables 7.4 and 7.5 list the asymmetry values corrected for sign mismeasurement for Run 1A and Run 1B.

$< \lvert\eta_\mu\rvert >$	A($\lvert\eta_\mu\rvert$)
0.09	-0.041±0.075
0.30	0.044±0.091
0.50	0.111±0.099
0.67	-0.067±0.160
1.10	0.180±0.287
1.36	0.073±0.238

Table 7.4: The Run 1A asymmetry after background, detector asymmetry and sign misidentification corrections.

$< \lvert\eta_\mu\rvert >$	A($\lvert\eta_\mu\rvert$)
0.09	0.010±0.023
0.30	0.056±0.031
0.49	0.100±0.029
0.68	0.156±0.051
1.11	0.063±0.088
1.34	0.101±0.099

Table 7.5: The Run 1B asymmetry after background, detector asymmetry sign misidentification corrections.

This is the final correction to be applied and as such the asymmetry values in the last two tables represent the true asymmetry.

CHAPTER 8

RESULTS AND CONCLUSIONS

8.1 Introduction

This chapter summarizes the W charge asymmetry after all the corrections mentioned in Chapters 6 and 7. The measurements are also compared to predictions from various parton distribution functions.

8.2 Corrections and Error Propagation

The raw number of positively and negatively charged muons, N^+ and N^- , are shown in tables 5.1 and 5.2 for Run 1A and Run 1B, respectively. Background fractions from various sources are summarized in Table 6.6. These are used in (6.4) to estimate the background contribution to N^+ and N^- due to the first three sources in Table 6.6. These are subtracted from the respective raw values for N^+ and N^- and the charge asymmetry is calculated. The $W \rightarrow \tau \rightarrow \mu$ background contribution is then corrected using (6.5). The resulting background corrected values are collected in Tables 6.7 and 6.8. The charge asymmetry values increase as expected from Section 6.9.

Next, corrections to the measured charge asymmetry are applied for detector asymmetry (7.12) and charge misidentification (7.17). The resulting charge asymmetry values, after all corrections, are listed in Tables 8.1 and 8.2 for Run 1A and Run 1B, respectively.

The statistical error on the raw number of N^+ and N^- in each $|\eta|$-bin is given by Poisson statistics, namely the square root of the number of events. Propagation of errors using the mean values without errors for the fraction of background events, detector asymmetry and sign misidentification probability yields the statistical error.

The dominant systematic error comes from the statistics of the samples used to determine the background fractions, detector asymmetry and sign misidentification. These

errors are propagated along with the statistical error on the raw values of N^- and N^+ to obtain the total error listed in Tables 8.1 and 8.2.

$< \|\eta_\mu\| >$	A($\|\eta_\mu\|$)
0.09	-0.041±0.075
0.30	0.044±0.091
0.50	0.111±0.099
0.67	-0.067±0.160
1.10	0.180±0.287
1.36	0.073±0.238

Table 8.1: The Run 1A charge asymmetry of muons from W decay after all corrections.

$< \|\eta_\mu\| >$	A($\|\eta_\mu\|$)
0.09	0.010±0.023
0.30	0.056±0.031
0.49	0.100±0.029
0.68	0.156±0.051
1.11	0.063±0.088
1.34	0.101±0.099

Table 8.2: The Run 1A charge asymmetry of muons from W decay after all corrections.

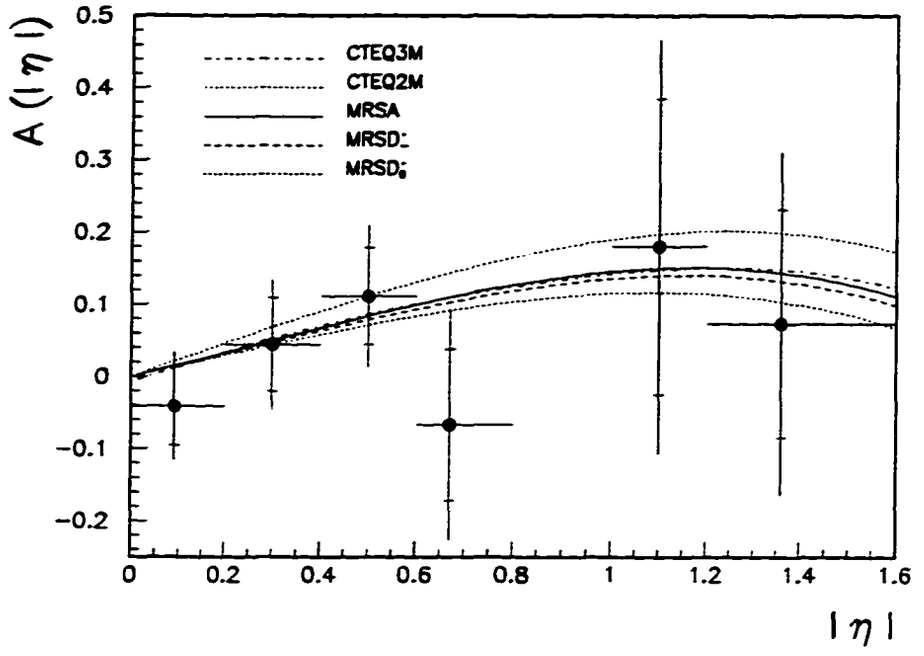

Figure 8.1: The charge asymmetry of muons from W decay for Run 1A.

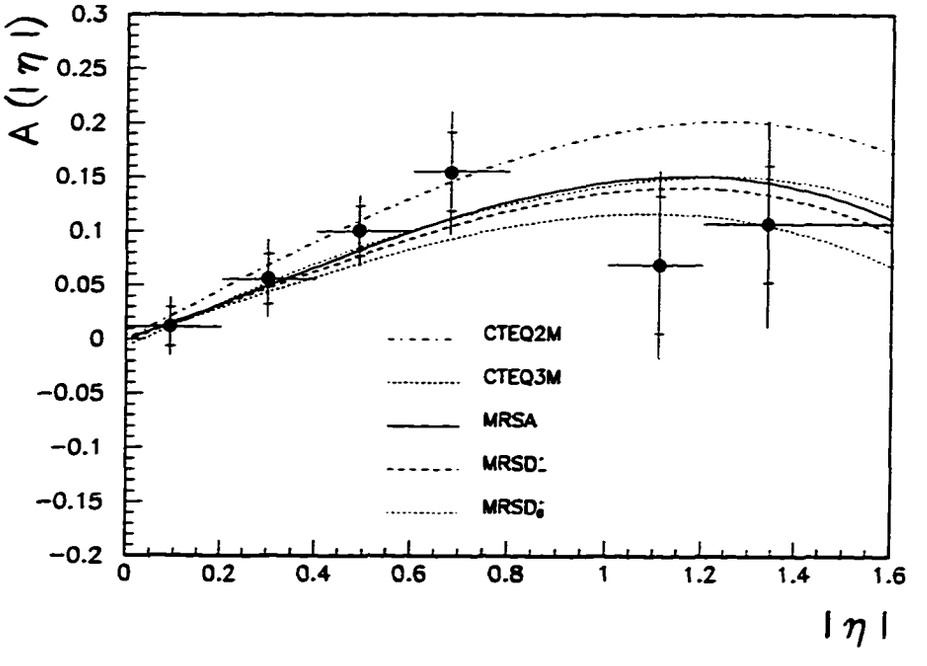

Figure 8.2: The charge asymmetry of muons from W decay for Run 1B.

The final charge asymmetry and errors are plotted in Figures 8.1 and 8.2 for Run 1A and Run 1B, respectively. The long vertical error bars show combined statistical and systematic errors while the short horizontal bars on them indicate the extent of the statistical error. The long horizontal bars indicate the bin widths with the points positioned at the mean value of $|\eta|$ for each bin.

The combined results for Run 1A and Run 1B are shown in Table 8.3 and plotted in Fig. 8.3.

The curves labelled with names of parton distribution functions (PDF's) are theoretical values for the charge asymmetry calculated with the fast Monte Carlo generator, described in Section 2.6, with the corresponding PDF as input. Of these CTEQ2M, MRSD'$_-$ and MRSD'$_0$ are older parameterizations that use data from deep inelastic scattering experiments. MRSA and CTEQ3M are more recent and these also use W charge asymmetry data from measurements made by the CDF collaboration. MRSA is the nominal PDF used in W mass measurements at both the CDF and DØ experiments at the Tevatron.

$< \lvert\eta_\mu\rvert >$	$A(\lvert\eta_\mu\rvert)$
0.09	0.006 ± 0.022
0.30	0.055 ± 0.029
0.49	0.101 ± 0.028
0.68	0.135 ± 0.049
1.11	0.073 ± 0.084
1.34	0.097 ± 0.091

Table 8.3: The combined Run 1A and Run 1B charge asymmetry of muons from W decay.

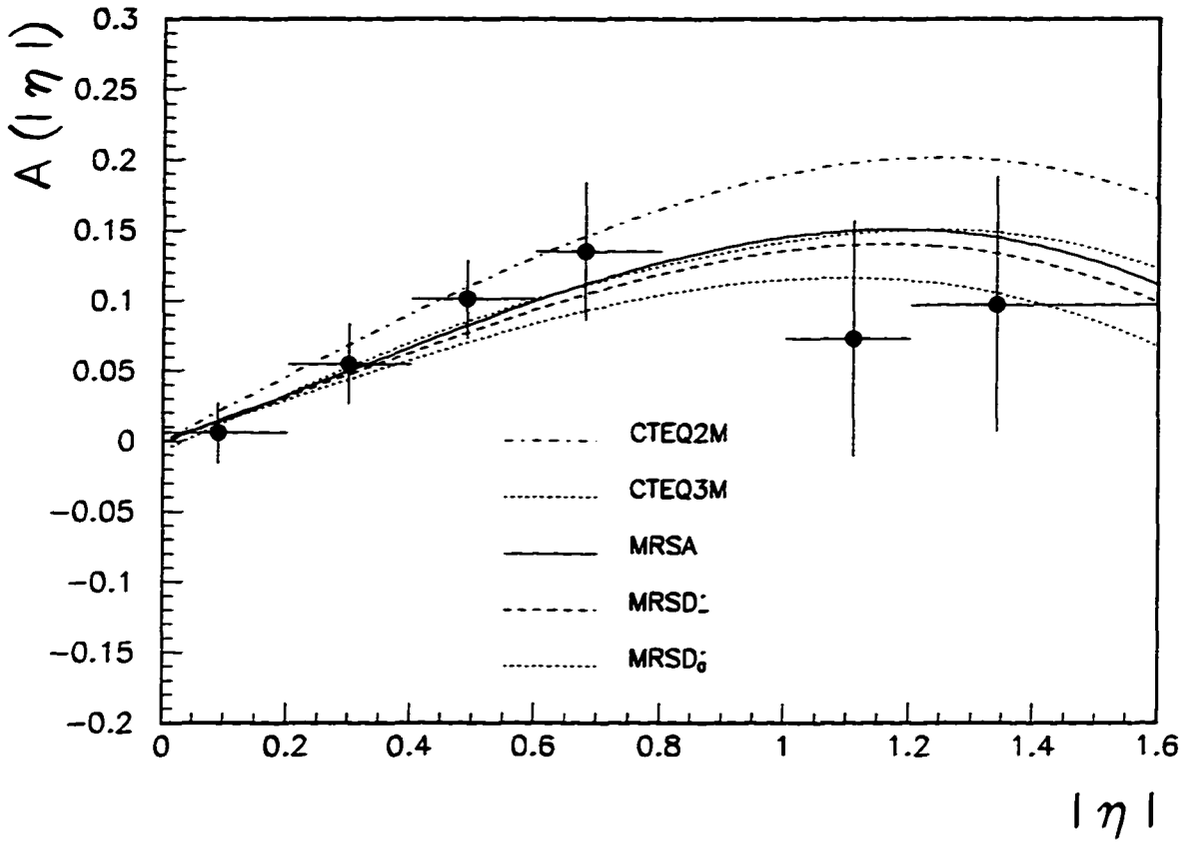

Figure 8.3: The combined charge asymmetry of muons from W decay for run1A and Run 1B.

8.3 Estimating the best fit

We compare data and theory using a reduced χ^2 value defined by

$$\chi^2 = \frac{1}{N} \sum \frac{(A_i - P_i)^2}{\sigma^2_{A_i}}.$$

Here the sum is over N= 6 bins of η, A_i is the measured asymmetry and P_i is the prediction obtained from theory for a particular input parton distribution function (PDF). Comparing the measurements shown in Figure 8.3 with the theoretical curves gives the reduced χ^2 values shown in Table 8.3.

8.4 Conclusion

As can be seen from the reduced χ^2 values in Table 8.3, the data cannot discriminate between the parton distribution functions we have considered but is consistent with all of them. The reason for this lack of discrimination is limited statistics. Figure 8.3 indicates that maximum discrimination may be obtained in the EF, $1.0 \leq |\eta| \leq 1.6$, where the theoretical curves diverge from one another. Radiation damage to proportional drift tubes in this region reduced their efficiency leading to a loss of good track candidates. Additional loss in statistics resulted from prescaling the Level 1 muon trigger to handle the high rates in this region.

PDF	Run 1A & 1B
CTEQ2M	0.716
CTEQ3M	0.294
MRSA	0.331
MRSD'_	0.352
MRSD'$_0$	0.421

Table 8.3: Reduced χ^2 values from a comparison of data with some recent PDF's.

The W charge asymmetry has also been measured by the CDF experiment [54]. The CDF detector can identify the charge on both electrons and muons. With events in both channels, their measurement extended up to roughly $|\eta| \approx 1.8$ in Run 1A and to 2.3 in Run 1B. The Run 1A measurements were used in fits by the MRS and CTEQ groups. The Run 1B measurements in the $|\eta| > 2.0$ region has shown that existing PDF's may be in need of further tuning to fit the data. Figure 8.4 [55] shows the CDF and DØ measurements simultaneously. The effect of limited statistics on the DØ measurement is clear from this plot.

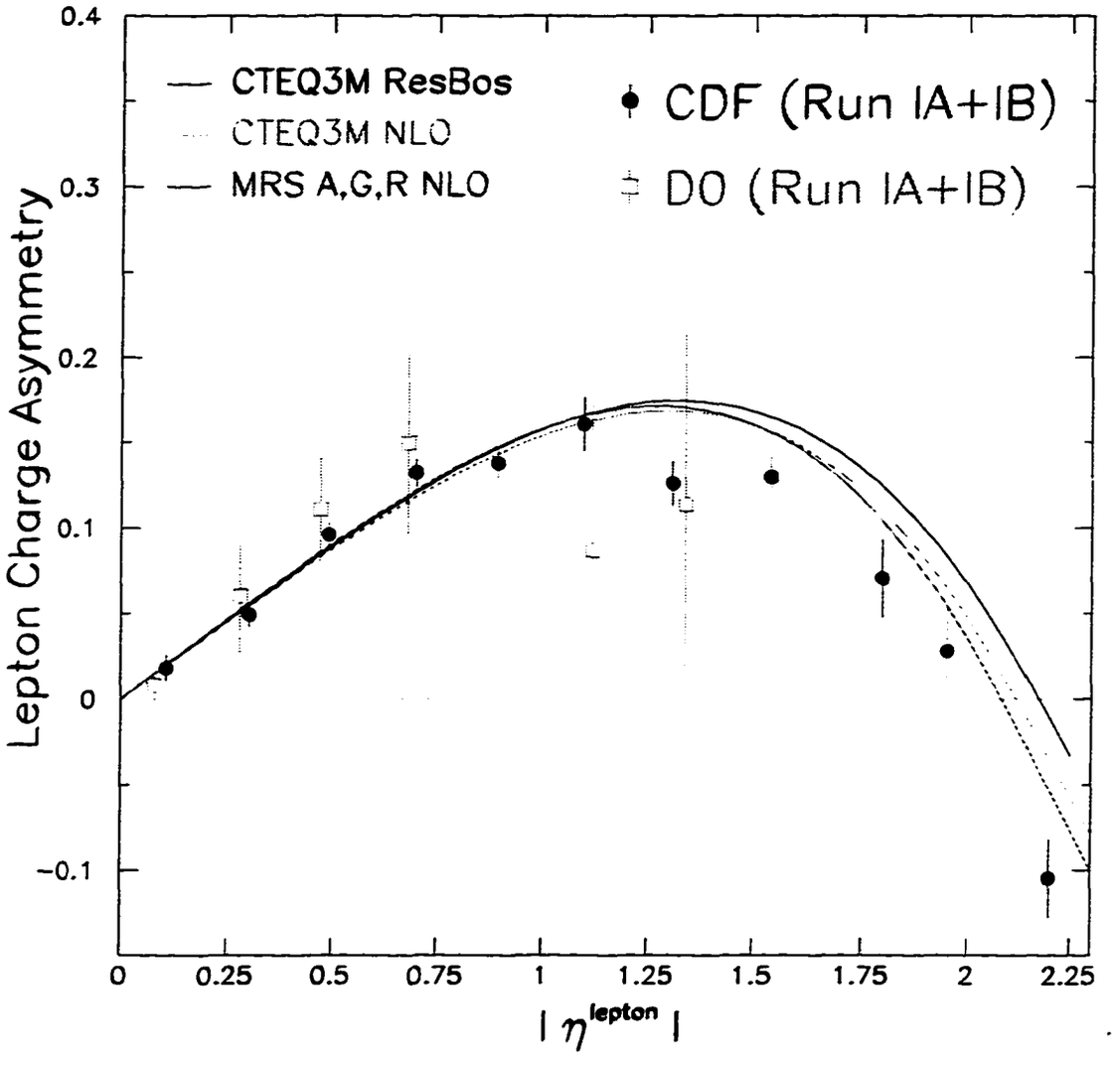

Figure 8.4: The charge asymmetry measurement of leptons from W decay for run1A and Run 1B by the CDF and DØ experiments.

CHAPTER 9

PROSPECTS FOR RUN II

9.1 Introduction

The Fermilab Tevatron is undergoing a major upgrade (the Main Injector) which will increase the delivered luminosity by almost a factor of 10 to 2 $\times 10^{32}$ $cm^{-2}s^{-1}$. At the same time the Tevatron center-of-mass energy will be increased to 2 TeV. A consequence of the accelerator upgrades is that the beam crossing times will decrease from 3.5μs to 396 or perhaps 132 ns. The total integrated luminosity delivered in Run II is expected to be 2 fb^{-1}. The physics potential of the W asymmetry measurement in Run II is discussed in this chapter.

The increased luminosity and decreased beam crossing times require the DØ detector to undergo a major upgrade. Significant additions include a new tracking system consisting of a 2T solenoid, silicon vertex detector (SVX), and central fiber tracker (CFT). As a result, DØ will be able to precisely measure the signed momentum of both muons and electrons in Run II. Central and forward preshower detectors will be added to increase electron identification capability. The forward muon detector system will be replaced with mini-drift tubes and scintillation trigger counters. Additional details may be found in [56]. In this chapter, those elements relevant to the W asymmetry measurement are described in brief.

9.2 Tracking System

As mentioned, D0 will install an entirely new tracking system for Run II. Closest to the beam will be a silicon vertex (SVX) detector. It consists of six 12 cm disk/barrel modules. The barrel has four layers of double sided silicon with $r - \phi$ and stereo views. "F" disks located between the six barrels and "H" disks located in the forward direction,

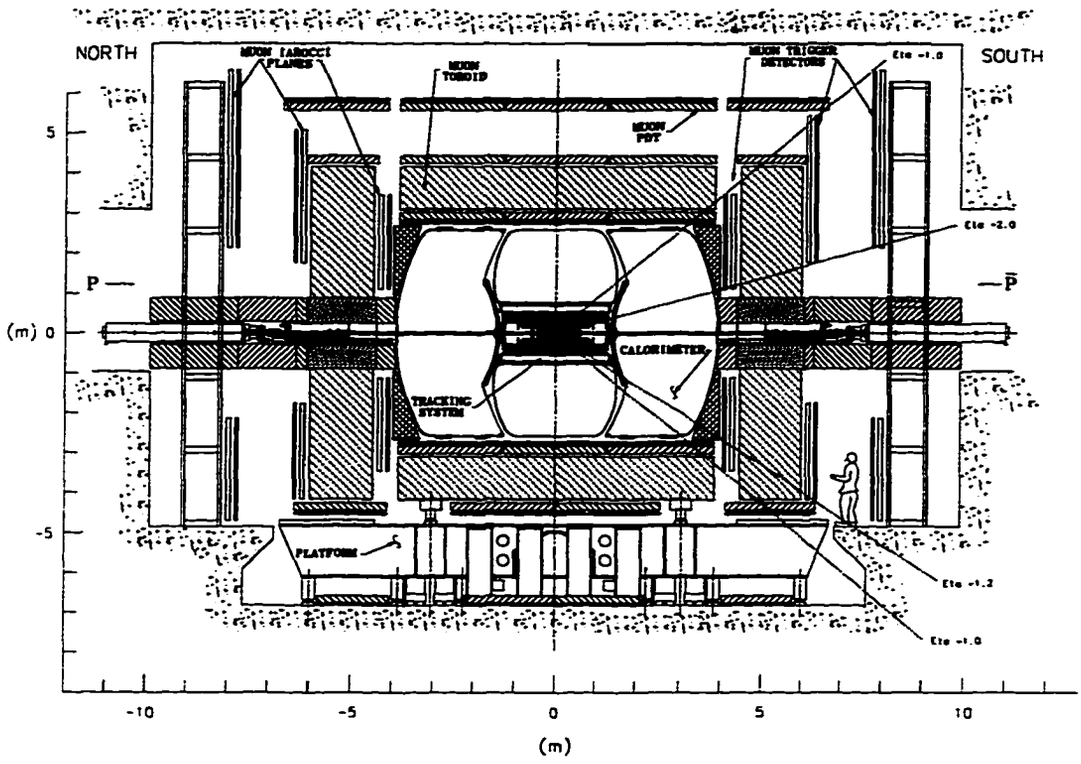

Figure 9.1: Elevation view of the DØ detector for Run II.

beyond the barrels, provide forward track reconstruction out to eta of 2.5. The "F" and "H" disks are also made of double sided silicon with plus and minus 15° and 7.5° stereo views respectively. The SVX impact parameter resolution is 10μm .

The solenoid and the central fibre tracker will be installed inner to the calorimeter. The solenoid is a 2.8 m long superconducting magnet with an average radius of 60 cm. It has two layer coil that provides a uniform 2T field.

The central fibre tracker (CFT) detects charged particle using scintillating fibres of diameter 835 μm . It consists of eight concentric cylinders at radii 19.5, 23.4, 28.1, 32.8, 37.5, 42.1, 48.8 and 51.5 cm. Each cylinder supports a doublet layer of axial fibers. Cylinders at odd numbered radial positions also support two additional doublet layers of fibres that are oriented at $\pm$(2.0°) stereo angles. Each doublet consists of two layers of fibres in a close packed configuration. The stereo layers will enable the measurement of the z-coordinate. The fibres are read out using visible light photon counters (VLPC's).

The eight layer coverage of the CFT extends to $|\eta| < 1.7$.

The momentum resolution that the SVX-CFT tracking system is expected to achieve is $\Delta p_T/p_T^2 \approx 0.002$.

9.3 Electron Detection

As in Run I, electrons are detected by the Uranium-Liquid Argon calorimeter which remains unchanged except for an upgrade of the front-end and readout electronics necessary to accommodate the shorter beam-crossing times. Electron identification will be enhanced by the tracking system which will allow a momentum measurement to be matched to the calorimeter energy.

Electron identification will also be aided by a central ($|\eta| < 1.2$) and two forward ($1.4 < |\eta| < 2.5$) preshower detectors. The preshower detectors function as a "ninth" layer of the fiber tracker and consist of one or two layers of extruded scintillator strips readout by wavelength shifting fiber and 2 X_0 of lead absorber. The preshower detectors help electron identification by early sampling of shower energy and precise position measurement.

9.4 Muon Detection

Muons will be identified by "stubs" or tracks in the muon detector system as in Run I, however a matching track in the CFT/SVX system will provide the precise signed momentum measurement.

In the central region ($|\eta| < 1.2$), the existing PDT's and the C-layer "Cosmic-Cap" scintillation counters will be retained, but the front-end and readout electronics will be upgraded. The drift time in the PDT's will be lowered to 450 ns from 800 ns by using a faster gas mixture of Ar(90%), CF_4(10%) and CH_4(10%). Note that there will still be some pile-up of hits because of the decreased beam crossing times. The trigger hardware will use information from fast scintillating detector elements to sort out hits and correlate them with crossings. New "A-ϕ" scintillating counters will be mounted on the A-layer. At the bottom, where calorimeter supports hamper the placement of these counters on

the A-layer PDT's, the counters are placed on the B-layer PDT's. The ϕ-segmentation of these counters is 4.5° to match the sector segmentation of the CFT. There are nine counters in the z dimension. Timing cuts in the A-ϕ and Cosmic Cap counters is used to reject out-of-time backgrounds.

The forward region ($1.0 < |\eta| < 2.0$) will be entirely new. The PDT's in Run 1 suffered radiation damage due to a combination of high particle fluxes and out-gassing of the Glassteel used to make the cathode pads. In Run II, there will be three layers of mini-drift tubes and three layers of scintillator "pixel" trigger counters. The innermost layer ("A") of both detectors is inside the EF toroids while the other two layers ("B" and "C") are outside the toroids. This configuration is similar to the PDT layout in the central region.

The mini-drift tubes are made of 8 cell aluminum extrusions. Each cell is 1 cm x 1 cm in cross section. Each layer of mini-drift tubes has three ("B" and "C" layers) or four ("A" layers) decks of tubes. The gas used is identical to that used for the central PDT's giving a maximum drift time of 100 ns.

The "pixel" scintillation counters are of size $\Delta\phi = 4.5\,\mathrm{deg}$ and $\Delta\eta = 0.1$. The phi segmentation again matches the sector segmentation of the CFT. Charged or neutral particle backgrounds are greatly reduced by the use of timing cuts in the three layers of counters. In addition, hits in the forward muon detectors arising from beam and target jet interactions with beam-line elements such as the low beta quads are greatly reduced due to the addition of substantial shielding around these elements. A shield of 15" of iron, 6" of polyethylene, and 1" of lead is used to absorb particles produced from these interactions.

9.5 Charge Asymmetry Measurement in Run II

These capabilities of the upgraded DØ detector are well suited to making the charge asymmetry measurement. Two of the physics goals for Run II are the measurement of the lepton charge asymmetry in W boson decay and measurement of the forward/backward asymmetry in Z decays.

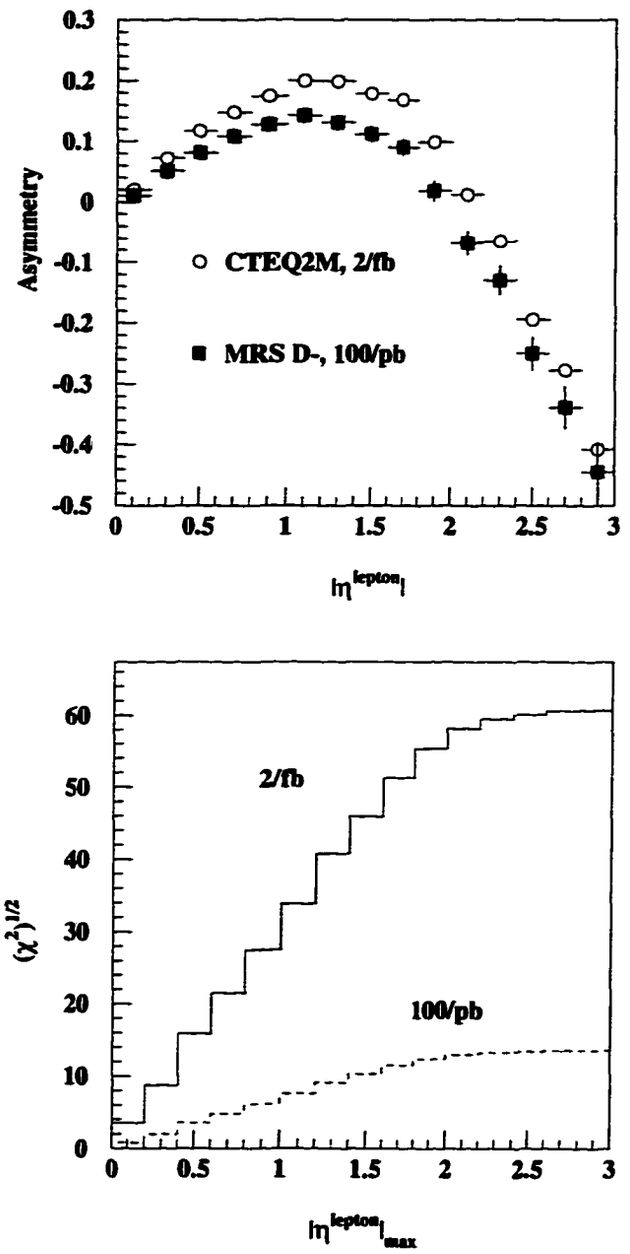

Figure 9.2: Top: W charge asymmetry vs the pseudorapidity of leptons by CTEQ2M and MRSD-. Bottom: The significance with which the charge asymmetry predicted by CTEQ2M and MRSD- can be differentiated for integrated luminosities of 2 fb^{-1} and 100 pb^{-1}.

We could expect to collect $\approx 1.0 \times 10^6$ $W \rightarrow e\nu$ and $W \rightarrow \mu\nu$ events each with the 2 fb^{-1} of data expected in Run II. With such statistics the W charge asymmetry measurement can be used to better distinguish among competing parton distribution functions. For example, the upper plot in Fig. 9.2 [56] [57] shows the W charge asymmetry for two input parton distribution functions MRSD- and CTEQ2M. The error bars are assumed to be simply $1/\sqrt{N}$ (see discussion following (4.3))

The total number of events for CTEQ2M has been normalized to an integrated luminosity of 2 fb^{-1} and that for MRSD- has been normalized to an integrated luminosity of 100 pb^{-1} . The statistical power of 2 fb^{-1} of data is easily seen.

The lower plot in Fig. 9.2 [56] shows two histograms highlighting the significance of the difference between CTEQ2M and MRSD-. For each histogram, the value plotted for each $|\eta_{\text{lepton}}|$ bin is the $\sqrt{\chi^2}$ between the two PDF's integrated from η=0 to that bin. The dashed curve assumes 100 pb^{-1} of data and the solid curve assumes 2 fb^{-1} of data. It can be seen that discrimination between the PDF's is best in the pseudorapidity range between 1.0 and 2.0 where the slope of the histograms is the steepest. Beyond a value of 2.0, the slope becomes shallow and discrimination becomes more difficult.

REFERENCES

[1] R.M. Barnett *et al.* *Phys. Rev.*, D54:1, 1996.

[2] J. L. Rosner. *hep-ph/9704331 15 Apr 1997.* (To be submitted to Comments on Nuclear and Particle Physics), 1997.

[3] Barger V., Phillips R. *Collider Physics*, 1987.

[4] Berger E. L., Halzen F., Kim C. S., Willenbrock S. *Phys. Rev. D*, 40:83, 1989.

[5] Martin A. D., Roberts R. G., Stirling W. J. *Mod. Phys. Lett.*, [4]12:1135, 1989.

[6] New Muon Collaboration, Amaudrez P., *et al.* *Nucl. Phys.*, B 371:3, 1992.

[7] Fermilab E665 Collaboration, Adams M. R. *et al.* *Phys. Rev. Lett.*, X:Y, 1995.

[8] New Muon Collaboration,. *CERN-PPE/95-138, Submitted to Phys. Lett.*, X:Y, 1995.

[9] New Muon Collaboration,Amaudrez P., *et al.* *Phys. lett.*, B 295:159, 1992.

[10] BCDMS Collaboration, Benvenuti *et al.* *Phys. Lett.*, B 237:592, 1990.

[11] H1 Collaboration, Ahmed T., *et al.* *Nucl. Phys.*, B 439:471, 1995.

[12] Zeus Collaboration. *Phys. Lett.*, B 316:412, 1990.

[13] New Muon Collaboration, M. Arneodo *et al.* *Phys. Rev.*, D 50:1, 1994.

[14] Martin A. D., Roberts R. G., Stirling W. J. *Phys. Lett.*, 252:653, 1990.

[15] Gottfried K. *Phys. Rev. Lett.*, 18:1174, 1967.

[16] Streets K Demarteau M., Sculli J. *DØ Internal Note: 2929*, 1996.

[17] Plothow-Besch H. *Comp. Phys. Comm.*, 75, 1993.

[18] Yuan C.P. Ladinsky G.A. *Phys. Rev.* **D**, 50:4239, 1994.

[19] Kauffman R.P. Arnold P.B. *Nucl. Phys.* **B**, 349:381, 1991.

[20] Ting Hu. *Ph.D. Thesis* State University of New York at Stony Brook, 1996.

[21] Matsura T. Hamberg R., van Neerven W. L. *Nucl. Phys.* **B**, 359:343, 1991.

[22] Takeuchi T. Rosner J. L., Worah M. P. *Phys. Rev.* **D**, 49:1363, 1994.

[23] Flattum E. *Ph.D. Thesis* Michigan State University, 1996.

[24] Thomson J. *DØ Internal Note: 2367, FERMILAB-TM-1909*, 1995.

[25] DØ Collaboration, S. Abachi *et al.* *Phys. Rev. Lett.*, 74:2632, 1995.

[26] F. Abe *et al.* CDF Collaboration. *Phys. Rev. Lett.*, 74:2626, 1995.

[27] DØ Collaboration, S. Abachi *et al.* *Nucl. Instr. Meth.* **A**, 338:185, 1994.

[28] Clark A. R., *et al.* *Nucl. Instr. Meth.* **A**, 315:193, 1992.

[29] Frank I. M. Ginzberg V. L. *JETP*, 16:15, 1946.

[30] Jackson. *Classical Electrodynamics, 2 ed.*, 1975.

[31] G. Yodh X. Arthu and G. Mennessier. *Phys. Rev.* **D**, 12:1289, 1975.

[32] Clark A. R., *et al.* *Nucl. Instr. Meth.* **A**, 279:243, 1987.

[33] Avery R., *et al.* *IEEE. Trans. Nucl. Sci* **NS**, 40:573, 1993.

[34] Amos N. *et al.* *DØ Internal Note: 2031*, 1994.

[35] Bantly J. *et al.* *DØ Internal Note: 2544*, 1995.

[36] Hedin D. *DØ Internal Note: 1738*, 1993.

[37] Green D., *et al.* *Nucl. Instr. Meth.* **A**, 224:356, 1986.

[38] Haggerty H. Marshall T. *DØ Internal Note: 2556*, 1995.

[39] DØ Collaboration. To be submitted to *Nucl. Instr. Meth.* **A**, 1997.

[40] F. Abe *et al.* CDF Collaboration. *Phys. Rev.* **D**, 50:5550, 1994.

[41] F. Abe *et al.* CDF Collaboration. *Phys. Rev.* **D**, 50:5518, 1994.

[42] F. Abe *et al.* CDF Collaboration. *Phys. Rev.* **D**, 50:5535, 199.

[43] Amos N. *et al.* Fermilab E710 Collaboration. *Phys. Lett.* **B**, 243:158, 1990.

[44] Snyder S. *D0$CONFIGS$ROOTis:[COOR_SIM]TRIGPARSE.DOC]*, 1994.

[45] Gerber C. *Ph.D. Thesis* Universidad de Buenos Aires, 1994.

[46] Hedin D. *D0$MUON_UTIL$ROOT:[DOCS]MUON_ANALYSIS.MEM*, 1992.

[47] Ting Hu. *DØ Internal Note: 1811*, 1993.

[48] Gallas E. *DØ Internal Note: 2066*, 1994.

[49] John Butler. *DØ Internal Note: 2602*, 1995.

[50] DØ Collaboration, S. Abachi *et al.* *Phys. Rev. Lett.*, 76:2228, 1995.

[51] Quintas P. Private communication.

[52] Wood D. *http://www-d0.fnal.gov/darien/tfloat_studies.html*, 1996.

[53] *D0$MUON_RECO$ROOT:[SOURCE]MU_SMEAR.FOR.*

[54] CDF II Collaboration. *The CDF Detector, Techical Design Report, FERMILAB-Pub-96/390-E*, page 35, 1996.

[55] Young-Kee Kim. *Private Communication. Presented at ls Snomass*, 1997.

[56] DØ Collaboration. *http://higgs.physics.lsa.umich.edu/dzero/d0doc96/d0doc.html*, 1996.

[57] Wood D. Private communication.